Bars in Edge-On Spiral Galaxies

by

Martin Bureau

A thesis submitted for the degree of

Doctor of Philosophy

of The Australian National University

Mount Stromlo and Siding Spring Observatories
Institute of Advanced Studies
The Australian National University

August 1998

To my mother, who nurtured my curiosity toward nature.

Declaration of Authorship

I hereby declare that the work presented in this thesis is that of the candidate alone, except where indicated in the text and as described below.

The following chapters are modified versions of papers submitted or shortly to be submitted for publication.

Chapter 2 *The Shape and Figure Rotation of NGC 2915's Dark Halo*, by Bureau, M., Freeman, K. C., Pfitzner, D. W., & Meurer, G. R. (submitted to The Astronomical Journal)

Chapter 3 *Bar Diagnostics in Edge-On Spiral Galaxies. I. The Periodic Orbits Approach*, by Bureau, M., & Athanassoula, E.

Chapter 4 *Bar Diagnostics in Edge-On Spiral Galaxies. II. Hydrodynamical Simulations*, by Athanassoula, E., & Bureau, M.

Chapter 5 *The Nature of Boxy/Peanut-Shaped Bulges in Spiral Galaxies*, by Bureau, M., & Freeman, K. C. (to be submitted to The Astronomical Journal)

The candidate wrote the above papers and co-authors contributed to refining the text.

In Chapter 2, D. W. Pfitzner contributed preliminary results from a set of CDM simulations. E. Athanassoula provided a number of routines used in Chapters 3 and 4.

Martin Bureau

August 1998

Acknowledgements

The research presented in this thesis would not have been possible without the cooperation, advice, and support of many people, to whom I am indebted.

First, I am indebted to Ken Freeman, for accepting to supervise me in the path I chose, for providing valuable advice and insightful comments throughout my thesis, and for sharing his knowledge and providing much appreciated guidance. Thank you for treating me as an equal, for teaching me to identify the important questions and to be open to new ways of answering them, and thank you mostly for sharing with me the excitement of research. I hope this is only the beginning of a long association. I also wish to thank Agris Kalnajs, for many lengthy discussions and for his tremendous knowledge and critical views of various works. I am grateful to Lia Athanassoula and Albert Bosma, for welcoming me in their group at the Observatoire de Marseille, and wish to thank Lia for a fruitful collaboration and for giving me access to her hydrodynamical models. Merci aussi à Jean-Charles et Eric pour le support informatique. Similarly, I am grateful to Gerhardt Meurer for access to the NGC 2915 data.

I am also indebted to Jeremy Mould and Lister Staveley-Smith, for getting me involved in various side projects during my thesis. Je ne saurais comment remercier Claude Carignan, à l'Université de Montréal, pour avoir initié mon intérêt pour la dynamique des galaxies, et pour avoir, par la suite, suggeré et supporté ma venue à Mount Stromlo.

Thanks also to Tim de Zeeuw, Ortwin Gerhard, Daniel Pfenniger, and their respective institutes, for allowing me to visit, to exchange ideas, and mostly for advice at a crucial stage of my thesis. A big thank you also to Linda Sparke, for getting me started on the periodic orbits project. I extend similar thanks to the many people who provided comments on my work in a hallway, sipping a cup of coffee, or over a meal, during conferences. These include Ron Buta, Françoise Combes, Jerry Sellwood, and many others.

Finally, I want to express my sincere gratitude to the staff of Siding Spring Observatory, the Australia Telescope National Facility, and the workshops here at Mount Stromlo, for providing and maintaining top quality instruments. I am equally grateful to the administrative, computing, and other support staff at Mount Stromlo Observatory, without whom none of this work would have been possible. A thousand thanks as well to the academic staff, who were always available when needed.

Of course, a great deal of personal and social support is also required to undertake such large task as a thesis, and I am indebted to many people, friends and family.

Tout d'abord, j'aimerais remercier ma mère, à qui cette thèse est dédiée. Son support et ses encouragements, depuis le début des mes études, sont à l'origine de mes succès. Merci aussi pour m'avoir donné le pouls de Montréal pendant mon absence. Merci également à mon père, pour son amour de la nature, qui m'a inspirée. I must of course thank the other students of Mount Stromlo, who have made my stay a memorable experience. A special thank to past and present residents of House #16: Sylvie, pour l'aide à mon arrivée; Sungeun, for being herself; Ben, for providing a reliable drinking partner; Lisa and Kim, the first Aussies I lived with; Heath, for his formidable Tercel; and finally Octave, for showing me how wonderful life would be if I only had to eat and sleep. I am also indebted to many other past and current residents of the mountain: Uncle Simon, for feeding us all and for a house full or treasures; Mark, for his friendship and good port; and Dave, for an introduction to pit cooking. Thanks of course to all the other students whose friendship I value: Ian, Mary, Oak-Kyoung, Ron, etc. Of course, thanks to all of you, for keeping up with my Frenchism(s)!

I would also like to express my gratitude to the staff and students of the Vatican Observatory Summer School of 1995, for memories which will last a lifetime. Similar thanks also to the various Australian and overseas astronomy students I have met over the years, for wonderful memories.

J'aimerais aussi remercier et reitérer mon amitié à toute la gang de Brossard: Tounic, Lépine, Homsy, Alex, Petit, Tommy, ... Merci surtout pour votre amitié, mais aussi pour avoir enduré mon côté studieux et mes absences fréquentes, et pour avoir gardé contact pendant quatre longues années. Merci d'être vous-mêmes, je ne vous échangerais contre rien au monde. Merci aussi à Jean-François et Quan, pour une amitié profonde et durable.

Of course, special thanks to Makiko, for embarking on a common journey despite the distance separating us. You have enriched my life in more ways than you can imagine.

Finally, a special thank to all the Aussies I have met, for showing me what Australia is all about.

I would also like to acknowledge the financial support of a Canadian NSERC Postgraduate Scholarship, an Australian DEETYA Overseas Postgraduate Research Scholarship, the Astronomical Society of Australia, and of the various institutes I visited and conferences I attended.

Abstract

The main goal of this thesis is to deepen our understanding of the structure and dynamics of bars in spiral galaxies. We first tackle the issue of the pattern speed of bars. We measure directly the bar pattern speed in the galaxy NGC 2915, the first time this is achieved in a late-type gas-rich system. NGC 2915 is a unique object, possessing a blue compact dwarf galaxy core and a H I disk with a bar and spiral arms pattern extending far beyond the optical galaxy. The bar pattern speed is slow, putting corotation at more than 1.7 bar radii, a value incompatible with self-consistent models of barred disks. We demonstrate that the spiral pattern cannot be due to interactions, be sustained by swing amplification, or be driven by the bar. Because the disk of NGC 2915 is dominated by dark matter, we argue that an extensive triaxial dark halo with a slow figure rotation could drive the disk morphology. The existence of such halos is supported by a preliminary analysis of a set of CDM simulations. If our interpretation is right, objects like NGC 2915 offer new opportunities to probe the structure and dynamics of dark halos.

The main part of this thesis is concerned with the vertical structure of bars, and with observational tests of the bar-buckling mechanism for the formation of boxy/peanut-shaped (B/PS) bulges in (edge-on) spiral galaxies. Because bars in edge-on spirals are hard to identify morphologically, we first had to develop bar diagnostics. We use the kinematical signature that a bar imposes on the position-velocity diagram (PVD) of an edge-on disk. We first use periodic orbit families as building blocks to model the structure of real galaxies. We show that the global structure of the PVDs is a reliable bar diagnostic in edge-on disks. Gaps between the signatures of the various periodic orbit families arise in the PVDs due to the non-homogeneous distribution of orbits in a barred disk. We show specifically how the signatures of the x_1 and x_2 families of periodic orbits can be used to determine the viewing angle with respect to the bar.

We also develop bar diagnostics for edge-on disks using hydrodynamical simulations, which specifically target the gaseous component of spiral galaxies. We show that, when a nuclear spiral is formed, associated with the existence of x_2 orbits, the presence of a gap in the PVDs, between the signature of the nuclear spiral and that of the outer parts of the disk, reliably indicates the presence of a bar. This gap is caused by shocks and inflows which lead to depletion of the gas in the outer bar region. The shape of the signature of the nuclear spiral also allows us to determine the viewing angle to the bar.

The last part of this thesis constitutes an extensive observational study of the relationship between bars and B/PS bulges. Using emission line spectroscopy, we search for bars in a large sample of edge-on spiral galaxies with B/PS bulges, and in a smaller control sample of spirals with more spheroidal bulges. We show that almost all B/PS bulges are due to a thick bar viewed edge-on, while only a few extreme cases may be due to the accretion of external material. This strongly supports the bar-buckling mechanism for the formation of B/PS bulges, and implies that accretion plays at most a minor role in the formation of these objects. None of the galaxies in the control sample shows evidence for a bar, which suggests conversely that all bars are B/PS. Studies of this type open up for the first time the possibility of studying observationally the vertical structure of bars. We introduce a number of related ongoing projects before concluding this thesis.

Contents

List of Figures

List of Tables

Chapter 1

Introduction

From ellipticals to dwarfs, galaxies display an amazing variety of morphologies. This is particularly the case for spiral galaxies, where the importance of the bulge, spirals arms, and star formation, all at the core of the Hubble classification of galaxies (Sandage 1961), vary enormously. Although it is less recognised, the bulges of spiral galaxies also show a wide variety of shapes. Boxy and peanut-shaped bulges perhaps form the best known category departing from the classical picture of a spheroidal bulge.

Boxy/peanut-shaped (B/PS) bulges can be distinguished only in edge-on spiral galaxies and are characterised by isophotes which are flat with radius or slightly depressed along the minor axis. This suggests that their vertical structure is significantly different from that of the more spheroidal bulges (Binney & Petrou 1985). In addition, it is now known that spiral galaxies with a B/PS bulge are common, constituting about 20-30% of the spiral galaxy population (see, e.g., Shaw 1987). With the recent discovery that the bulge of the Milky Way is also boxy-shaped (Weiland et al. 1994), it becomes even more important to gain a good understanding of these objects. The core of this thesis is concerned with the development and use of tools to study the three-dimensional structure and dynamics of B/PS bulges, in an attempt to identify their formation mechanism.

As is often the case in astronomy, one can identify phases in the study of B/PS bulges when research focussed on a specific topic and a paradigm was developed. New observational data can topple those paradigms and nurture the rapid progress of new ideas. We may be in such a period now with regard to our understanding of the formation and nature of B/PS bulges.

A chronological approach is well-suited to a review of our knowledge of these fascinating objects. In the next section, the works which laid the foundation for the present study of B/PS bulges will be explored. We will mostly concentrate on the theoretical ideas which were put put forward to explain the formation of B/PS bulges, but will point out, when necessary, observations which either supported, opposed, or prompted these theories. This way, we hope to stress the interplay between theory and observations which guided the evolution of this subject since its beginning.

1.1 The Nature of Boxy/Peanut-Shaped Bulges in Spiral Galaxies: A Historical Perspective

1.1.1 The Recognition of the Boxy/Peanut-Shaped Bulge Phenomenon

It is hard to pinpoint the time when it was first recognised that some spiral galaxies had a bulge with a significant boxy/peanut shape. Burbidge & Burbidge (1959) discussed the unusual shapes of the bulges in NGC 128 (one of the best example of a peanut-shaped bulge), saying that "...NGC 128 is unusual, as its maximum extent perpendicular to the major axis occurs not at the center but at two points symmetrically spaced on either side of the center.", and in NGC 7332, stating that "The shape of the nuclear region is almost rectangular; this galaxy looks intermediate between a normal S0 and NGC 128.". Although they did not use the term B/PS bulge, they had already identified the main property of this class of object. Hodge & Merchant (1966) also noted the "...squareness of the central regions" in their photometric study of NGC 128.

The term "boxy-shaped bulge" maybe due to Sandage (1961) when, in *The Hubble Atlas of Galaxies*, he commented: "NGC 128 has a peculiar box-shaped nucleus." and "NGC 7332 is classed as peculiar because of the box-shaped central regions, ...". On the other hand, many other galaxies in *The Hubble Atlas of Galaxies* have a B/PS bulge but were not labelled as such. For example, about NGC 4565, Sandage said "Note how flat the central cross section of NGC 4565 is.", while no comment on the boxy-shaped bulge of NGC 891, or the peanut-shaped bulge of NGC 4111, was made.

Historically, it is clear that the property of some bulges to appear boxy or peanut-shaped when viewed edge-on was recognised early-on. However, it seems that, at this point, this behaviour was viewed as a peculiarity of no special significance.

1.1.2 The Differentiation of Bulges and Ellipticals

In the early 1970s, a lot of work was devoted to the understanding of the structural and dynamical properties of elliptical galaxies. Prompted mostly by the flattened light distribution of ellipticals, oblate spheroidal models with isotropic velocity dispersions were first constructed (e.g. Lynden-Bell 1962; Prendergast & Tomer 1970). However, it was soon realised (Wilson 1975) that these could not explain the most flattened systems (E5 and later), as they would be unstable to non-axisymmetric perturbations (Ostriker & Peebles 1973). The subject was transformed by kinematical observations which showed that ellipticals rotate too slowly to be rotationally flattened (e.g. Bertola & Capaccioli 1975; Illingworth 1977), and that some have non-zero radial velocity gradients on the minor axis (Bertola & Galletta 1978; Schechter & Gunn 1979). This indicated that ellipticals were oblate spheroids or triaxial ellipsoids with anisotropic velocity dispersions (Binney 1980). While the bulges of spiral galaxies had long been considered close parents of ellipticals, because mostly of the similarities in the light distribution (e.g. Sandage, Freeman, & Stokes 1970), stellar content (e.g. Faber 1977), and kinematics (e.g. Faber & Jackson 1976), these results ultimately changed this view and prompted more detailed studies of bulges.

It was first noted that the light profile of many spiral galaxy bulges did not follow exactly the $R^{1/4}$ law of ellipticals (see, e.g., Kormendy and Bruzual 1978 and Jensen & Thuan 1982 for NGC 4565; Tsikoudi 1980 for NGC 4111). These studies also highlighted the fact that no elliptical galaxy was known (at the time) to possess a B/PS morphology. Furthermore, it was realised that bulges were flatter in the mean than elliptical galaxies (e.g. de Vaucouleurs 1974; Kormendy & Illingworth 1982; see also Kormendy 1980). The result which definitely separated bulges from ellipticals was the realisation that they rotated much more rapidly than the bright ellipticals (see, e.g., Illingworth 1977; Kormendy & Illingworth 1982; Kormendy 1982). Unlike ellipticals, bulges thus appeared to be true rotationally flattened oblate spheroids (see Binney 1976, 1978). Davies et al. (1983) later showed, however, that ellipticals with luminosities comparable to those of bulges had comparable rotation. All these results set the stage for the first comprehensive efforts to model in detail the structure and kinematics of spiral galaxy bulges.

Of particular interest here was the discovery that some of the best known B/PS bulges exhibited cylindrical rotation; i.e. their rotation was independent of the height above the galactic plane (see Kormendy & Illingworth 1982 for NGC 4565; Jarvis 1981 for NGC 128). At this stage, it seemed clear that both the structure and kinematics of B/PS bulges were different from those of “normal” more spheroidal galaxy bulges. In the early 1980s, with the first serious theoretical attempts to understand the formation of B/PS bulges, and then later on with the first systematic studies of the prevalence of these objects, the interest of the B/PS bulge “phenomenon” was finally recognised.

1.1.3 Accretion Scenarios

Jarvis & Freeman (1985a) constructed rotationally flattened axisymmetric models of bulges, using a distribution function based on two integrals of motion, the energy E and angular momentum along the symmetry axis L_z, and an energy cutoff like that of the King (1966) models. Their models reproduced very well the structure and kinematics of spheroidal bulges (Jarvis & Freeman 1985b), but could not account for the cylindrical rotation observed in the B/PS bulges. Jarvis (1981) argued that cylindrical rotators probably require a higher density of material at high L_z in the (E,L_z) plane (close to the boundary defining the circular orbits) than is present in his models, particularly for stars far from the nucleus.

Specifically trying to model B/PS bulges, Rowley (1988) built axisymmetric models based on a two-integral distribution function favouring material on prograde orbits. Contrary to most models at the time, he adopted a truncation depending on both E and L_z, and following a contour of constant density in the (E,L_z) plane. This ensured that his models were cylindrically rotating. Rowley (1986) successfully modelled both kinematical and photometric data for a number of B/PS bulges (although he noted that some bulges were probably mildly triaxial). He argued that the accretion of satellite galaxies by a host spiral was the most likely scenario which could give rise to the distribution function adopted. However, the merger of two similar sized disks could also lead to B/PS bulges in Rowley's (1988) picture; he suggested that this could lead to the larger B/PS bulges.

The work of Binney & Petrou (1985) had an important influence on the way B/PS bulges were thought to form. They constructed a distribution function depending on a third integral of motion, in addition to E and L_z. This third integral generated a higher density of material near a particular plane in action space, which in turn favoured orbits reaching a given height above the galactic plane. These orbits formed tori which appeared B/PS when seen in projection, and cylindrical rotation followed naturally. The models of Binney & Petrou (1985) were not self-consistent, but they provided insight into the structure of (axisymmetric) B/PS bulges. Binney & Petrou (1985) argued that the accretion of satellite galaxies was the ideal way of populating particular regions of action space and thereby forming B/PS bulges. For the accreted material to form a B/PS bulge, the velocity dispersion of the satellite must be much be lower than its orbital speed, and the decay timescale of the orbit must be much longer than the orbital time. This ensures that the accreted material stays clumped in action space.

Following the picture of Binney & Petrou (1985), a range of accretion scenarios could be imagined. However, in order to form a B/PS bulge this way, the range of orbital energies and angular momenta allowed for the accreted material is restricted. It is thus unlikely that several small accreted satellite galaxies would all satisfy this criterion. Remaining satellites should be detectable but they were not observed. Shaw (1987) found that spiral galaxies with a B/PS bulge had no more satellites than spirals with a more spheroidal bulge. The accretion of a single large companion was also excluded, because of the large velocity dispersion and small decay timescale involved, which preclude the clustering of material in action-space. The merger of two spiral galaxies of similar size is another possibility raised by Binney & Petrou (1985). However, Jarvis (1986), Shaw (1987), and de Souza & dos Anjos (1987) showed that B/PS were present in about 20-30% of the entire spiral galaxy population. Because the formation of a B/PS bulge through the merger of two spiral galaxies would require a fairly precise alignment of the spin and orbital angular momenta of the two galaxies, the abundance of these objects makes it an unlikely process (although Rowley 1986 relaxed this condition).

Soon after the work of Binney & Petrou (1985), the accretion of a small number of moderate-sized satellites was left as the only viable accretion scenario to form B/PS bulges. While Shaw (1987) showed that spiral galaxies with a B/PS bulge were not found preferentially in clusters, a cursory examination suggests that the best examples of B/PS bulges are indeed found in small groups (e.g. NGC 128 and ESO 597- G 036). This view was supported by Whitmore & Bell (1988) in another influential paper. They argued that X-shaped structures in spiral galaxies are related to polar-rings, and that both are formed through the accretion of satellite galaxies or external material. While the material in polar-rings is accreted at a nearly perpendicular angle to the disk, they suggested that X-shaped structures could be formed by accreting material at a more oblique angle. Precession is then important, and differential precession spreads the accreted material into a cone, which appears X-shaped in projection. The superposition of the X-shaped structure onto an existing spheroidal bulge will appear B/PS. Their suggestion was supported by the N-body simulations of Hernquist & Quinn (1989), which showed that the accretion of companions on inclined orbits can produce long-lived axisymmetric X-shaped structures.

May, van Albada, & Norman (1985) proposed another mechanism to form B/PS bulges. They showed that a short-lived cylindrical torque, applied to an initially non-rotating prolate triaxial ellipsoid (supported by anisotropic velocity dispersion), leads to an almost axisymmetric rotationally flattened figure with a small figure rotation. Their models appeared clearly B/PS in projection, and the rotation was cylindrical. Although it is not clear how relevant this process might be to the creation of real bulges (the torque is "...merely a convenient experimental device, ..."), similar torques may arise in the early formation stages of galaxies, for example from transient non-axisymmetries in the disks, or from tidal torques during the aggregation process.

While many theoretical ideas involving accretion were put forward during the 1980s, they did not offer clear cut tests of their validity. At that time, observational data were sparse and did not offer a coherent picture of the nature of B/PS bulges. As a consequence, accretion scenarios were generally thought to be an acceptable picture for the formation of these objects.

1.1.4 Bar-Buckling Scenarios

Accretion scenarios were seriously challenged for the first time at the beginning of the 1990s, when it was rediscovered that the three-dimensional (3D) structure of bars tends to evolve toward a boxy/peanut shape when viewed edge-on (Combes et al. 1990; Raha et al. 1991). This idea had been originally proposed by Combes & Sanders (1981) but was neglected. Before we dig deeper into this topic, it is worth retracing the major steps in our understanding of the *two*-dimensional (2D) structure and dynamics of bars. A complete review of barred disks dynamics would take us too far from the issue of B/PS bulges, however, and we refer to the review of Sellwood & Wilkinson (1993) for a more detailed discussion.

The first N-body simulations of rotationally supported stellar disks revealed that they were violently unstable to the formation of large scale bars (e.g. Hockney & Hohl 1969; Miller, Prendergast, & Quirk 1970). These results were confirmed many times over the years, with simulations of ever increasing quality (e.g. Sellwood 1981; Athanassoula & Sellwood 1986). These bi-symmetric instabilities were quickly identified with the dominant linear modes found in stability analyses of axisymmetric disks (Shu 1970; Kalnajs 1971, 1977). The bar instability could be controlled by raising the velocity dispersion in the disk or immersing the galaxy in a massive halo (Ostriker & Peebles 1973). However, this would respectively prevent the propagation of density waves, and imply that galaxies are dark matter dominated even within their optical radii, which is generally not required dynamically (e.g. van Albada & Sancisi 1986). The bars formed in these N-body simulations were fast, ending at or just inside their corotation radius (e.g. Sellwood 1981), although they did slow down slowly with time. They also seemed to match fairly well the observed light distribution of bars (Sparke & Sellwood 1987).

The internal dynamics of barred disks was, and still is, generally explored by studying the orbital structure of model potentials. These are typically composed of a non-axisymmetric component, representing the bar, and some axisymmetric components, representing the disk and halo. The range of mass distributions allowed for bars is constrained by observations, but the bar pattern speed Ω_p is very much a free parameter. Because of the bar potential, the main families of periodic orbits are elongated, and their orientation changes at each major resonance (e.g. Sanders & Huntley 1976). The x_2 family of periodic orbits, elongated perpendicular to the bar, is located inside the inner Lindblad resonances (ILRs); the main family of periodic orbits, the x_1, is elongated parallel to the bar, and is located within corotation (mainly inside the inner ultra-harmonic resonance, IUHR). There are higher order resonance families close to corotation, and periodic orbits around the Lagrange points on the minor axis of the bar, but most are generally thought to be unimportant for the structure of real bars. All these orbit families are mirrored beyond corotation. As the barred component of the potential is made stronger, regions of stochasticity grow around each of the resonances (e.g. Contopoulos & Papayannopoulos 1980). Contopoulos & Grosbøl (1989) provide a more detailed overview of the orbital structure of barred disks. Because self-consistent bars must be supported by the x_1 periodic orbits (and their quasi-periodic analogs), it was realised early-on that bars should end at or just inside corotation (Contopoulos 1980), in agreement with the N-body simulations discussed above. However, nothing formally prevents the bars from having a lower pattern speed.

Most studies mentioned so far considered 2D disks. Because spiral disks are thin, it was thought (despite some evidence for the contrary) that the third dimension was unimportant. James & Sellwood (1978) and Hohl & Zang (1979) carried out some of the first 3D N-body simulations of rotationally supported disks, and noticed that significant vertical structure arose in their models. Combes & Sanders (1981) were the first to notice that the bars in 3D simulations took a B/PS appearance when viewed edge-on. They showed that the thickness of N-body disks increases with time, although this effect could be curbed by a large halo to disk mass ratio. In their models, the bars appeared boxy-shaped when seen end-on and peanut-shaped when seen side-on, and they proposed that this effect could be at the origin of the B/PS bulges seen in many spiral galaxies. Unfortunately, the bar buckling/thickening hypothesis for the formation of B/PS bulges was only half-born at this stage, as their idea was not investigated further for almost 10 years.

The idea resurfaced only after the work of Combes et al. (1990) and Raha et al. (1991). This explains why, despite continuous work on the structure and dynamics of barred spiral galaxies, the idea of forming B/PS bulges through bar-buckling has only taken off in recent years. Using N-body simulations, Combes et al. (1990) showed that bars form and take on a B/PS appearance when viewed edge-on under a large variety of conditions (different numerical schemes, initial mass distributions, initial conditions, etc.). All the bars thickened soon after forming, ending close to corotation once an equilibrium state was reached. This work established that bar formation and thickening is a generic property of rotationally supported stellar disks. Combes et al. (1990) also generated two-dimensional velocity and velocity dispersion fields, and showed that cylindrical rotation is confined to the brightest parts of the bar/bulge. Raha et al. (1991) reported on similar simulations. However, they showed that in an initially thin disk, the buckling of a bar out of the plane of the galaxy can be so violent as to seriously disrupt and weaken it. Bars form, buckle, and then settle with an increased thickness and velocity dispersion. They suggested that such violent buckling may be able to totally destroy a bar, and could explain the relatively low fraction of barred spiral galaxies observed (i.e. why many galaxies are not barred). They also provided snapshots of the disks in the act of bending, with strong saddle shapes. These strongly support the idea that the thickening of the disks is due to the buckling instability.

Toomre (1966) was the first to study the buckling of disks. He showed that if the vertical velocity dispersion in a disk is less than about a third of the velocity dispersion in the plane, the disk will be unstable to buckling modes (fire-hose or buckling instability). Toomre's (1966) results were later confirmed by many authors (e.g. Fridman & Polyachenko 1984; Araki 1985). Bar formation in a disk makes the orbits within the bar more eccentric, without affecting much their vertical motions, and thus provides a natural mechanism for the bar to buckle. Combes & Sanders (1981) and Combes et al. (1990) developed an alternative idea for the thickening of bars. They suggested that resonances between the rotation of the bar (Ω_p) and the vertical oscillations of the stars (ν_z) could also make the disk vertically unstable (see also Binney 1981). They noticed that the maximum vertical excursion of the stars in their models occured at the position of both the horizontal ILR ($\Omega_p = \Omega - \kappa/2$, where κ is the epicyclic frequency) and the vertical ILR ($\Omega_p = \Omega - \nu_z/2$), implying that $\kappa \approx \nu_z$ where the boxy/peanut shape is strongest. The buckling instability and the mechanism proposed by Combes et al. (1990) are likely to be complementary processes in the thickening of bars.

Many studies of the 3D orbital structure of non-rotating or slowly rotating triaxial ellipsoids exist, in the context of elliptical galaxies, but their relevance to rapidly rotating bars in disks is far from clear (see, e.g., de Zeeuw & Franx 1991 for a review). Pfenniger (1984) showed that the x_1 orbits, the main family of periodic orbits in 2D barred disks, developed regions of vertical instability when allowed to move in the third dimension. These regions grew as the bar was made thinner. Pfenniger and Friedli (1991) studied the orbital structure in one of the Combes et al. (1990) models. They showed that most stars in the B/PS bar are trapped around orbits of the 2:2:1 family, the 3D generalisation of the x_1 family (2 radial oscillations and 2 vertical oscillations during one revolution). This is probably the case no matter how the bar thickened. Pfenniger (1985) further demonstrated that chaotic motions associated with the vertical instabilities can populate the bulges by semi-ergodic diffusion.

The body of theoretical and modelling work now supporting the buckling and thickening of bars makes this a very appealing mechanism to explain the formation of B/PS bulges in spiral galaxies. However, observational confirmations of this hypothesis are few. Only in a few cases can a bar be directly associated with a B/PS bulge, based on the morphology of the system alone (see, e.g., Bettoni & Galletta 1994 for NGC 4442). The best evidence in favour of the bar-buckling scenario perhaps comes from our own Milky Way. It is now well established that the Galactic bulge is boxy (Weiland et al. 1994) and there is mounting evidence that it is bar-like (see Kuijken 1996 for a recent review). Further support for the bar-buckling mechanism comes from the statistics of the prevalence of these objects, which show that B/PS bulges are present in 20-30% of edge-on spirals (Jarvis 1986; Shaw 1987; de Souza & dos Anjos 1987). This number is consistent with the fraction of strongly barred spirals in more face-on systems (e.g. Sellwood & Wilkinson 1993). The fraction of boxy versus peanut-shaped bulges is also consistent with that predicted from N-body simulations (Combes et al. 1990). Perhaps more importantly, bar-buckling offers a natural way to form B/PS bulges in isolated systems. We recall that B/PS bulges are not found preferentially in clusters (Shaw 1987). Another point in favour of the bar-buckling scenario is that cylindrical rotation is present naturally in all the models. Nevertheless, these arguments are rather indirect. Beside the recent work of Kuijken & Merrifield (1995), which we will discuss in the next section, very little direct confirmation of the validity or the bar-buckling scenario exists.

Forming B/PS bulges out of bars also has some possible drawbacks, although none of these appear particularly threatening at the moment. The general impression one gets from the examination of spirals with a B/PS bulge is that the bulges are shorter, relative to the disk diameter, than the bars seen in face-on systems or the strong bars formed in N-body simulations. However, simple projection effects could easily explain these differences (a given surface-brightness level is reached at a smaller radius in a more face-on disk), and no proper statistics exist. The secular evolution of bars is also poorly known and the subject of many current studies. For examples, bars could be seriously affected by interaction with the disk or a massive spheroidal component, as suggested by Sellwood (1980, 1981) and Weinberg (1985), who studied the transfer of angular momentum between these components. Recent simulations by Debattista & Sellwood (1998) suggest, however, that even though the bar can be slowed down if a dark halo dominates the inner parts of the disk (which, again, is not expected), the bar continues to grow and preserve its boxy/peanut shape. Some efforts have also been directed toward the understanding of mechanisms which have the potential of destroying bars, particularly the growth of a central mass concentration (e.g. Hasan & Norman 1990; Friedli & Benz 1993). However, the destruction of a bar through this mechanism also destroys the boxy/peanut shape (Norman, Sellwood, & Hasan 1996), so it is not inconsistent with the idea of a connection between bars and B/PS bulges.

There are also "hybrid" scenarios for the formation of B/PS bulges. Noguchi (1987) first suggested that interaction can provide a very efficient mechanism to initiate bar formation in disk galaxies. He showed that, in the case of parabolic prograde encounters, his N-body disks had a tendency to form well-developed spiral structures, with strong bar-like patterns in the inner regions. Gerin, Combes, & Athanassoula (1990) also showed that interaction can accelerate bar formation in a disk which is marginally stable. The bar growth rate and final shape are affected by the sense of the interaction (prograde versus retrograde), as well as the strength and pattern speed of the resulting bar (to a lesser extent). Of course, once a bar is formed in this way, it is free to evolve to a boxy/peanut shape in the manner described above (see Mihos et al. 1995). Hybrid scenarios thus couple the accretion and bar-buckling mechanisms. However, hybrid scenarios are really bar-buckling scenarios: interactions initiate bar formation, but the shape of the resulting bar, the issue of interest here, is really due to the subsequent buckling and thickening of the bar.

1.2 Current Status and Thesis Outline

1.2.1 The Pattern Speed of Bars

As we stressed in the our discussion of the structure and dynamics of 2D barred disks, little information is available to constrain the pattern speed of bars. N-body simulations of rotationally supported stellar disks generally yield fast rotating bars, that is bars which end at or just inside their corotation radius (e.g. Sellwood 1981). This view is supported by studies of the orbital structure of barred disks (e.g. Contopoulos 1980), but nothing formally prevents the bars from having a slower pattern speed.

Observationally, it is very difficult to measure the pattern speed of bars. Many methods exist, but only two are widely used. The first method, based on the theory of resonance ring formation pioneered by Schwarz (1981, 1984; see also Byrd et al. 1994), relies on the association of rings in the disk of barred spirals with the location of known resonances. A measurement of the circular velocity curve (usually taken to be the observed rotation curve) then allows to infer the pattern speed. In the second method, the gas flow in a barred spiral galaxy is compared with a series of hydrodynamical models in which the pattern speed of the bar is a free parameter. The best fit model then yields an estimate of the bar pattern speed (see, e.g., Sanders & Tubbs 1980 and Duval & Athanassoula 1983 for early models of NGC 5383). These methods rely on theory and are therefore rather indirect. Tremaine & Weinberg (1984) proposed the only direct method, relying on little theory and observable quantities alone. Unfortunately, the application of the method is very difficult, and it has only been used with success on one object (see Kent 1987; Merrifield & Kuijken 1995).

The above methods have yielded measurements which are generally in agreement with the view that bars are fast rotators. However, most of the evidence is indirect (in the above sense) and, until more bars have their pattern speed directly measured, the issue remains open. Furthermore, both N-body simulations and observational studies have focussed on systems with strong bars, representative of barred spirals of intermediate and early type. Our knowledge of the pattern speed of bars in late-type galaxies is still rudimentary. With recent suggestions that such bars may rotate slowly, with corotation far in the disk (see Elmegreen 1996 for a review of the issue), it has become pressing to obtain direct measurements of the bar pattern speed in range of objects, particularly in late-type spirals. Chapter 2 of this thesis constitutes a small step in that direction.

In Chapter 2, we measure the pattern speed of NGC 2915, a blue compact dwarf (BCD) galaxy with a very extended H I disk (see Meurer, Mackie, & Carignan 1994; Meurer et al. 1996). This gaseous disk extends out to 22 optical scale-lengths and displays a strong spiral structure with a short central bar. We show that the measured pattern speed puts corotation at more than 1.7 bar radii, a value incompatible with self-consistent models of rotationally supported disks. Furthermore, we show that the spiral pattern is unlikely to be caused by interaction, be sustained by swing amplification (Toomre 1981), or be driven by the bar. It may therefore be caused by dark matter, which is known to dominate the dynamics of the system at all radii (Meurer et al. 1996). We reject the possibility of dark matter distributed in a disk, but argue that a massive and extended triaxial dark halo with a slow figure rotation could drive the observed H I structure. We associate the pattern speed of the H I disk with the figure rotation of this dark halo. If this is correct, galaxies like NGC 2915 may provide a new way to study the properties of triaxial dark halos, which is a subject of cosmological significance (see Chap. 2).

1.2.2 The Relationship Between Bars and Boxy/Peanut-Shaped Bulges

Our historical review of the evolution of our knowledge concerning B/PS bulges reflected current ideas about the formation of these objects. Theories of formation for B/PS bulges can loosely be put into two groups: accretion scenarios and bar-buckling scenarios.

The review of accretion mechanisms highlighted many problems of these theories. Most importantly, the range of impact parameters allowed for the accreted material in order to form a B/PS bulge is very restricted (e.g. Binney & Petrou

1985). We argued that the only viable accretion scenario is through the accretion of a small number of intermediate size satellites. Therefore, while it is likely that accretion plays a role in the formation of *some* B/PS bulges, it is unlikely to be the primary formation mechanism. Our approach in this thesis will reflect this view. While we do not specifically target accretion, we will address relevant issues when appropriate.

At this stage, we believe that the emphasis of any study of B/PS bulges should be on testing the bar-buckling scenario. N-body simulations strongly suggest that the buckling and thickening of bars, and the resulting boxy/peanut shape, are a generic property of barred disks (e.g. Combes et al. 1990). Orbital studies in 3D support this view and can explain the final shape of the bars in term of orbit trapping about the 2:2:1 periodic orbit family (e.g. Pfenniger & Friedli 1991). The body of theoretical and modelling work supporting the bar-buckling mechanism for the formation of B/PS bulges is thus extensive and solid. At the moment, the main problem facing buckling scenarios is the lack of observational support. Most evidence in favour of bar-buckling are weak and statistical in nature (e.g. Shaw 1987), and a direct connection between B/PS bulges and bars has been hard to come by. Unfortunately, it is difficult to identify bars in edge-on spirals, where B/PS bulges are most easily seen. The methods used in the past, such as the association of a plateau in the light profile of an edge-on disk with the presence of a bar (e.g. de Carvalho & da Costa 1987), are insecure. A large part of this thesis, Chapters 3 and 4, will thus be devoted to the development of reliable bar diagnostics in edge-on disks. Chapter 5 will make use of these diagnostics to directly test the relationship between bars and B/PS bulges, using a large sample of edge-on spiral galaxies with and without a B/PS bulge.

Kuijken & Merrifield (1995; see also Merrifield 1996) first demonstrated that a kinematical identification of bars in external edge-on spiral galaxies was possible. They showed that periodic orbits in an edge-on barred disk produce characteristic double-peaked line-of-sight velocity distributions, which can then be used to identify an edge-on spiral as barred. In Chapter 3, we refine and develop further the method proposed by Kuijken & Merrifield (1995). We use periodic orbit families as building blocks to model real barred galaxies. We show that the global structure of the position-velocity diagrams (PVDs; i.e. the density of projected material as a function of line-of-sight velocity and projected position) can be used reliably as a bar diagnostic in edge-on disks. The presence of gaps in the PVDs is a direct consequence of the non-homogeneous distribution of orbits in a barred galaxy. We also discuss how the signatures of particular families of periodic orbits can be used to determine the viewing angle with respect to the bar, and to a lesser extent to constrain the mass distribution of an observed galaxy.

In Chapter 4, we develop analogous bar diagnostics specifically for the gas component of spiral galaxies. For that, we use hydrodynamical simulations of barred disks where the gas is treated as test particles (Athanassoula 1992). We show that when a nuclear spiral is formed, corresponding to the existence of an ILR, the presence of gaps in the PVDs between the signature of the nuclear spiral and that of the outer parts of the disk reliably indicates the presence of a bar. These gaps are due to the presence of shocks and inflows in the simulations, which lead to a depletion of the gas in the main and outer bar regions. The shape of the signature of the nuclear spiral can also be used to determine the viewing angle to the bar. These diagnostics are not applicable if no nuclear spiral is present. However, the presence (or absence) of a nuclear spiral puts strong constraints on the properties of an observed galaxy.

In Chapter 5, we present a systematic study of the relationship between bars and B/PS bulges in spiral galaxies. We use the diagnostics developed in Chapters 3 and 4 to search for bars in a large sample of edge-on spiral galaxies with B/PS bulges, and in a smaller control sample of edge-on spirals with more spheroidal bulges. We show that almost all B/PS bulges are due to a thick bar viewed edge-on, while only a few extreme cases may be due to accretion. None of the galaxies in the control sample show evidence for a bar, which suggests conversely that all bars are B/PS. These results strongly support the bar-buckling mechanism for the formation of B/PS bulges.

In Chapter 6, we summarise our results and describe work in progress which is relevant to this thesis. Finally, we discuss some ideas for future work, and describe some interesting spin-offs that this study might have in other fields.

References

Araki, S. 1985, Ph.D. Thesis, Massachusetts Institute of Technology

Athanassoula, E. 1992, MNRAS, 259, 345

Athanassoula, E., & Sellwood, J. A. 1986, MNRAS, 221, 213

Bertola, F., & Capaccioli, M. 1975, ApJ, 200, 439

Bertola, F., & Galletta, G. 1978, ApJ, 226, L115

Bettoni, D., & Galletta, G. 1994, A&A, 281, 1

Binney, J. J. 1976, MNRAS, 177, 19

———. 1978, MNRAS, 183, 501

———. 1980, Phil. Trans. R. Soc. London, 296, 329

———. 1981, MNRAS, 196, 455

Binney, J., & Petrou, M. 1985, MNRAS, 214 449

Burbidge, E. M., & Burbidge, G. R. 1959, ApJ, 130, 20

Byrd, G., Rautiainen, P., Salo, H., Buta, R., & Crocker, D. A. 1994, AJ, 108, 476

Combes, F., Debbasch, F., Friedli, D., & Pfenniger, D. 1990, A&A, 233, 82

Combes, F., & Sanders, R. H. 1981, A&A, 96, 164

Contopoulos, G. 1980, A&A, 81, 198

Contopoulos, G., & Grosbøl, P. 1989, A&A Rev., 1, 261

Contopoulos, G., & Papayannopoulos, T. 1980, A&A, 92, 33

Davies, R. L., Efstathiou, G., Fall, S., Illingworth, G., & Schechter, P. L. 1983, ApJ, 266, 41

Debattista, V. P., & Sellwood, J. A. 1998, ApJ, 493, L5

de Carvalho, R. R., & da Costa, L. N. 1987, A&A, 171, 66

de Souza, R. E., & dos Anjos, S. 1987, A&AS, 70, 465

de Vaucouleurs, G. 1974, in The Formation and Dynamics of Galaxies, ed. J. R. Shakeshaft (Boston:Reidel), 1

de Zeeuw, T., & Franx, M. 1991, ARA&A, 29, 239

Duval, M. F., & Athanassoula, E. 1983, A&A, 121, 297

Elmegreen, E. 1996, in Barred Galaxies, ed. R. Buta, D. A. Crocker, and B. G. Elmegreen (ASP: San Francisco), 505

Faber, S. M. 1977, in The Evolution of Galaxies and Stellar Populations, eds. B. M. Tinsley & R. B. Larson (New Haven: Yale University Observatory), 157

Faber, S. M., & Jackson, R. E. 1976, ApJ, 204, 668

Fridman, A. M., & Polyachenko, V. L. 1984, Physics of Gravitating Systems (New York: Springer-Verlag)

Friedli, D., & Benz, W. 1993, A&A, 268, 65

Gerin, M., Combes, F., & Athanassoula, E. 1990, A&A, 230, 37

Hasan, H., & Norman, C. 1990, ApJ, 361, 69

Hernquist, L., & Quinn, P. J. 1989, ApJ, 342, 1

Hockney, R. W., & Hohl, F. 1969, AJ, 74, 1102

Hodge, P. W., & Merchant, A. E. 1966, ApJ, 144, 875

Hohl, F., & Zang, T. A. 1979, AJ, 84, 585

Illingworth, G. 1977, ApJ, 218, L43

James, R. A., & Sellwood, J. A. 1978, MNRAS, 182, 331

Jarvis, B. J. 1981, Ph. D. Thesis, The Australian National University

———. 1986, AJ, 91, 65

Jarvis, B. J., & Freeman, K. C. 1985a, ApJ, 295, 314

———. 1985b, ApJ, 295, 324

Jensen, E. B., & Thuan, T. X. 1982, ApJS, 50, 421

Kalnajs, A. J. 1971, ApJ, 166, 275

———. 1977, ApJ, 212, 637

Kent, S. M. 1987, AJ, 93, 1062

King, I. R. 1966, AJ, 71, 64

Kormendy, J. 1980, in Proceedings of ESO Workshop on Two-Dimensional Photometry, ed. P. Crane & K. Kjär (Genava:ESO), 191

———. 1982, ApJ, 257, 75

Kormendy, J., & Bruzual, A. G. 1978, ApJ, 223, L63

Kormendy, J., & Illingworth, G. 1982, ApJ, 256. 460

Kuijken, K. 1996, in Barred Galaxies, ed. R. Buta, D. A. Crocker, and B. G. Elmegreen (ASP: San Francisco), 505

Kuijken, K., & Merrifield, M. R. 1995, ApJ, 443, L13

Lynden-Bell, D. 1962, MNRAS, 123, 447

May, A., van Albada, T. S., & Norman, C. A. 1985, MNRAS, 214 131

Merrifield, M. R. 1996, in Barred Galaxies, ed. R. Buta, D. A. Crocker, and B. G. Elmegreen (ASP: San Francisco), 179

Merrifield, M. R., & Kuijken K. 1995, MNRAS, 274, 933

Meurer, G. R., Carignan, C., Beaulieu, S. F., & Freeman, K. C. 1996, AJ, 111, 1551

Meurer, G. R., Mackie, G., & Carignan, C. 1994, AJ, 107, 2021

Miller, R. H., Prendergast, K. H., & Quirk, W. J. 1970, ApJ, 161, 903

Mihos, J. C., Walker, I. R., Hernquist, L., de Oliveira, M. C., & Bolte, M. 1995, ApJ, 447, L87

Noguchi, M. 1987, MNRAS, 228, 635

Norman, C. A., Sellwood, J. A., & Hasan, H. 1996, ApJ, 462, 114

Ostriker, J. P., & Peebles, P. J. E. 1973, ApJ, 186, 467

Pfenniger, D. 1984, A&A, 134, 373

———. 1985, A&A, 150, 112

Pfenniger, D., & Friedli, D. 1991, A&A, 252, 75

Prendergast, K. H., & Tomer, E. 1970, AJ, 75, 674

Raha, N., Sellwood, J. A., James, R. A., & Kahn, F. D. 1991, Nature, 352, 411

Rowley, G. 1986, Ph.D. Thesis, The Australian National University

———. 1988, ApJ, 331, 124

Sandage, A. 1961, The Hubble Atlas of Galaxies (Washington: Carnegie Institution)

Sandage, A., Freeman, K. C., & Stokes, N. R. 1970, ApJ, 160, 831

Sanders, R. H., & Huntley, J. M. 1976, ApJ, 209, 53

Sanders, R. H., & Tubbs, A. D. 1980, ApJ, 235, 803

Sellwood, J. A. 1980, A&A, 89, 296

———. 1981, A&A, 99, 362

Sellwood, J. A., & Wilkinson, A. 1993, Rep. Prog. Phys., 56, 173

Schechter, P. L., & Gunn, J. E. 1979, ApJ, 229, 472

Schwarz, M. P. 1981, ApJ, 247, 77

———. 1984, MNRAS, 209, 93

Shaw, M. A. 1987, MNRAS, 229, 691

Shu, F. H. 1970, ApJ, 160, 89

Sparke, L. S., & Sellwood, J. A. 1987, MNRAS, 225, 653

Toomre, A. 1966, in Geophysical Fluid Dynamics, 1966 Summer Study Program at Woods Hole Oceanographic Institution, ref. no. 66-46, 111

———. 1981, in Structure and Evolution of Normal Galaxies, ed. S. M. Fall & D. Lynden-Bell (Cambridge: Cambridge University Press), 111

Tremaine, S., & Weinberg, M. D. 1984, ApJ, 282, L5

Tsikoudi, V. 1980, ApJS, 43, 365

van Albada, T. S., & Sancisi, R. 1986, Phil. Trans. R. Soc. London A, 320, 447

Weiland, J. L., et al. 1994, ApJ, 425, L81

Weinberg, M. D. 1985, MNRAS, 213, 451

Whitmore, B. C., & Bell, M. 1988, ApJ, 324, 741

Wilson, C. P. 1975, AJ, 80, 175

Chapter 2

The Shape and Figure Rotation of NGC 2915's Dark Halo

Abstract

NGC 2915 is a blue compact dwarf galaxy with a very extended H I disk. This disk shows a short central bar and extended spiral arms, both reaching far beyond the optical component. We use Tremaine & Weinberg's (1984) method to measure the pattern speed of the bar and spiral arms from H I radio synthesis data. Our measurements yield a pattern speed of $\Omega_p = 0.21 \pm 0.06$ km s^{-1} arcsec^{-1} (8.0 ± 2.4 km s^{-1} kpc^{-1} for $D = 5.3$ Mpc), which is inconsistent with the generic property of self-consistent barred disks, that corotation lies just outside the end of the bar. Our adopted bar semi-length $r_b \approx 180''$ puts corotation at more than 1.7 r_b. Because NGC 2915 is isolated, gravitational interactions cannot account for the structure observed in the H I disk. We also demonstrate that the low surface density in the disk and the location of the pseudo-rings make it unlikely that swing amplification (Toomre 1981) or bar-driven spiral arms can explain the bar and spiral pattern. Based on the similarity of the dark matter and H I surface density profiles, we discuss the possibility of dark matter distributed in a disk and following closely the H I distribution. This disk then becomes gravitationally unstable and can naturally form a bar and spiral pattern. However, this explanation is difficult to reconcile with some of the properties of NGC 2915.

Finally, we consider the effect of a massive and extended triaxial dark matter halo with a rotating figure. The existence of such halos is supported by CDM simulations displaying strongly triaxial dark halos with slow figure rotation. The observed structure of the H I disk can then arise through forcing by the rotating triaxial figure. We associate the measured H I pattern speed in NGC 2915 with the rotation of the figure of its dark halo.

2.1 Introduction

About 30% of spiral galaxies are strongly barred. This fraction is roughly doubled if weaker bar-like asymmetries are included. Barred spirals are thus the norm rather than the exception among disk galaxies. The study of barred spiral galaxies is therefore an important field of galactic structure and dynamics, and we refer the reader to the review by Sellwood & Wilkinson (1993).

The form of the potential and the bar pattern speed (Ω_p) are the most important quantities determining the structure and dynamics of a barred spiral disk. N-body simulations of bars (e.g. Sellwood 1981; Combes & Sanders 1981) and analytical calculations (e.g. Contopoulos 1980; Contopoulos & Grosbøl 1989) have shown that for bars to be self-consistent, their pattern speed should be such that corotation occurs just outside the end of the bar. However, measuring the pattern speed of bars is not an easy task and most methods are rather indirect (see, e.g., Schwarz 1981, 1984; Athanassoula 1992b). The method proposed by Tremaine & Weinberg (1984) is the only direct method, relying on little theory and observables alone. However, because of the assumptions it makes, the method is rarely applicable to real galaxies and has been applied successfully to only one object so far (Kent 1987; Merrifield & Kuijken 1995). In this chapter, we apply the Tremaine & Weinberg (TW) method to the galaxy NGC 2915, a blue compact dwarf (BCD) galaxy with a very extended H I disk (Meurer, Mackie, & Carignan 1994, hereafter MMC94; Meurer et al. 1996, hereafter MCBF96). This disk shows a late barred spiral galaxy morphology extending far beyond the optical component.

While the formation of bars is now fairly well understood, the formation of the spiral patterns seen in many spiral disks remains an open issue. Various mechanisms have been proposed to form and maintain spiral patterns. We will consider the most prominent ones here: gravitational interactions (e.g. Noguchi 1987), swing amplification of spiral density waves (Toomre 1981), and bar-driven spiral arms (e.g. Schwarz 1981). We show that none of these is likely to explain the bar and spiral arms structure observed in the H I disk of NGC 2915.

This problem leads us to consider the background mass distribution in NGC 2915. In order to reproduce their flat rotation curves, disks are commonly believed to be immersed in massive dark halos (e.g. Carignan & Freeman 1985). Although the shape of such halos is often assumed to be spherical, there is little observational information on this subject and other shapes are clearly possible (see, e.g., Trimble 1987 and Carr 1994 for reviews). In the particular case of NGC 2915, we demonstrate that a simple rigid spherical halo is unable to explain the properties of the H I disk. We therefore consider other dark matter distributions, including: 1) dark matter distributed in a thin disk following the H I surface density distribution, and 2) dark matter distributed in an extended triaxial halo with a slowly rotating figure.

In § 2.2, we discuss the TW method to measure the pattern speed of bars and review its past applications. In § 2.3, we describe the properties of NGC 2915 and measure its pattern speed. The issues of self-consistency and multiple pattern speeds are mentioned in § 2.4, and in § 2.5 we discuss the possible formation mechanisms for the bar and spiral pattern. In § 2.6, we consider two particular models for the dark matter distribution in NGC 2915. We conclude briefly in § 2.7.

2.2 Pattern Speed Measurement

2.2.1 Indirect Methods

Some indirect methods have been devised to measure the bar pattern speed Ω_p in barred spiral galaxies, and we discuss two of them here. The first one relies on the theory of resonance ring formation (Schwarz 1981, 1984; see also Ousley, Byrd, & Dalla Piazza 1997). It is possible to identify morphological features in the disk of a barred galaxy, such as rings, with the location of known resonances. Using the circular velocity curve and derived epicyclic frequency, the bar pattern speed can then be inferred (see, e.g., Ryder et al. 1996 for recent applications to NGC 1433 and NGC 6300). We apply this method to NGC 2915 in § 2.5. Secondly, it is possible to construct hydrodynamical models of the gas flow in a galaxy (often to reproduce H I observations because of their full kinematical coverage). The hydrodynamical models depend on several parameters of the potential, including Ω_p, so the best fitting model gives an estimate of the bar pattern speed (see, e.g., Lindblad & Kristen 1996 and Lindblad, Lindblad, & Athanassoula 1996 for recent applications to NGC 1300 and NGC 1365). Sellwood & Wilkinson (1993) review many such barred galaxy studies.

Although these indirect methods yield useful information about pattern speeds, it is clearly preferable to have a direct measurement, without relying on theoretical arguments or comparison with dynamical models. We will pursue these indirect methods only as a consistency check of more direct measurements.

2.2.2 Direct Methods

Tremaine & Weinberg (1984) showed that the pattern speed of a barred disk galaxy can be derived from the observed kinematics of a tracer population if (1) there exists a unique, well-defined disk pattern speed Ω_p, and (2) the luminosity density of the tracer satisfies the continuity equation. With these conditions, the pattern speed is given by

$$\Omega_p \sin i = \frac{\int_{-\infty}^{\infty} h(y)dy \int_{-\infty}^{\infty} \Sigma(x,y)[\bar{v}_{los}(x,y) - v_{sys}]dx}{\int_{-\infty}^{\infty} h(y)dy \int_{-\infty}^{\infty} \Sigma(x,y)xdx}, \tag{2.1}$$

where i is the disk inclination, Σ is the surface brightness distribution of the tracer, $\bar{v}_{los}$ is the mean line-of-sight velocity of the tracer, v_{sys} is the systemic velocity of the galaxy, and (x, y) are Cartesian coordinates on the plane of the sky, with the origin at the center of the galaxy and the x-axis parallel to the line of nodes (i.e. the apparent major axis for an intrinsically round disk). These quantities are all observables. The function $h(y)$ is an arbitrary weighting function (see Tremaine & Weinberg 1984). Although the method was intended to measure bar pattern speeds, it can equally be applied to any strong and fairly open pattern, such as spiral arms.

The continuity assumption is valid for a dust-free old stellar population, but may well break down in a dusty system, or when using gas as a tracer (possibility of ionisation, molecular conversion, optical thickness, etc.). In fact, while Tremaine & Weinberg (1984) succeeded in applying their method to an artificial dataset generated from an N-body simulation, they failed on H I data from the barred spiral galaxy NGC 5383 (Sancisi, Allen, & Sullivan 1979). The method is fairly sensitive to noise because only the non-symmetric (i.e. odd in x) part of Σ contributes to the integrals in equation (2.1).

Kent (1987) applied the TW method to the barred spiral galaxy NGC 936. The stellar component of NGC 936 is ideal for this application because it has a strong bar, high surface brightness, high rotation velocity, and is devoid of dust and star formation. The orientation of the system is also favourable. Kent carefully estimated the sources of error in measuring Ω_p. Unfortunately, the relatively poor quality of the kinematical data (by today's standards) led to inconclusive results. He derived an average pattern speed of $\Omega_p = 8.4 \pm 2.9$ km s^{-1} arcsec^{-1} ($\Omega_p = 104 \pm 36$ km s^{-1} kpc^{-1} for $D = 16.6$ Mpc). With Kormendy's (1984) rotation curve, corrected for non-circular motions, and a deprojected bar length of $52''$, corotation then lies between 0.54 and 1.21 bar semi-lengths. This is marginally consistent with the generic result from orbital calculations and self-consistent models of barred spiral galaxies, that corotation occurs just outside the end of the bar (see, e.g., Sellwood 1981; Teuben & Sanders 1985; Athanassoula 1992b).

Merrifield & Kuijken (1995; see also Kuijken & Merrifield 1996) reapplied the TW method to NGC 936, this time with better data and methods. They did not use equation (2.1) directly, but rather used the equivalent formula

$$\Omega_p \sin i = \frac{\langle \bar{v}_{los} \rangle - v_{sys}}{\langle x \rangle} \quad \text{(for a given } y\text{)}, \tag{2.2}$$

where the brackets represent luminosity-weighted averages along the slit. The advantage of this procedure is that the long-slit data can be co-added along the

Table 2.1: Basic Properties of NGC 2915

Quantity	Value	Reference
Position (J2000)	$\alpha = 9^{\rm h}26^{\rm m}11\overset{\rm s}{.}83$	1
Position (J2000)	$\delta = -76°37'35\overset{''}{.}8$	1
Heliocentric Velocity	$V_{\odot} = 468 \pm 5$ km s^{-1}	2,3
Distance	$D = 5.3 \pm 1.6$ Mpc	1
Classification	I0/BCD	1
Total Apparent B Magnitude	$m_{B_T} = 13.34$ mag	1
Total Absolute B Magnitude	$M_{B_T} = -15.90$ mag	1
B Disk Scalelength	$\alpha_B^{-1} = 25\overset{''}{.}6$ (660 pc)	1
Corrected B Central Surface Brightness	$B(0)_c = 22.44$ mag arcsec^{-2}	1
B Holmberg Radius ($\mu_{B,0} = 26.6$ mag arcsec^{-2})	$R_{{\rm Ho},B} = 1\overset{'}{.}9$ (2.93 kpc)	1
Total H I Flux	$F_{\rm HI} = 145$ Jy km s^{-1}	2
Total H I Mass	$M_{\rm HI} = 9.58 \times 10^8\ M_{\odot}$	2
H I Velocity Width	$W_{20} = 170$ km s^{-1}	2
H I Extent ($N_{\rm HI,0} = 5 \times 10^{19}$ cm^{-2})	$R_{\rm HI} = 9\overset{'}{.}7$ (14.9 kpc)	2
Dust Mass	$M_{\rm Dust} = 1.05 \times 10^4\ M_{\odot}$	3
Total Mass (within $r \approx 600'' = 15.4$ kpc)	$M_{\rm Tot} = 2.7 \times 10^{10}\ M_{\odot}$	2

References for Table 2.1.

(1) Meurer et al. 1994; (2) Meurer et al. 1996; (3) Schmidt & Boller 1992.

spatial axis to measure $\langle \bar{v}_{los} \rangle$, and along the dispersion axis to measure $\langle x \rangle$, yielding higher signal-to-noise measurements. To obtain an unbiased measure of $\langle \bar{v}_{los} \rangle$, Merrifield & Kuijken (1995) also used a deconvolution algorithm allowing for asymmetric Doppler broadening of the spectral lines. They obtained a well-defined average pattern speed of $\Omega_p = 4.8 \pm 1.1$ km s^{-1} arcsec^{-1} ($\Omega_p = 60 \pm 14$ km s^{-1} kpc^{-1} for $D = 16.6$ Mpc). This value puts corotation at $69 \pm 15''$, or 1.3 ± 0.3 bar radii, in good agreement with theoretical expectations.

2.3 NGC 2915

2.3.1 Background

NGC 2915 is a nearby relatively isolated BCD galaxy. MMC94 carried out optical imaging and spectroscopy of NGC 2915 to study its structure, stellar populations, and star formation history. MCBF96 obtained H I synthesis data to study the neutral hydrogen distribution and kinematics, and to model the overall mass distribution (including dark matter). Table 2.1 summarises the basic properties of NGC 2915.

The photometry of MMC94 shows that NGC 2915 has two distinct stellar populations: (1) an exponential red diffuse population in the outer parts ($r \geq 35'' = 0.90$ kpc), with a scale length $\alpha_B^{-1} = 25\farcs6$ (660 pc), an extrapolated central surface brightness $B(0)_c = 22.44$ mag arcsec^{-2} (corrected for inclination and extinction), and constant color; and (2) a slightly peaked core population ($r < 35''$) with increasingly bluer color toward the center. The diffuse population is similar to dwarf elliptical galaxies, but the core is lumpy, contains a young stellar population, and is the locus of high mass star formation. Spectroscopy in the core shows strong Balmer and Ca II H+K absorption lines, and strong narrow emission lines with ratios typical of high excitation low metallicity H II regions. A velocity difference of 60 km s^{-1} is detected across the inner galaxy. If this gradient is due solely to rotation, it corresponds to a deprojected rotational velocity $V_r = 50 \pm 21$ km s^{-1} at $r = 32''$ (neglecting the effects of the bubbles seen in Hα by Marlowe et al. 1995). The associated mass $M_{\rm Core} = 4.8 \times 10^8$ $M_\odot$ for the optical core, with a mass-to-light ratio $M_{\rm Core}/L_B = 1.3$ $M_\odot/L_{B,\odot}$.

The neutral hydrogen observations of NGC 2915 (MCBF96) reveal an H I distribution very different from the optical. Figure 2.1 shows the naturally weighted total H I intensity map overlaid on an optical image of NGC 2915. The H I distribution is unusually extended, up to 5.1 $D_{{\rm Ho},B}$ (22.7 α_B^{-1}), and it has a striking late-type barred spiral galaxy morphology, with two extended spiral arms starting at the end of a central bar. At higher resolution, the H I bar is resolved into two clouds; its semi-length is about $2\farcm4$ (3.7 kpc), and it corresponds roughly in position, orientation, and size to the optical emission. The H I surface density profile is tabulated in Table 2.2. The total H I mass is $M_{\rm HI} = 9.6 \times 10^8$ $M_\odot$, while the H I mass in the bar is only about $5 - 7.5 \times 10^7$ $M_\odot$. Figure 2.2 shows the MCBF96 naturally weighted H I velocity field of NGC 2915, again overlaid on an optical image. It clearly shows the pattern of a rotating disk (with an oval distortion), and suggests the presence of a warp in the outer parts. MCBF96 derived a rotation curve for NGC 2915 using the standard tilted ring algorithm ROTCUR (Begeman 1989). The position angle varies by about 15° and the inclination by about 10° outside of the barred region (where the effects of the bar and a possible warp are hard to disentangle), supporting the presence of a warp in the outer disk. The H I velocity dispersion outside the barred region is the usual $\sigma_v \approx 8$ km s^{-1}, but increases up to 40 km s^{-1} in the central regions (see Table 2.2), a value comparable to the rotation velocities obtained from ROTCUR. This indicates that pressure support is important in the center. MCBF96 applied an asymmetric drift correction to the rotation curve to produce the "circular velocity curve" needed for mass modelling. The circular velocity is tabulated in Table 2.2. It increases rapidly with radius in the inner parts, reaching 80 km s^{-1} by $r = 150''$ (3.9 kpc); it then stays flat until $r = 400 - 450''$ (10.3–11.6 kpc), and increases again up to $\approx$90 km s^{-1} at the last measured point ($r \approx 600'' = 15.4$ kpc).

MCBF96 constructed three-component mass models to interpret the circular

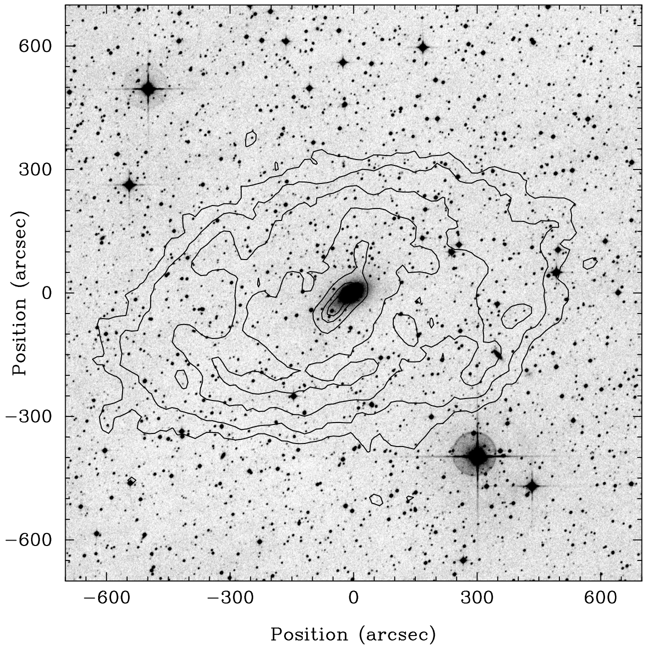

Figure 2.1: Meurer et al. (1996) naturally weighted total H I intensity map, overlaid on an optical image of NGC 2915 (Digitized Sky Survey). The beam is $45'' \times 45''$. Contours levels are 2.5, 7.5, 15, 25, 50, 75, and 90 percent of the peak H I surface brightness of 3.1 Jy beam^{-1} km s^{-1} ($N_{HI} = 1.71 \times 10^{21}$ cm^{-2}).

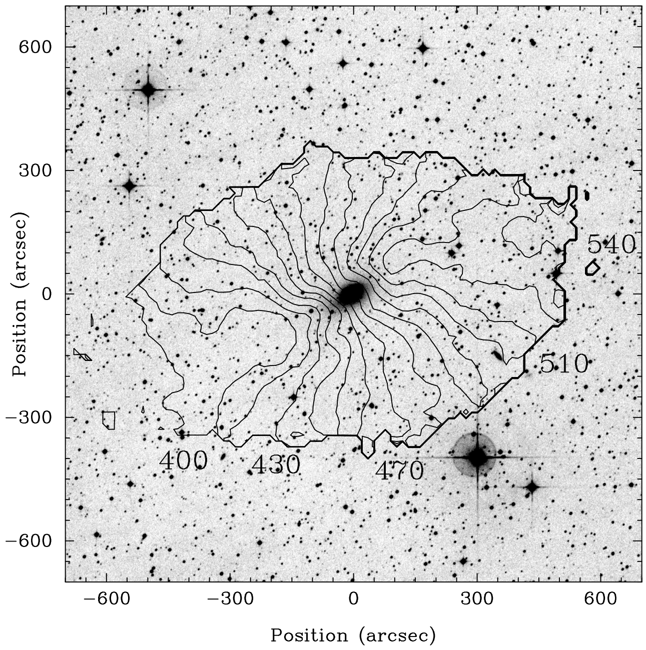

Figure 2.2: Meurer et al. (1996) naturally weighted H I velocity field, overlaid on an optical image of NGC 2915 (Digitized Sky Survey). The beam is $45'' \times 45''$ and the velocity resolution is 6.62 km s^{-1}. Contours are heliocentric velocities separated by 10 km s^{-1}. A few contours are identified on the map.

Table 2.2: Structural and Kinematical Profiles of NGC 2915

r (arcsec)	$\mu_{\rm HI}$ ($M_\odot$ pc^{-2})	μ_B $\left(\frac{B \text{ mag}}{\text{arcsec}^{-2}}\right)$	V_c (km s^{-1})	$\sigma_{V,\rm HI}$ (km s^{-1})	Ω $\left(\frac{\text{km s}^{-1}}{\text{arcsec}^{-1}}\right)$	κ $\left(\frac{\text{km s}^{-1}}{\text{arcsec}^{-1}}\right)$
27.5	8.90	22.55	39.0	33.4	1.42	2.37
52.5	6.35	23.97	53.0	28.8	1.01	1.76
77.5	4.10	25.11	65.0	23.0	0.84	1.44
102.5	3.17	26.26	72.7	20.8	0.71	1.15
127.5	2.53	27.20	76.0	15.6	0.60	0.93
152.5	2.26	28.26	79.2	11.9	0.52	0.81
177.5	2.32	29.32	81.4	10.7	0.46	0.69
202.5	2.36	30.38	82.5	9.9	0.41	0.60
227.5	2.12	31.44	82.8	9.2	0.36	0.48
252.5	1.75	32.50	80.4	10.1	0.32	0.41
277.5	1.49	33.56	80.4	10.1	0.29	0.42
302.5	1.41	34.62	80.9	9.3	0.27	0.38
327.5	1.46	35.68	80.7	8.7	0.25	0.35
352.5	1.43	36.74	80.8	8.3	0.23	0.34
377.5	1.23	37.80	82.0	8.8	0.22	0.32
412.5	1.09	39.28	82.3	8.6	0.20	0.30
457.5	0.89	41.19	83.8	8.1	0.18	0.28
502.5	0.67	43.10	85.5	8.1	0.17	0.28
547.5	0.48	45.01	88.5	8.1	0.16	0.29
592.5	0.32	46.92	93.9	7.7	0.16	0.30

velocity curve. Their models were composed of: (1) a stellar disk, obtained from the B-band surface brightness profile of MMC94 (the mass-to-light ratio M/L_B is a free parameter); (2) an H I disk, based on their observations; and (3) a spherical dark halo (two density distributions were used, both with a central density ρ_0 and core radius r_c as free parameters). All models are dominated by dark matter at all radii. In fact, NGC 2915 is one of the "darkest" disk galaxies known. Its dark matter core is very dense and compact. MCBF96's best fit model[1] has $M/L_B = 1.2\ M_\odot/L_{B,\odot}$, $\rho_0 = 0.10 \pm 0.02\ M_\odot$ pc^{-3}, and $r_c = 1.13 \pm 0.15$ kpc, yielding a total mass $M_T = 2.7 \times 10^{10}\ M_\odot$, $M_T/L_B = 76\ M_\odot/L_{B,\odot}$, and $M_{dark}/M_{luminous} = 19$ within the last measured point.

2.3.2 Pattern Speed

Using the H I data of MCBF96, we now attempt to measure the pattern speed Ω_p of the figure in the disk of NGC 2915. As mentioned in § 2.2.2, the continuity equation imposes a strong constraint on the applicability of the TW method, and

[1]Their model D, with a dark matter density distribution $\rho(r) = \rho_0[1 + (r/r_c)^2]^{-1}$.

gaseous systems are usually thought to be poor candidates for a measurement. NGC 2915 is an unusual galaxy, however, and we argue that the TW method should work for its H I distribution. Firstly, because the stellar component of NGC 2915 is confined to the inner regions of its H I distribution, and the star-forming core to the very center of the H I bar, there is no source of ionising photons over most of the H I disk (except for the weak metagalactic radiation field, and possibly some radiation from the distant core seen by the warped regions). Furthermore, the H I column density is low enough in most of the disk (where the velocity dispersion $\sigma_v \approx 8$ km s^{-1}) that optical thickness problems should not affect the observed H I intensity. Only in the inner parts of the bar, where the optical disk lies, does the column density reach $N_{HI} = 10^{21}$ cm^{-2}, but there the H I velocity dispersion is larger ($\sigma_v \approx$ 20–40 km s^{-1}), so again the optical depth is expected to be low. At this stage, we have no information on possible H I-molecule conversion. However, the low H I column density suggests that this effect is not important. For these reasons, and because the bar and spiral arms pattern is clear and strong, we believe that the TW method applied to the H I distribution and kinematics of NGC 2915 should give a realistic measure of its pattern speed. We note that the orientation of the system is ideal, with the disk at intermediate inclination and the bar oriented about 30° from the major axis of the disk.

We apply the TW method to NGC 2915 using MCBF96's naturally weighted total H I intensity map and velocity field (Fig. 2.1 and 2.2). Additional structural and kinematical parameters describing the galaxy are needed to use the TW method (see § 2.2.2), but these are all provided by the tilted-ring analysis of MCBF96. We use averages of their parameters in the outer disk, outside of the barred region ($r > 150''$): the center of the disk $(x_c, y_c) = (63, 64)$ (in $14''$ pixels), $v_{sys} = 467$ km s^{-1}, and the position angle of the line of nodes PA = 117°. We use equation (2.1) directly, without a weighting function $h(y)$, and for all possible positions y (equivalent to using $h(y) = \delta(y - y_o)$ for each y_o). Because the major axis traces the position of the line of nodes, y is effectively the position of the integration axis along the minor axis of the galaxy. Each offset y provides an independent measurement of the pattern speed. The coordinate system is shown in Figure 2.3, and Figure 2.4a shows the derived pattern speeds as a function of the offset y. The measurements are consistent for most offsets. Only for a few isolated points and for offsets between 0 and $200''$ on the NE side of the galaxy (positive offsets) are the values of $\Omega_p \sin i$ significantly discrepant (recall that the TW method assumes a unique pattern speed for the whole disk, so all offsets should yield similar pattern speeds).

This discrepant region is associated with the northernmost of the two clouds identified by MCBF96, located at the northern end of the bar. Around that region, both the total H I intensity distribution and the velocity field show a

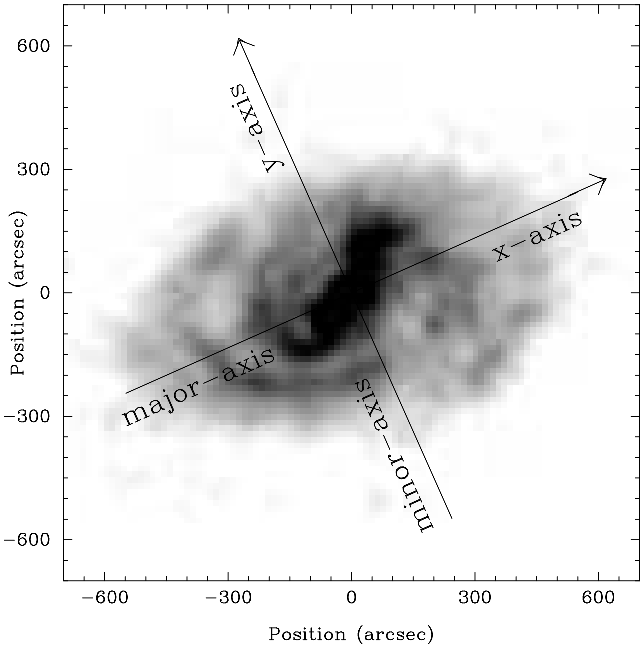

Figure 2.3: Schematised view of the "set-up" required for the Tremaine-Weinberg method calculations (eq. [2.1]), overlaid on a grayscale image of Meurer et al. (1996) naturally weighted total H I intensity map ($45'' \times 45''$ beam).

strong deviation from their large-scale pattern. The discrepancy in the derived pattern speeds therefore probably arises from the fact that the cloud breaks the pattern in the density distribution and/or the velocity field, an effect to which equation (2.1) is very sensitive. Away from this problem region, the pattern speed is well-defined: the entire SW half of the galaxy and the farthest regions in the NE half yield fairly consistent values for $\Omega_p \sin i$. Therefore, we believe that the TW method works for the H I distribution in NGC 2915 and that it gives a reliable estimate of the pattern speed.

In our calculations, we assumed that the parameters required for the TW method measurements were fixed over the whole disk. The center of the disk is well-defined, and only the x-component of the center (x_c) affects the calculations anyway. The systemic velocity is also well constrained, with a small uncertainty of a few km s^{-1}. On the other hand, as shown by the tilted-ring analysis of MCBF96, both the inclination i and position angle PA vary significantly with radius in NGC 2915. A change in inclination affects the pattern speed measurements only through the deprojection. However, a change in position angle materially affects the calculations themselves. We have therefore reapplied the TW method to the H I data of NGC 2915, using a range of values for x_c, v_{sys}, and PA. Although no combination of parameters yields perfectly equal pattern speeds over the whole minor axis, most cases with plausible values show a regular behaviour, with only a restricted range of offsets having very discrepant measurements. A typical good

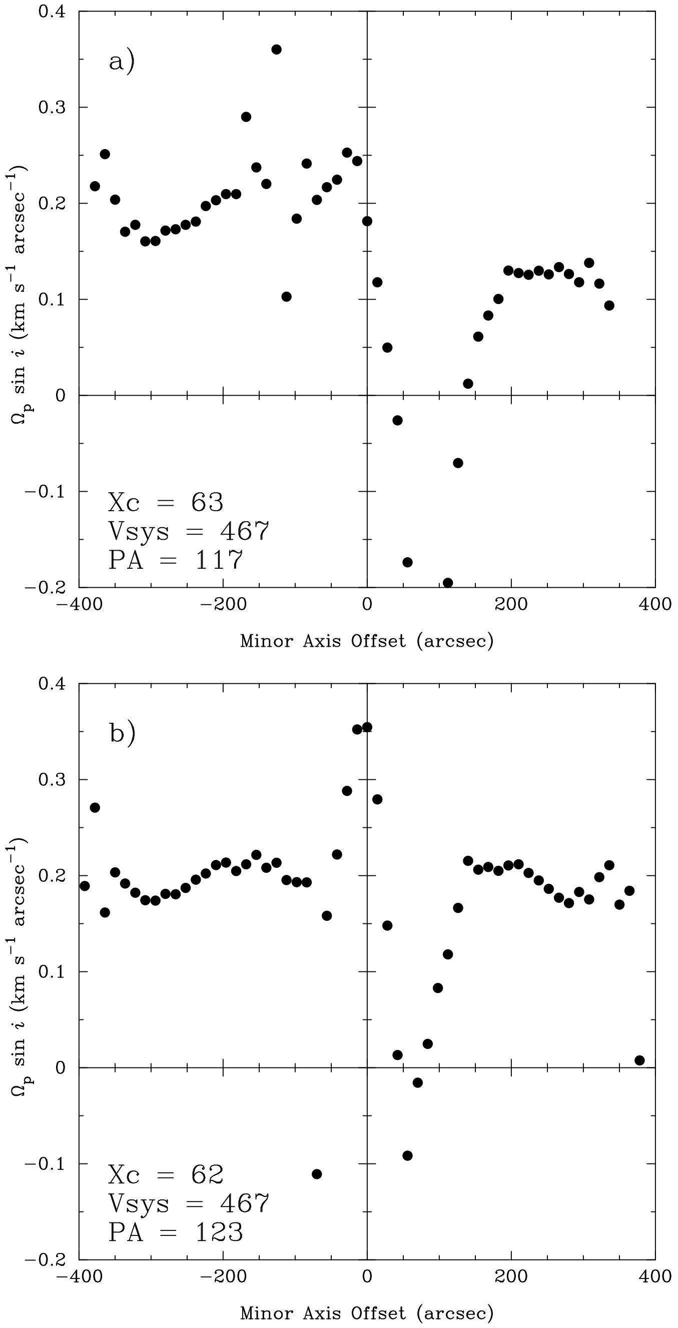

Figure 2.4: Tremaine-Weinberg method measurements of the pattern speed in NGC 2915. (a) shows the case with Meurer et al. (1996) tilted-ring model best fit parameters, while (b) shows a typical good case. Parameters are indicated in the bottom-left corner of each plot.

case is presented in Figure 2.4b.

For all of our estimates, the flat portions of the $\Omega_p \sin i$ "distribution" always lie between $\Omega_p \sin i = 0.12$ km s^{-1} arcsec^{-1} and $\Omega_p \sin i = 0.22$ km s^{-1} arcsec^{-1}. We therefore adopt $\Omega_p \sin i = 0.17 \pm 0.05$ km s^{-1} arcsec^{-1} ($\Omega_p \sin i = 6.6 \pm 1.9$ km s^{-1} kpc^{-1} for $D = 5.3$ Mpc) as our estimate of the pattern speed in NGC 2915. The uncertainty given here represents half the range of measured values for $\Omega_p \sin i$, and is not a standard error estimate. From the outer parts of the disk again, we get an average inclination $i = 56 \pm 3°$. This gives a deprojected pattern speed $\Omega_p = 0.21 \pm 0.06$ km s^{-1} arcsec^{-1} (8.0 ± 2.4 km s^{-1} kpc^{-1}).

The 30% uncertainty in Ω_p is comparable to that achieved by Merrifield & Kuijken (1995) for NGC 936, but is still large given that we are using gas kinematics with the advantage of full two-dimensional spatial coverage. On the other hand, our error estimate (half the range of measured values) is very conservative. As suggested by Tremaine & Weinberg (1984), we tried using odd weighting functions (e.g. $h(y) = \delta(y - y_0) - \delta(y + y_0)$; y_c now affects the calculations directly). Such weighting eliminates the contribution of perturbations with odd azimuthal wavenumbers to the integrals in equation (2.1), and diminishes the effect of centering errors. However, it did not improve our results, as discrepant regions on one side of the minor axis contaminate the combined measurements from both sides. Although we cannot exclude the possibility that the continuity equation is not fully satisfied for the H I in some parts of NGC 2915 (particularly the central regions), we believe that the main sources of error in our measurements are the presence of some short-lived features in the disk (such as the structure seen near the NW cloud) and the warped structure. Tremaine & Weinberg (1984) note that a warp may affect the pattern speed determination, acting as a non-axisymmetric perturbation with zero pattern speed. We repeated the calculations using only the inner barred region of the galaxy, but the results were inconclusive (it is far from clear that the method should work in such a case, as the integrals in eq. [2.1] should extend over the whole system).

2.4 The Nature of the Pattern

2.4.1 Self-Consistent Bars

Many N-body studies show that rotationally supported stellar disks are globally unstable to bisymmetric distortions and quickly form strong bars. This is seen in both two-dimensional (e.g. Sellwood 1981; Athanassoula & Sellwood 1986) and three-dimensional (e.g. Combes & Sanders 1981; Raha et al. 1991) simulations. These instabilities can be identified with the dominant linear modes found in analytical global stability analyses of axisymmetric disks (e.g. Kalnajs 1971, 1977).

The main characteristic of the stellar bars formed in such self-consistent disks is that the bar ends at or just inside its corotation radius (where $\Omega_p = \Omega(r)$).

Orbital calculations in barred disk potentials also support the view that bars end at or just inside corotation (see, e.g., Contopoulos 1980; Athanassoula 1992a; for a review of the orbital structure of barred disks, see Contopoulos & Grosbøl 1989). The argument is that the bar-shaped x_1 orbits, believed to support self-consistent bars, extend close to but not past corotation.

This generic property of self-consistent barred disks does not appear to hold in NGC 2915. The gaseous bar ends well within corotation. We take the ends of the bar to be defined by the regions where the density of the rectangular-shaped central component in the H I distribution drops rapidly; these are also the regions where the spiral arms start. The observed semi-length of the bar is then 145″, with a deprojected value $r_b \approx 180''$. Using our adopted pattern speed, $\Omega_p = 0.21 \pm 0.06$ km s^{-1} arcsec^{-1} (see § 2.3.2), and MCBF96's circular velocity curve (see Table 2.2), corotation occurs at a radius $r_{co} = 390^{+\infty}_{-80}$ arcsec (see Fig. 2.7). Therefore, the ratio of corotation to the bar semi-length is very large, $r_{co}/r_b > 1.7$, and the bar is slowly rotating.

Such a bar is inconsistent with the properties of self-consistent disks and we must conclude that the bar is not due to global bisymmetric unstable modes. It is thus unlikely that the bar and disk are self-gravitating. This is not surprising, considering that the galaxy is completely dominated by dark matter, even in the central regions (MCBF96).

In that regard, we note that dense dark halos have been predicted to slow down bars significantly, as the bar can transfer angular momentum to the outer disk and halo through dynamical friction (see Sellwood 1980; Weinberg 1985; Debattista & Sellwood 1998). These studies used purely stellar models, with a stellar bar, and excluded gaseous processes, some of which may lead to an increase of the bar pattern speed (see, e.g., Kalnajs 1996). They therefore probably overestimate the deceleration rate of the bar, especially in very gaseous disks. Nevertheless, it would be interesting to know how relevant this process might be to the situation observed in NGC 2915.

2.4.2 Bar or Spiral Arms Pattern Speed?

The TW method measures the pattern speed of a disk, taken to be unique. While it was designed to measure the pattern speed of bars, it equally applies to any pattern present in a disk, as long as it is strong enough. It is therefore important to establish the component from which we are measuring the pattern speed. Are we measuring the pattern speed of the bar, the spiral arms, or a common pattern speed for both?

Sellwood & Sparke (1988) suggest that spiral arms in barred spiral galaxies could have a different (lower) pattern speed than the bar. Their work was aimed primarily at explaining the presence of dust lanes on the inner edge of spiral arms in many objects. A lower pattern speed for the spiral would allow the gas to overtake the pattern and therefore lie within its corotation radius in that region, while still retaining the view that bars end at or just inside *their* corotation radius. Sellwood & Sparke (1988) support their suggestion with N-body simulations of barred galaxies showing outer spiral patterns slower than the bar patterns (e.g. Sparke & Sellwood 1987).

Tagger et al. (1987) and Sygnet et al. (1988) develop the idea that the non-linear coupling of (two) modes with different pattern speeds could sustain spiral structure for a long time. For the mechanism to be efficient, resonances of the two patterns must be closely spaced. They observe this effect in many N-body simulations, where the corotation radius of the bar and the inner Lindblad resonance (ILR) of the spiral pattern are very close (this is also the region where the bar ends and the spiral arms begin). The beat wave generated is then axisymmetric and close to its Lindblad resonance and couples non-linearly to the bar and spiral arms.

If we assume that the pattern speed measured here is that of the spiral arms, and that the corotation radius of the bar lies close to the ILR of the spiral pattern, as suggested by Tagger et al. (1987) and Sygnet et al. (1988), we obtain a bar corotation radius $r_{co} < 50''$ (see Fig. 2.7), well inside the bar observed in H I ($r_b \approx 180''$). Such a view would be difficult to defend, considering the body of analytical and numerical work which requires the corotation radius to lie *at least* just outside the bar. This is a strong indication that we are in fact measuring the pattern speed of the bar.

Furthermore, considering the form of equation (2.1), we see that for small minor axis offsets ($y < 90''$), both the central (barred) and external (non-barred) regions of the galaxy contribute to the integrals, while for large offsets ($y > 90''$), the integration axis does not cross the barred region and only the outer parts of the disk contribute to the pattern speed calculations. If the bar and spiral arms had significantly different pattern speeds, we would expect the TW method to fail for small offsets. However, excluding the discrepant points 0–200$''$ on the NE side (which we attribute to a large H I cloud, see § 2.3.2), the pattern speed measurements yield a relatively constant value for all offsets (and for most reasonable combinations of parameters). Considering the relatively small extent of the barred region and the importance of the flux in the outer parts of the disk, it might appear that the spiral arms could dominate the contribution to the integrals in equation (2.1) even for small offsets. This is not so, however: for small offsets, both the barred region and outer parts of the disk contribute significantly to the numerator. It is therefore very likely that a unique pattern speed is being measured. This view is further strengthened by the fact that the spiral arms in NGC 2915 appear to start from the end of the bar (although Sellwood & Sparke 1988 showed that this is not a strong argument).

We therefore adopt the view that the pattern speed which we have measured in § 2.3.2 *is* the unique, common pattern speed of both the bar and the spiral arms, although we cannot entirely exclude yet the possibility that it is the pattern speed of the spiral arms alone.

2.5 The Origin of the Pattern

Having measured the speed of the H I pattern in NGC 2915, we now consider the origin of the pattern. Is the pattern a phenomenon of the disk itself, or is it driven by other mechanisms?

2.5.1 Gravitational Interactions

Tidal triggering is a potentially important way to form bars, especially in dense environments. In the case of parabolic prograde planar encounters, Noguchi (1987) found that self-consistent disks (with a static halo) develop strong spiral structures over their entire length, with a bar-like pattern in their inner regions. Gerin, Combes, & Athanassoula (1990) also showed that interaction with a companion accelerates bar formation. The sense of interaction (prograde or retrograde) affects the bar growth rate and shape, with lesser effects on the strength and pattern speed of the resulting bar. When a bar already exists, its strength and pattern speed can again be affected by an interaction.

It seems unlikely that such scenarios can explain the structure of the disk in NGC 2915. No evidence of interaction is seen in the H I data of MCBF96, and the only catalogued potential interaction partner for NGC 2915, within 5°, is a low luminosity, low surface brightness object, SGC 0938.1-7623, at a radius of $42'$ (projected distance of 65 kpc at the distance of NGC 2915). This object does not have a catalogued optical or H I velocity so, although there are no indications that NGC 2915 is interacting, we cannot definitively exclude this possibility.

2.5.2 Swing Amplification

Swing amplification (Toomre 1981) can generate spiral arms in a disk as transient tidal features. Although Toomre (1981) considered a stellar disk, his treatment should equally apply to gaseous disks. Swing amplification is a local cooperative effect: shear, epicyclic motions, and self-gravity all contribute to support the spiral pattern, originally excited by a small disturbance. The epicyclic motions resonate with the shear flow as the spiral pattern wraps, and the spiral arms are sustained. The self-gravity of the arms leads to a gravitational instability (Goldreich & Lynden-Bell 1965). These effects can be summarised (somewhat simplified by neglecting the shear) in Toomre's parameter X, given by

$$X = \frac{\lambda}{\lambda_{\rm crit}}, \tag{2.3}$$

where

$$\lambda_{\rm crit} = \frac{4\pi^2 {\rm G}\mu}{\kappa^2}, \tag{2.4}$$

μ is the surface density, and κ is the epicyclic frequency. Swing amplification is efficient for $X \lesssim 3$ (including the effects of shear and random motions; see, e.g., Fig. 7 of Toomre 1981). For an extended disk, we can write $\lambda = 2\pi r/m$, where m is the azimuthal wavenumber of the spiral pattern considered, and

$$X(r) = \frac{r\kappa(r)^2}{2\pi {\rm G} m\mu(r)} \tag{2.5}$$

(see Athanassoula, Bosma, & Papaioannou 1987).

Figure 2.5 shows $X(r)$ for NGC 2915 for two and four-armed spiral patterns. We use the surface density of the luminous matter only (gaseous and stellar), assuming that the dark matter is not responsive to the density perturbation created by the spiral pattern (Toomre 1981 considered a fixed halo). In Figure 2.5a, only the H I distribution from MCBF96 is included (see Table 2.2). It is clear from the figure that $X(r)$ is nowhere near a value of 3. In fact, even for $m = 4$, $X(r) \gtrsim 10$ for almost all radii. In Figure 2.5b, the stellar content is also included. To construct the surface density profile, we used the B surface brightness profile of MMC94 for $r < 125''$, and an extrapolation of their exponential fit to the outer parts of the disk for larger radii ($B(0)_c = 22.44$ mag arcsec^{-2} and $\alpha_B^{-1} = 25\farcs6$), with $M/L_B = 1.2\ M_\odot/L_{B,\odot}$ (as in the adopted mass model of MCBF96). The resulting surface brightness profile is tabulated in Table 2.2. Even with the stellar component, $X(r) \gtrsim 10$ for most radii. Small values of $X(r)$ are present in the inner regions only: $X(r) \leq 5$ for $r < 75''$ only. We note that those regions are within the rapidly rising portion of the rotation curve, where the bar resides and the shear is low, while swing amplification relies on shear to amplify the spiral pattern.

The work by Toomre (1981) refers to a flat rotation curve, $V_c(r) =$ constant, which is not exactly the case here. The amplification criterion $X \lesssim 3$ increases for higher shear rates (e.g. $X \lesssim 6$ for a Keplerian rotation curve, $V_c(r) \propto r^{-1/2}$) and decreases for smaller shear (e.g. $X \lesssim 1.5$ for $V_c(r) \propto r^{1/2}$; Toomre, private

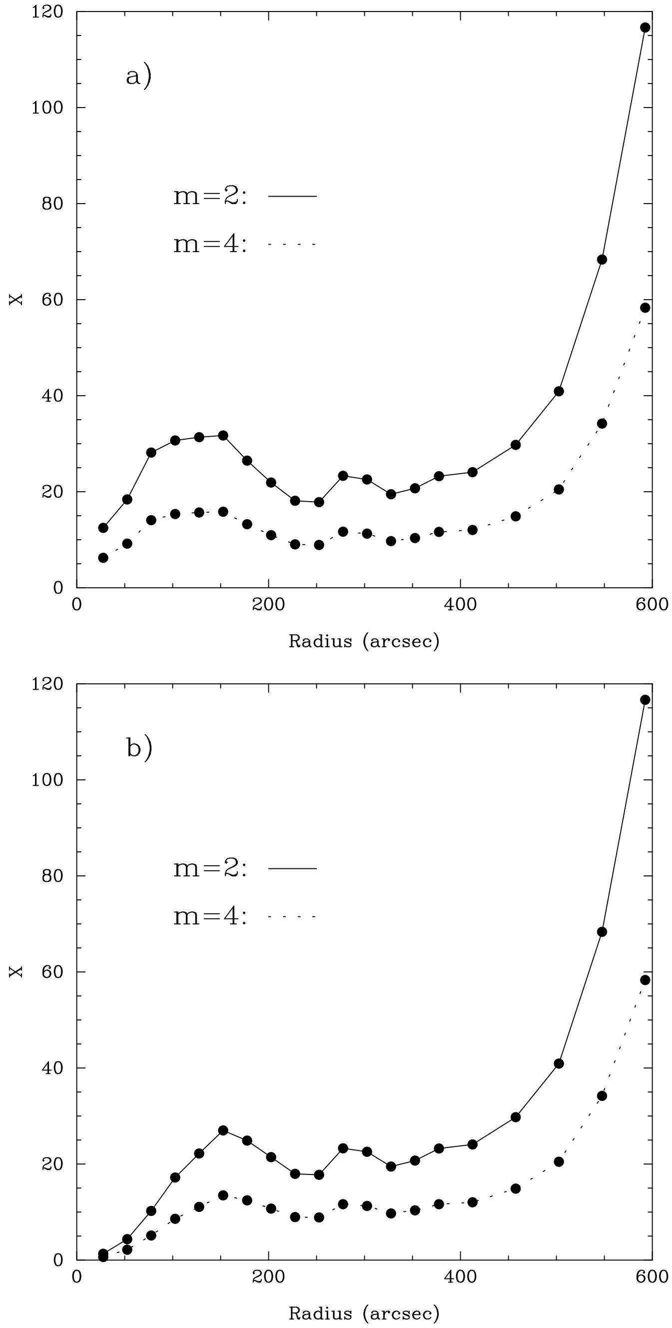

Figure 2.5: Calculated swing amplifier parameter $X(r)$ (eq. [2.5]) for two-armed ($m = 2$, full lines) and four-armed ($m = 4$, dotted lines) spiral patterns in NGC 2915. (a) shows $X(r)$ when only the H I distribution is taken into account, while in (b) both the H I and the stellar components are considered. $X \lesssim 3$ is required for swing amplification.

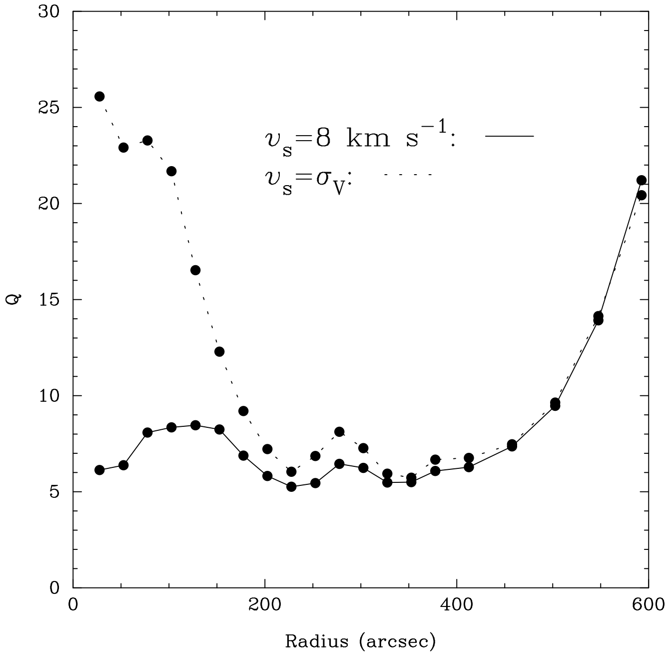

Figure 2.6: Calculated stability parameter $Q(r)$ (eq. [2.6]) in NGC 2915. The full line shows $Q(r)$ considering a fixed sound speed $v_s(r) = 8$ km s^{-1}, equal to the velocity dispersion in the outer parts of the H I disk. The dotted line assumes $v_s(r) = \sigma_v(r)$. $Q(r)$ scales directly with $v_s(r)$. $Q \gtrsim 2$ curbs swing amplification.

communication). So, if anything, the constraints on swing amplification are even stronger in the case of NGC 2915, especially in the inner parts.

Toomre's (1964) stability parameter Q also affects the efficiency of the swing amplifier mechanism. The stellar disk of NGC 2915 does not extend into the spiral pattern region, so we consider only the gaseous disk. Then,

$$Q(r) = \frac{v_s(r)\kappa(r)}{\pi \mathrm{G}\mu(r)}, \tag{2.6}$$

where v_s is the sound speed of the gas, taken here as the velocity dispersion. As Q increases, the maximum swing amplification factor decreases. For $V_c(r) =$ constant, $Q \gtrsim 2$ curbs most of the amplification (see, again, Fig. 7 of Toomre 1981). The criterion becomes $Q \gtrsim 3$ for $V_c(r) \propto r^{-1/2}$ and $Q \gtrsim 1.5$ for $V_c(r) \propto r^{1/2}$ (Toomre, private communication). Figure 2.6 shows $Q(r)$ for NGC 2915 using both a constant velocity dispersion, equal to the velocity dispersion in the outer parts of the H I disk, and the H I velocity dispersion profile of MCBF96, tabulated in Table 2.2. We see that $Q(r) \gtrsim 5$ everywhere, so the amplification factor would be small. In particular, $Q(r)$ is high in the inner regions. The sound speed would have to be less than 2–3 km s^{-1} to make $Q(r) < 2$ over a significant range of radii. Even then, X would still be too high for the swing amplifier to work efficiently.

Given the behaviour of $X(r)$ and $Q(r)$, and if the analogy between Toomre's

(1981) stellar treatment and our gaseous treatment is at least qualitatively valid[2], it seems clear that swing amplification cannot explain the spiral pattern seen in NGC 2915. Furthermore, given the very extended mass distribution of NGC 2915, it is unlikely that the observed spiral pattern results from an edge-mode, as discussed by Toomre (1981).

At this point, we conclude that the bar and spiral arms pattern in NGC 2915 is unlikely to be caused by gravitational interaction or swing amplification. We must therefore search for an alternative formation mechanism.

2.5.3 Bar-Driven Spiral Arms: Resonance Ring Formation

For a given rotation curve, the bar pattern speed is the most important parameter affecting the structure of barred spiral galaxies. It determines the presence and position of the resonances, and therefore the kind and extent of the orbit families present in the disk (see Sellwood & Wilkinson 1993). We can use the theory of resonance ring formation (Schwarz 1981, 1984; Byrd et al. 1994) to see if our pattern speed measurement is consistent with the location of the (pseudo-)rings seen in NGC 2915, and therefore determine whether the spiral arms could be driven by the bar.

Using the MCBF96 circular velocity curve, we can calculate the angular frequency of circular motion Ω and the associated Lindblad precession frequencies $\Omega + \kappa/2$, $\Omega - \kappa/2$, and $\Omega - \kappa/4$ (see Table 2.2). These are shown in Figure 2.7, along with the measured pattern speed and the position of various features in the disk of NGC 2915.

The first points in Figure 2.7 are affected by beam smoothing in the inner regions, but suggest the presence of an ILR ($\Omega_p = \Omega - \kappa/2$) at $r < 50''$. Nuclear rings are believed to be associated with ILRs, and usually form easily recognisable annuli of H II regions in the inner parts of galaxies. The shallower the rotation curve in the inner parts, the larger the nuclear ring formed (Byrd et al. 1994). However, no such ring is visible in the photometry of MMC94 or in the Fabry-Perot Hα images of Marlowe et al. (1995). The resolution of the H I data of MCBF96 is too low to resolve a ring of radius smaller than about $1\overset{'}{.}5$.

The inner spiral arms seen in the total H I intensity map of NGC 2915 (Fig. 2.3) appear to form a pseudo-ring just outside the end of the bar, at a deprojected radius of $215 \pm 15''$. Inner rings are usually associated with the inner ultraharmonic resonance ($\Omega_p = \Omega - \kappa/4$) which, in this case, occurs between about $190''$ and $340''$. This is just consistent with the position of the inner pseudo-ring.

[2] As mentioned by Toomre (1981) based on the work of Bardeen (1975) and Aoki, Noguchi, & Iye (1979), gaseous disks are probably more stable than stellar ones, which would strengthen our conclusions.

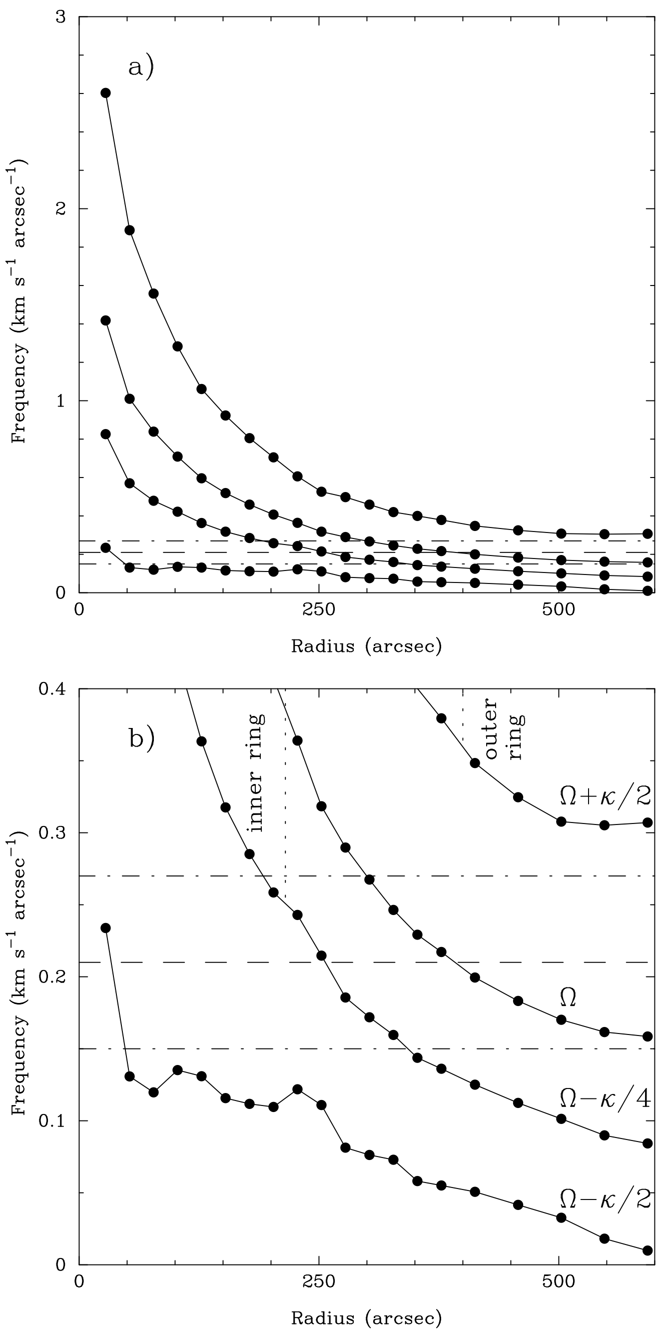

Figure 2.7: (a) Calculated Lindblad precession frequencies for NGC 2915 (solid lines). From top to bottom, they are, respectively, $\Omega + \kappa/2$, Ω, $\Omega - \kappa/4$, and $\Omega - \kappa/2$. The dashed line shows the adopted pattern speed Ω_p, while the dot-dashed lines show the range of values allowed by the uncertainty on Ω_p. (b) is simply an enlargement of (a), but in addition the position of various features in the disk of NGC 2915 are indicated (dotted vertical lines).

The outer spiral arms seen at the edge of the H I disk in Figure 2.3 form an outer pseudo-ring at $r = 400 \pm 15''$. Outer rings are normally associated with the outer Lindblad resonance ($\Omega_p = \Omega + \kappa/2$). However, the $\Omega + \kappa/2$ curve in Figure 2.7 does not intersect the range of measured values for Ω_p, which suggests that no outer Lindblad resonance is present in the disk of NGC 2915. Thus, no outer ring would be expected.

In summary, resonance ring theory has only limited success in explaining the position of the various (pseudo-)rings in NGC 2915 (nuclear, inner, and outer rings). It could be that the pattern in NGC 2915 is still evolving, and that the spiral arms are still in the process of forming rings. This seems unlikely, however, since no nuclear ring is detected, and the timescale for nuclear ring formation is very short (10^7 – 10^8 yr; Combes 1993). Stellar mass loss or gas infall can delay the formation of rings (Schwarz 1981), but these are improbable as most of the H I disk is devoid of stars and NGC 2915 is isolated.

Petrou & Papayannopoulos (1986) proposed a mechanism to terminate bars well within their corotation radius. This mechanism requires the presence of a 1:1 resonance ($\Omega_p = \Omega - \kappa$) in the bar, however, so it is clear from Figure 2.7 that it is not relevant in the case of NGC 2915.

We therefore conclude that the structures seen in the disk of NGC 2915 are probably not due to resonances and that the spiral pattern is not driven by the bar.

2.6 Dark Matter and the Structure of NGC 2915

The H I data of MCBF96 showed that NGC 2915 is dominated by dark matter, even in the central optical region of its disk. We now discuss the possible relations between the properties of this dominant dark matter distribution and the properties of the H I pattern.

2.6.1 Rotationally Supported Disk Dark Matter

Pfenniger, Combes, & Martinet (1994; see also Pfenniger & Combes 1994) propose that the dark matter required dynamically in disk galaxies is in the form of rotationally supported cold molecular gas. This idea is attractive for NGC 2915, as it would also provide the extra disk mass needed to explain the formation of the bar and spiral arms through gravitational instabilities in the disk. Unfortunately, observing such cold gas directly is difficult (for H_2, see Combes & Pfenniger 1997; for CO, see Lequeux & Allen 1993 and Wilson & Mauersberger 1994).

Figure 2.8a shows how much additional mass is required in the *disk* for the swing amplification mechanism to be efficient ($X = 3$ everywhere in the disk; see § 2.5.2). Similarly, Figure 2.8b shows how much additional disk matter is needed to lower Q to a value of 2 at all radii (the value required to make the disk gravitationally responsive). For comparison, we plot in Figure 2.8c the observed H I surface density (Table 2.2) and the projected surface density of the dark isothermal *sphere* used by MCBF96 to model the circular velocity curve (their model D), rescaled by a large constant factor (47.7).

The similarity between the H I and the dark matter surface density profiles seen in Figure 2.8c has been noticed before in other objects (e.g. Bosma 1978, 1981; Carignan & Beaulieu 1989; Broeils 1992) and has been interpreted as possible evidence that the H I and the dark matter are somehow associated. Here, we see in addition a qualitative similarity between the observed H I surface density profile and the surface density profile of the additional disk matter required to make $Q(r) = 2$ (Fig. 2.8b). It is tempting to regard this as further evidence that the dark matter is distributed in a disk and follows relatively closely the distribution of the neutral hydrogen. However, the increase in disk surface density required to make the swing amplifier work efficiently ($X = 3$ over most of the disk; Fig. 2.8a) would lower Q even more, and would make the disk unstable to axisymmetric modes. Figure 2.9 shows the ratio of the surface density obtained by imposing $X(r) = 3$ to Kennicutt's (1989) critical surface density for star formation in disks. This ratio is well above unity for the entire disk, so we would expect to see evidence for active star formation in the outer H I disk if the swing amplifier was working, which is not observed. It is therefore unlikely that dark matter distributed in a disk can account for all the properties of the H I disk in NGC 2915.

Nevertheless, it would be interesting to see if this type of argument, based on Toomre's (1964) parameter Q and the presence of a spiral pattern, could be used in other spiral galaxies to argue for the presence of a substantial amount of disk dark matter (see Quillen & Sarajedini 1998 for a similar application to intermediate-redshift galaxies).

2.6.2 Slowly Rotating Triaxial Dark Halos

Simulations of hierarchical structure formation in cold dark matter (CDM) universes predict that the dark halos around galaxies are triaxial in the mean, with some tendency to prolate shapes (Frenk et al. 1988; Dubinski & Carlberg 1991; Warren et al. 1992). The triaxiality and oblateness are slightly stronger in the outer parts but are almost independent of the halo mass and of the ratio V_r/σ_v (rotational velocity to velocity dispersion), indicating that the halos are supported by anisotropic velocity dispersions. The total angular momentum vector is nevertheless preferentially aligned with the minor axis of the mass distribution at all radii. When dissipation is included, the halos become more oblate while the

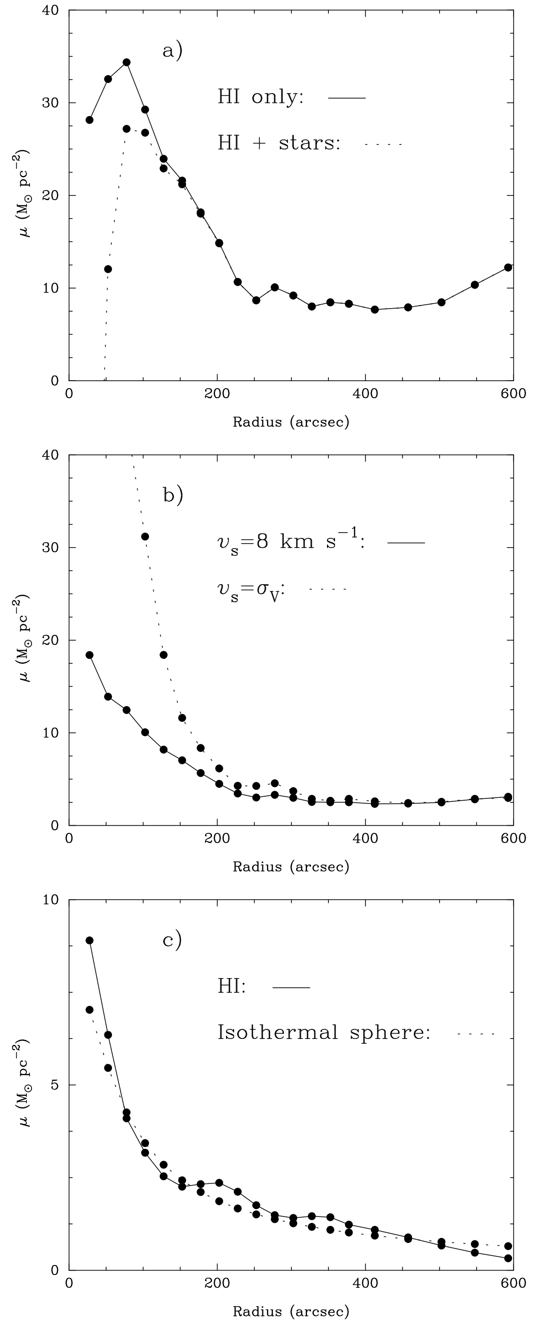

Figure 2.8: (a) Calculated disk dark matter surface density required to make the swing amplifier parameter $X(r) = 3$ (eq. [2.5]) for a two-armed ($m = 2$) spiral pattern in NGC 2915. The full line shows μ_{DM} when only the H I distribution is taken into account, while for the dotted line both the H I and the stellar component are considered. (b) Calculated disk dark matter surface density required to make the stability parameter $Q(r) = 2$ (eq. [2.6]). The full line shows μ_{DM} considering a fixed sound speed $v_s(r) = 8$ km s^{-1}, while the dotted line assumes $v_s(r) = \sigma_v(r)$. $Q(r)$ scales directly with $v_s(r)$. (c) The full line shows $\mu_{\rm HI}$, the observed disk surface density of H I (Table 2.2), while the dotted line shows μ_{DM}, the projected dark matter surface density of the dark isothermal sphere used by MCBF96 to model the rotation curve (their model D).

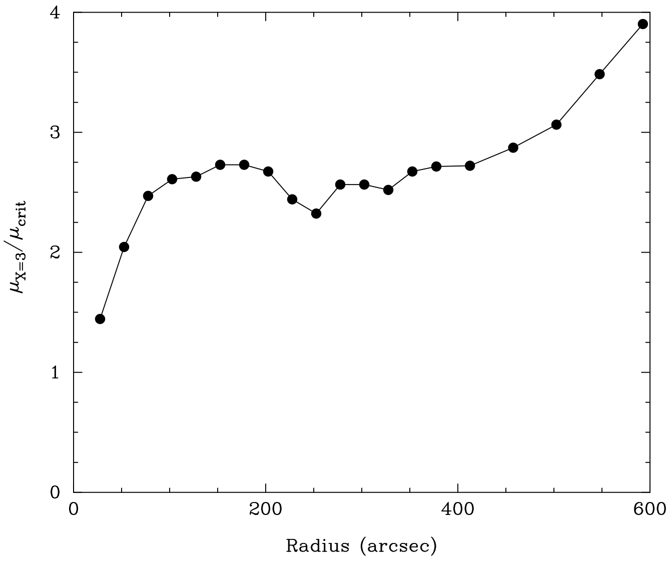

Figure 2.9: Calculated ratio of the total surface density required to make the swing amplifier parameter $X(r) = 3$ (eq. [2.5] with $m = 2$) to the critical surface density required for star formation in galactic disks (Kennicutt 1989) in NGC 2915.

flattening is unchanged (Dubinski 1994).

Observationally, the constraints on the shape of galactic halos remain weak. Polar-ring galaxies (e.g. Sackett et al. 1994) and the flaring (e.g. Olling 1995) and warping (e.g. Sparke 1984a) of the outer H I disk of spirals are usually used to constrain the three-dimensional structure of halos. Such studies often indicate flattened and sometimes triaxial dark halos (see also Becquaert & Combes 1997; Olling 1996), but are as yet inconclusive.

We now consider the possibility that the dark halo of NGC 2915 is triaxial, with its figure rotating slowly about the rotation axis of the H I disk, and that the H I bar and spiral arms in NGC 2915 are due to the forcing of the H I disk by this massive, extended, and rotating triaxial halo. The halo would then act much like a very massive, slowly rotating bar. This would readily explain why there is a unique pattern speed for the bar and spiral arms and why the bar ends so far from corotation (see § 2.4). The situation which we are proposing is similar to that of rotating weak oval distortions in disks, which are able to maintain an open spiral pattern to large radii (see, e.g., Hunter et al. 1988). This is in contrast to a more conventional bar, where the quadrupole term decreases too rapidly outside corotation (where the bar ends) to maintain an extended spiral structure.

The straight line of nodes of the warp in NGC 2915 (MCBF96) supports the suggestion of a triaxial halo. Displacements between the angular momentum vectors of the inner and outer regions of disks arise naturally in CDM models because of tidal torques. In an axisymmetric but flattened potential, the line of nodes would wrap quickly, but in a triaxial potential, the principal axes of the halo provide natural directions with which the warp can align (see Binney 1992 for a review of warps). Furthermore, an annulus of orbits circulating around the short axis of a triaxial halo becomes vertically unstable if the figure rotates, providing a natural way to excite a warp, although this may happen too far in the disk (outside corotation for prograde orbits) to be of interest here (Binney 1978, 1981; see also Sparke 1984b).

While the studies mentioned above (Frenk et al. 1988; Dubinski & Carlberg 1991; Warren et al. 1992; Dubinski 1994) have shown that the dark halos in CDM cosmological simulations can be strongly triaxial and have well-defined angular momentum properties (with flat rotation curves extending up to the core), only their instantaneous shapes and the rotational motions within the figures (streaming) have been studied. As far as we are aware, there has been no systematic study of the *figure* rotation of these triaxial halos.

Prompted by this work, Pfitzner began a study, to be published elsewhere, of the figure rotation of halos in a set of large CDM structure formation simulations. The shape distribution of the halos varies systematically with both radius and mass, but for our current purposes it suffices to say that many halos are significantly triaxial, as in other studies. Following the orientation of each halo over time, Pfitzner finds that a subset of the triaxial halos exhibits steady figure rotation about the minor axis. The statistics of how many halos in the simulations have figure rotation is confused by numerical resolution issues, but the fraction is clearly significant. To verify that these results are not due to transient phenomena, one of the rotating halo candidates was extracted and evolved in isolation. The halo displayed no systematic change of density or shape over the simulation time of 5 Gyr. Figure 2.10 shows that the figure of this triaxial halo rotates as a solid body with constant pattern speed. Hence we conclude that at least some halos in these CDM simulations do exhibit genuine steady slow figure rotation over a Hubble time. These simulations are not yet directly applicable to the example of NGC 2915, because the halos are much more massive than that of NGC 2915. They do, however, suggest that an underlying triaxial dark halo with figure rotation may make an important contribution to the dynamics of the outer H I disk of some galaxies. If this is correct, it also offers another way to measure the shape of (triaxial) dark halos from detailed H I velocity field, using methods similar to those of Franx, van Gorkom, & de Zeeuw (1994).

The slow pattern speeds found in the present study and in the above simulations are interesting in the context of recent work by Miwa & Noguchi (1998). They made N-body simulations of barred galaxies in which the bars arose (1) spontaneously in marginally stable disks, and (2) through the effect of a tidal interaction in more stable disks. The pattern speeds of the spontaneous bars are fast, with corotation near the ends of the bars, as expected in self-consistent sys-

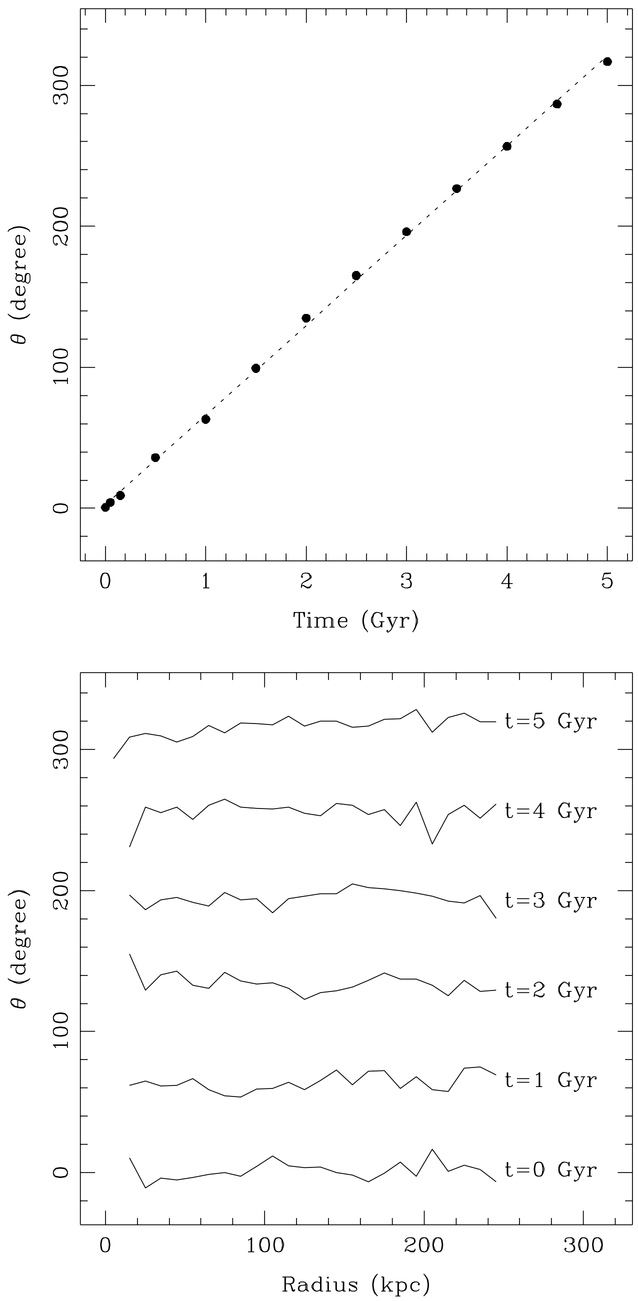

Figure 2.10: (a) Orientation of the major axis of a dark halo formed in a CDM simulation as a function of time. The angle θ is measured in a fixed plane perpendicular to the minor axis (the rotation axis). Filled circles show the mean orientation of the halo as a function of time, and the dotted line is a linear fit to the data, showing that the halo pattern speed is constant. (b) Orientation of the major axis of the same halo as a function of radius (in isodensity-defined shells) for selected times, showing that the halo rotates as a solid-body.

tems. In the tidally induced bars, however, the pattern speeds are generally much slower, and the bars appear to be limited by the ILR, rather than by corotation. In particular, any relatively large tidal disturbance leads to a slow pattern speed, independent of the original properties of the disk. These results may be relevant to the pattern speeds of the triaxial dark halos formed in CDM simulations, in which the triaxiality results at least partially from tidal effects during the aggregation process.

2.7 Conclusions

We applied the method of Tremaine & Weinberg (1984) to measure the pattern speed in the galaxy NGC 2915, using neutral hydrogen as the tracer and radio synthesis data. NGC 2915 is a BCD galaxy with a very extended H I disk showing an open barred spiral morphology. It is also completely dominated by dark matter. Our measurements yield a pattern speed of 8.0 ± 2.4 km s^{-1} kpc^{-1} for $D =$ 5.3 Mpc. This pattern speed is inconsistent with the generic property of self-consistent barred disks, that corotation occurs just outside the end of the bar. Our adopted bar length puts corotation at more than 1.7 bar radii. We considered the possibility that the bar and spiral arms have different pattern speeds and demonstrated that this is unlikely.

NGC 2915 is isolated, so gravitational interactions are unlikely to explain the strong bar and spiral pattern observed in the H I disk. Because the surface density in the disk is so low, Toomre's (1981) swing amplification mechanism is also unable to explain the origin of the pattern. Furthermore, resonance ring theory fails to predict successfully the position of the pseudo-rings seen in the disk of NGC 2915, indicating that the spiral arms are not driven by the bar itself.

This lead us to consider two scenarios, involving different dark matter distributions, to explain the structure and dynamics of the H I disk in NGC 2915. Firstly, we considered dark matter in near-circular motion, distributed in a disk, and following closely the distribution of H I, as suggested by the similarity of the dark matter and H I surface density profiles. This does not appear to work: if the dark matter disk is dense enough for the swing amplifier to function efficiently, then the disk becomes unstable to axisymmetric disturbances and we would expect to see evidence for star formation, which is not observed. Secondly, we considered the effects of dark matter distributed in a massive pressure-supported halo with extended triaxiality, like the halos seen in CDM cosmological simulations. In addition, we required the halo to have a slow figure rotation. Such figure rotation is seen in the preliminary analysis of a set of CDM simulations, which show triaxial halos with figure rotation constant over many Gyr. This kind of model can explain the structure in the disk of NGC 2915 through the torques exerted by the slowly rotating triaxial figure of the dark halo.

The H I structure in NGC 2915 is visible because the H I synthesis observations were made at a relatively high spatial resolution (beam FWHM of about 650 pc for the uniformly weighted data and about 1150 pc for the naturally weighted data). As far as we are aware, NGC 2915 is the only galaxy showing such structure in an extended H I disk. If our suggestions are correct, it would be very desirable to have H I observations of similar spatial resolution for other nearby galaxies with extended H I disks, as those observations could provide similar probes of the dynamics of their dark halos. Our argument on figure rotation also relies heavily on the theory of the forcing of structures by oval distortions in disk galaxies, in a situation which is not precisely analogous to that in NGC 2915. Hydrodynamical simulations of gas disks in the potentials of triaxial halos with figure rotation would thus be very welcome.

References

Aoki, S., Noguchi, M., & Iye, M. 1979, PASJ, 31, 737

Athanassoula, E. 1992a, MNRAS, 259, 328

———. 1992b, MNRAS, 259, 345

Athanassoula, E., Bosma, A., & Papaioannou, S. 1987, A&A, 179, 23

Athanassoula, E., & Sellwood, J. A. 1986, MNRAS, 221, 213

Bardeen, J. M. 1975, in Dynamics of Stellar Systems, ed. A. Hayli (Reidel), 297

Becquaert, J.-F., & Combes, F. 1997, A&A, 325, 41

Begeman, K. G. 1989, A&A, 223, 47

Binney, J. J. 1978, MNRAS, 183, 779

———. 1981, MNRAS, 196, 455

———. 1992, ARA&A, 30, 51

Bosma, A. 1978, Ph.D. Thesis, University of Groningen

———. 1981, AJ, 86, 1971

Broeils, A. H. 1992, A&A, 256, 19

Byrd, G., Rautiainen, P., Salo, H., Buta, R., & Crocker, D. A. 1994, AJ, 108, 476

Carignan, C., & Beaulieu, S. 1989, ApJ, 347, 760

Carignan, C., & Freeman, K. C. 1985, ApJ, 294, 494

Carr, B. 1994, ARA&A, 32, 531

Combes, F. 1993, in N-Body Problems and Gravitational Dynamics, ed. F. Combes & E. Athanassoula (Paris: Observatoire de Paris), 137

Combes, F., & Pfenniger, D. 1997, A&A, 327, 453

Combes, F., & Sanders, R. H. 1981, A&A, 96, 164

Contopoulos, G. 1980, A&A, 81, 198

Contopoulos, G., & Grosbøl, P. 1989, A&A Rev., 1, 261

Debattista, V. P., & Sellwood, J. A. 1998, ApJ, 493, L5

Dubinski, J. 1994, ApJ, 431, 617

Dubinski, J., & Carlberg, R. G. 1991, ApJ, 378, 496

Franx, M., van Gorkom, J. H., & de Zeeuw, T. 1994, ApJ, 436, 642

Frenk, C. S., White, S. D. M., Davis, M., & Efstathiou, G. 1988, ApJ, 327, 507

Gerin, M., Combes, F., & Athanassoula, E. 1990, A&A, 230, 37

Goldreich, P., & Lynden-Bell, D. 1965, MNRAS, 130, 125

Hunter, J. H., Ball, R., Huntley, J. M., England, M. N., & Gottesman, S. T. 1988, ApJ, 324, 721

Kalnajs, A. J. 1971, ApJ, 166, 275

———. 1977, ApJ, 212, 637

———. 1996, in Barred Galaxies and Circumnuclear Activity, ed. Aa. Sandqvist & P. O. Lindblad (Berlin: Springer), 165

Kennicutt, R. C. Jr. 1989, ApJ, 344, 685

Kent, S. M. 1987, AJ, 93, 1062

Kormendy, J. 1984, ApJ, 286, 132

Kuijken, K., & Merrifield, M. R. 1996, in Barred Galaxies, ed. R. Buta, D. A. Crocker, & B. G. Elmegreen (San Francisco:ASP), 215

Lequeux, J., & Allen, R. J. 1993, A&A, 280, L23

Lindblad, P. A. B., & Kristen, H. 1996, A&A, 313, 733

Lindblad, P. A. B., Lindblad, P. O., & Athanassoula, E. 1996, A&A, 313, 65

Marlowe, A. T., Heckman, T. M., Wyse, R. F. G., & Schommer, R. 1995, ApJ, 438, 563

Merrifield, M. R., & Kuijken K. 1995, MNRAS, 274, 933

Meurer, G. R., Carignan, C., Beaulieu, S. F., & Freeman, K. C. 1996, AJ, 111, 1551 (MCBF96)

Meurer, G. R., Mackie, G., & Carignan, C. 1994, AJ, 107, 2021 (MMC94)

Miwa, T., & Noguchi, M. 1998, ApJ, 499, 149

Noguchi, M. 1987, MNRAS, 228, 635

Olling, R. P. 1995, AJ, 110, 591

———. 1996, AJ, 112, 481

Ousley, D., Byrd, G., & Dalla Piazza C. 1997, BAAS, 29, 1333

Petrou, M., & Papayannopoulos, T. 1986, MNRAS, 219, 157

Pfenniger, D., & Combes, F. 1994, A&A, 285, 94

Pfenniger, D., Combes, F., & Martinet, L. 1994, A&A, 285, 79

Quillen, A. C., & Sarajedini, V. L. 1998, AJ, 115, 1412

Raha, N., Sellwood, J. A., James, R. A., & Kahn, F. D. 1991, Nature, 352, 411

Ryder, S. D., Buta, R. J., Toledo, H., Shukla, H., Staveley-Smith, L., & Walsh, W. 1996, ApJ, 460, 665

Sackett, P. D., Rix, H.-W., Jarvis, B. J., & Freeman, K. C. 1994, ApJ, 436, 629

Sancisi, R., Allen, R. J., & Sullivan, W. T. 1979, A&A, 78, 217

Schmidt, K.-H., & Boller, T. 1992, ANac, 313, 189

Schwarz, M. P. 1981, ApJ, 247, 77

———. 1984, MNRAS, 209, 93

Sellwood, J. A. 1980, A&A, 89, 296

———. 1981, A&A, 99, 362

Sellwood, J. A., & Sparke, L. S. 1988, MNRAS, 231, 25

Sellwood, J. A., & Wilkinson, A. 1993, Re. Prog. Phys., 56, 173

Sparke, L. S. 1984a, ApJ, 280, 117

———. 1984b, MNRAS, 211, 911

Sparke, L. S., & Sellwood, J. A. 1987, MNRAS, 225, 653

Sygnet, J. F., Tagger, M., Athanassoula, E., & Pellat, R. 1988, MNRAS, 232, 733

Tagger, M., Sygnet, J. F., Athanassoula, E., & Pellat, R. 1987, ApJ, 318, L43

Teuben, P. J., & Sanders, R. H. 1985, MNRAS, 212, 257

Toomre, A. 1964, ApJ, 139, 1217

———. 1981, in Structure and Evolution of Normal Galaxies, ed. S. M. Fall & D. Lynden-Bell (Cambridge: Cambridge University Press), 111

Tremaine, S., & Weinberg, M. D. 1984, ApJ, 282, L5

Trimble, V. 1987, ARA&A, 25, 425

Warren, M. S., Quinn, P. J., Salmon, J. K., & Zurek, W. H. 1992, ApJ, 399, 405

Weinberg, M. D. 1985, MNRAS, 213, 451

Wilson, T. L., & Mauersberger, R. 1994, A&A, 282, L41

Chapter 3

Bar Diagnostics in Edge-On Spiral Galaxies. I. The Periodic Orbits Approach

Abstract

We develop diagnostics to detect the presence and orientation of a bar in an edge-on disk, using its kinematical signature in the position-velocity diagram (PVD) of a spiral galaxy observed edge-on. Using a well-studied barred spiral galaxy mass model, we briefly review the orbital properties of two-dimensional non-axisymmetric disks and identify the main families of periodic orbits. We use those families as building blocks to model real galaxies and calculate the PVDs obtained for various realistic combinations of periodic orbit families and for a number of viewing angles with respect to the bar. We show that the global structure of the PVDs is a reliable bar diagnostic in edge-on disks. Specifically, the presence of gaps between the signatures of the periodic orbit families in the PVDs follows directly from the non-homogeneous distribution of the orbits in a barred galaxy. Similarly, material in the two so-called forbidden quadrants of the PVDs results from the elongated shape of the orbits. We show how the shape of the signatures of the dominant x_1 and x_2 families of periodic orbits can be used efficiently to determine the viewing angle with respect to the bar and, to a lesser extent, to constrain the mass distribution of an observed galaxy. We also address the limitations of the models when interpreting observational data.

3.1 Introduction

The classification of spiral galaxies along the Hubble sequence (Sandage 1961) is difficult for highly inclined systems. The tightness of the spiral arms and the degree to which they are resolved into stars and H II regions are useless criteria when dealing with edge-on galaxies. Only one main criterion remains: the relative importance of the bulge with respect to the disk. The problem is more acute when it comes to determining if a galaxy is barred, as there is no easy way to identify a bar in an edge-on system. The presence of a plateau in the light distribution of a galaxy (typically the light profile along the major axis) is often taken to indicate the presence of a bar (e.g. de Carvalho & da Costa 1987; Hamabe & Wakamatsu 1989). However, this method has two serious shortcomings: axisymmetric features might be mistaken for a bar (e.g. a lens would probably produce a very similar effect) and end-on bars are likely to be missed (their plateau would be both short and, in early type barred galaxies, superposed on the steep light profile of the bulge). The studies of the galaxy NGC 4762 by Burstein (1979a, 1979b), Tsikoudi (1980), Wakamatsu & Hamabe (1984), and Wozniak (1994) illustrate the uncertainties resulting from using such a method. It is clear that a photometric or morphological identification of bars in edge-on spiral galaxies is problematic and unsatisfactory.

Kuijken & Merrifield (1995; see also Merrifield 1996) were the first to demonstrate that a kinematical identification of bars in external edge-on spiral galaxies was possible. They calculated the projection of periodic orbits in a barred galaxy model for various lines-of-sight and showed that an edge-on barred disk produces characteristic double-peaked line-of-sight velocity distributions which would not occur in an axisymmetric disk. Equivalent methods have been used for many years in Galactic studies (e.g. Peters 1975; Mulder & Liem 1986; Binney et al. 1991; Wada et al. 1994; more recently Weiner & Sellwood 1995; Beaulieu 1996; Sevenster et al. 1997; Fux 1997a,b), since the position-velocity diagrams (PVDs) of external galaxies are analogous to the longitude-velocity diagrams of the aforementioned studies.

In this chapter, we aim to develop bar diagnostics using the PVDs of edge-on spiral galaxies in the same spirit as Kuijken & Merrifield (1995). We will, however, study the signature of each family of periodic orbits separately (before joining them to obtain a global picture) and examine how it depends on the viewing angle. We use a well-studied mass model, a well-defined method to populate the orbits, and we explore a large number of periodic orbit families. Our results should be used as a *guide* to interpret observations of the stellar and/or gaseous kinematics in edge-on spiral galaxies. While the gas streamlines can be approximated by periodic orbits, the presence of shocks will modify this behaviour significantly. Also, the collisionless stellar component is not confined to periodic or regular (quasi-periodic) orbits, and there can be a non-negligible fraction of stars on irregular orbits. Chapter 4 and Athanassoula & Bureau (1999; hereafter Paper III) will provide bar diagnostics similar to those developed here, but using, respectively, hydrodynamical and N-body simulations.

The identification of bars in edge-on spiral galaxies is not a goal in itself but rather a tool allowing us to deepen our understanding of bars. The particular line-of-sight to edge-on spirals allows us to view the kinematics of the *entire* symmetry plane of the disk in one single observation (assuming the disk is transparent) and provides a unique way of studying the dynamics of the disk globally. More importantly, such a diagnostic represents a unique opportunity to study the vertical structure of bars, of which very little is known observationally. Three-dimensional N-body simulations have shown that bars tend to buckle soon after their formation, and settle with an increased thickness and vertical velocity dispersion, appearing boxy or peanut-shaped when viewed edge-on (e.g. Combes & Sanders 1981; Combes et al. 1990; Raha et al. 1991). Beside the clues provided by the Galaxy (e.g. Blitz & Spergel 1991; Binney et al. 1991; Weiland et al. 1994), little observational data exist to directly test this hypothesis. In fact, the vertical light distribution of a bar has never been measured. Kuijken & Merrifield (1995) are the only ones to have actively searched for the kinematical signature of a large-scale bar in edge-on spiral galaxies with boxy/peanut-shaped bulges. Although their results seem to support the scenario described above, they only studied two galaxies. A similar study of a sample of thirty galaxies, most of which have a boxy or peanut-shaped bulge, will be presented in Chapter 5. The development of better bar diagnostics and the search for bars in edge-on systems are the keys to a better understanding of the vertical structure of bars. Chapters 3 and 4 of this thesis aim to fulfill the first of those needs; Chapter 5 will address the latter.

In § 3.2, we describe the mass model used in this chapter and in Chapter 4 and detail the methods adopted to calculate and populate the periodic orbits. The orbital properties of the mass model are described in § 3.3. In § 3.4, we describe the PVDs of edge-on spirals and develop kinematical bar diagnostics based on the properties of prototypical barred models with and without inner Lindblad resonances. We also generalise those diagnostics to a large range of models. The limitations of the models for interpreting spectroscopic observations are discussed in § 3.5. We summarise our results and conclude briefly in § 3.6.

3.2 Models

3.2.1 Density Distribution

The mass model used in this chapter and in Chapter 4 is the same as that used by Athanassoula (1992a,b; hereafter A92a, A92b). The results from all of those can therefore be directly compared and are complementary. We briefly review the main characteristics of the mass model here and refer the reader to A92a for a more thorough discussion of its properties.

The mass model has four free parameters which define the density distribution. The bar is represented by a Ferrers spheroid (Ferrers 1877) with density

$$\rho(x,y,z) = \begin{cases} \rho_0(1-g^2)^n & \text{for } g < 1 \\ 0 & \text{for } g \geq 1, \end{cases} \tag{3.1}$$

where $g^2 = x^2/a^2 + (y^2+z^2)/b^2$, a and b are the semi-major and semi-minor axes of the bar ($a > b$), ρ_0 is the bar central density, and (x,y,z) are the coordinates in the frame corotating with the bar. We will consider both homogeneous ($n = 0$) and inhomogeneous models; the latter with $n = 1$. The bar semi-major axis is, as in A92a, fixed at 5 kpc, but, contrary to A92a, the major axis of the bar is along the x-axis. We have thus so far introduced two free parameters: the bar axial ratio a/b (which fixes b) and the quadrupole moment of the bar Q_m (which fixes ρ_0). A92a showed how the central density, axial ratio, quadrupole moment, and mass of the bar are related. The pattern speed of the bar (Ω_p), or equivalently the distance to the Lagrange points L_1 and L_2 (r_L), constitutes a third free parameter.

The bar model described has often been used in the past and is well studied both in the context of orbital studies (e.g. Athanassoula et al. 1983; Papayannopoulos & Petrou 1983; Teuben & Sanders 1985) and of hydrodynamical simulations (e.g. Sanders & Tubbs 1980; Schwarz 1985). The main deficiency of this density distribution is that the shape and axial ratio of the bar are independent of radius.

The density distribution we use also has two axisymmetric components which, when combined together, produce a rotation curve rising relatively rapidly in the inner parts and flat in the outer parts. The first component is a Kuzmin/Toomre disk of surface density

$$\mu(r) = \frac{V_0^2}{2\pi G r_0}(1 + r^2/r_0^2)^{-3/2} \tag{3.2}$$

(Kuzmin 1956; Toomre 1963), where V_0 and r_0 are fixed to yield a maximum disk circular velocity of 164.2 km s^{-1} at 20 kpc. The second axisymmetric component is a central bulge-like spherical density distribution given by

$$\rho(R) = \rho_b(1 + R^2/R_b^2)^{-3/2}, \tag{3.3}$$

where ρ_b is the bulge central density and R_b its scalelength. The fourth free parameter of the mass model is the central concentration, $\rho_c = \rho_0 + \rho_b$ (which fixes ρ_b). The bulge scalelength is determined by imposing a fixed total mass within 10 kpc.

The models are therefore parametrised by an index n ($n = 0$ or 1) and by four free parameters: the bar axial ratio a/b, the quadrupole moment of the bar Q_m, the Lagrangian radius r_L, and the central concentration ρ_c. It should be noted that while the quadrupole moment of the bar affects all Fourier components of the potential equally, this is not the case for the bar axial ratio. The bar pattern speed and the central concentration mainly affect the existence and position of the resonances. The models considered are those of A92a (see her Table 1). We will also use her units: 10^6 $M_\odot$ for masses, kpc for lengths, and km s^{-1} for velocities. Based on a comparison with an observational sample (rotation curves, resonances positions, and Fourier components), A92a showed that these models are a fair representation of early type barred spiral galaxies.

3.2.2 Periodic Orbit Calculations

The periodic orbits allowed by a model are found using the shooting method. Through this chapter, we will only consider orbits in the plane of the disk ($z = 0$). For a given position along the y-axis ($x = 0$) and an initial velocity parallel to the x-axis ($\dot{y} = 0$), we follow a trial orbit for half a revolution in the reference frame of the bar. Other trial orbits with the same initial position but slightly different initial velocities allow iterative convergence to an orbit which "closes" after half a revolution. The orbits are integrated using a fourth-order Runge-Kutta method and the Newton-Raphson method is used to converge to the right initial velocity (Press et al. 1986). By then moving the initial position along the y-axis, it is possible to delineate a family of periodic orbits. Here, we use a constant increment along the y-axis ($\Delta y = 0.01$ kpc for all families). All periodic orbits found in this way are symmetric with respect to the minor axis of the bar. It should be noted that it is possible to have more than one periodic orbit at a given position along the y-axis (each one with a different initial velocity $\dot{x}$).

In the limit of negligible pressure, gas streamlines coincide with periodic orbits. However, contrary to periodic orbits, gas streamlines can not intersect. Thus, because we are mainly interested in studying the gaseous dynamics of barred spiral galaxies, we are not interested in periodic orbits that self-intersect or possess loops. We have therefore searched and identified only direct singly-periodic non-self-intersecting orbits, which best represent the gas flow. This constraint limits the extent of the periodic orbit families we study.

Periodic orbits can be regarded as galactic building blocks, but it is non-trivial to determine how best to use them to represent the gas distribution in a real galaxy. For stellar systems, Schwarzschild (1979) proposed a method where a linear combination (with non-negative weights) of orbits is used to reproduce the original mass distribution (yielding a self-consistent model). Here, we simply consider all the periodic orbits from certain families to be populated equally. Whenever we plot orbits, we plot an equal number of timesteps (an equal number of "points") for all orbits, independent of the period. Since we use a constant increment along the y-axis between the orbits of a given family, the resulting surface density along that axis is inversely proportional to the distance from the center (this would be true everywhere if the orbits were similar). One shortcoming of this method is that, although we have only selected individual periodic orbits which do not self-intersect and do not possess loops, orbits from a given family or from different families of periodic orbits can intersect. Such situations could not occur in the gas.

3.3 Periodic Orbit Families

As we already mentioned, periodic orbits can be thought of as the basic building blocks of the gas distribution in disk galaxies. Although they can not reproduce the properties of the gas flow in detail (e.g. the behaviour of the gas near shocks), they do give a zeroth order representation of the gas distribution and kinematics. It is thus important to understand the properties of the various periodic orbit families present in our models in order to be able to relate them to what is observed in real galaxies. A92a carried out a detailed study of the periodic orbit families located within corotation for our models. In this chapter, we will extend her study to the outer parts of the models (outside corotation) and will draw heavily on her conclusions to explain the behaviour observed in the inner parts. For a more general description of the orbital structure and the dynamics of barred spiral galaxies, we refer the reader to the excellent reviews by Contopoulos & Grosbøl (1989) and Sellwood & Wilkinson (1993).

In this section, we will describe the main properties of the basic families of periodic orbits present in the models. We will focus on two inhomogeneous bar models which are prototypes of models with and without inner Lindblad resonances (ILRs). They are, respectively: model 001 ($a/b = 2.5$, $Q_m = 4.5 \times 10^4$, $r_L = 6.0$, $\rho_c = 2.4 \times 10^4$) and model 086 ($a/b = 5.0$, $Q_m = 4.5 \times 10^4$, $r_L = 6.0$, $\rho_c = 2.4 \times 10^4$). Using the results of A92a, it is easy to extend the conclusions drawn from models 001 and 086 to most other models.

Figure 3.1 shows the characteristic diagrams of models 001 and 086. For all the periodic orbits calculated, they show the position where the orbit intersects the y-axis versus the Jacobi integral of the orbit ($E_J = E - \vec{\Omega}_p \cdot \vec{J}$). The Jacobi integral represents the energy in the rotating frame of the bar, and is the only combination of the energy and angular momentum which is conserved (neither being conserved separately in a rotating non-axisymmetric potential). All the major periodic orbit families are present. More exist, especially higher order resonance families near corotation, but they are probably unimportant for understanding the gas flow. Figure 3 of A92a shows examples of periodic orbits from the main families in model 001 (see Sellwood & Wilkinson 1993 for families outside corotation, although they use a slightly different potential). The most important families inside corotation

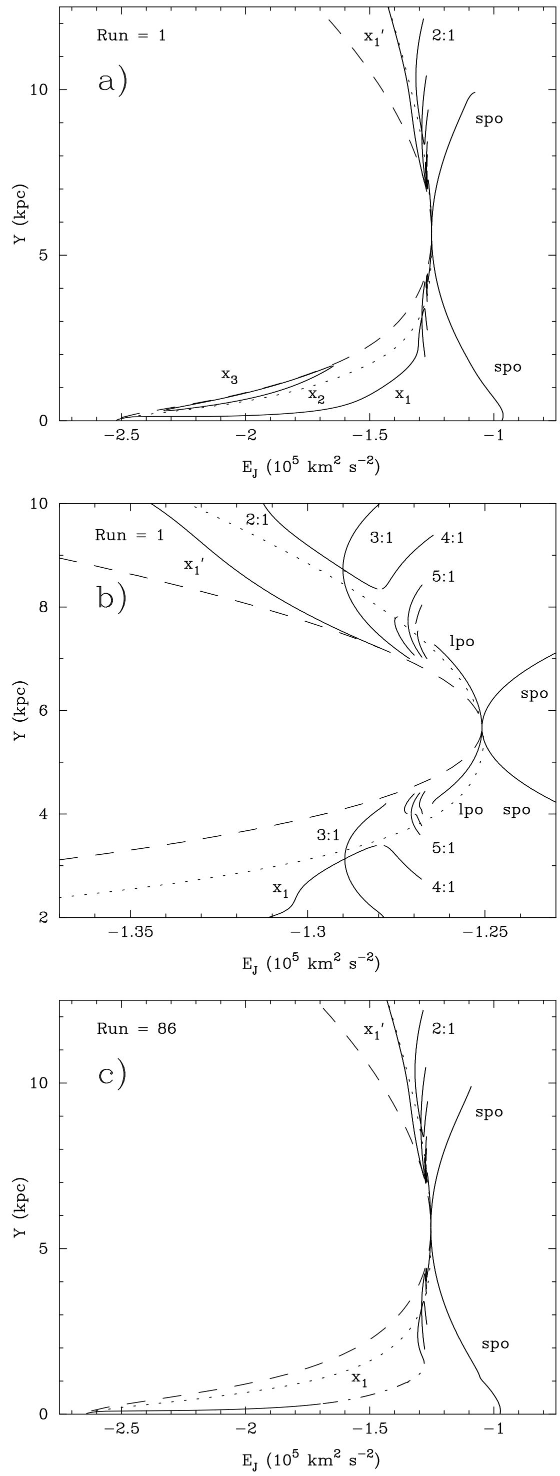

Figure 3.1: (a) Characteristic diagram of model 001. Each point represents a periodic orbit. The solid curves trace the extent of the various periodic orbit families, some of which are identified. The zero-velocity curve (ZVC) which no orbit can cross is plotted with a dashed line. The dotted line represents circular orbits in the azimuthally averaged mass distribution. (b) is simply an enlargement of (a). (c) is the same as (a) but for model 086. The section of the x_1 family plotted with a dot-dashed line represents orbits with loops.

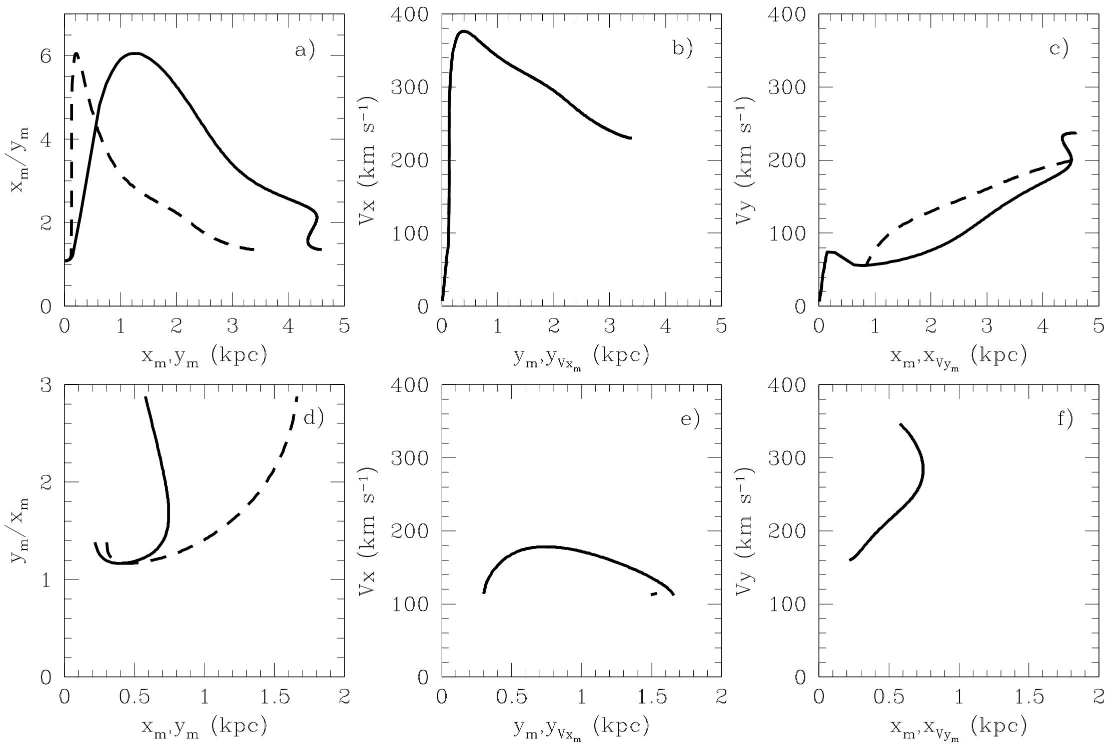

Figure 3.2: Basic properties of the x_1 and x_2 periodic orbits in model 001. (a) shows the axial ratio of the x_1 orbits as a function of their semi-major (full line) and semi-minor (dashed line) axes. (b) shows the velocity of the x_1 orbits as they cross the minor axis of the bar (full line), as well as the maximum velocity along the x-axis they reach at any point (dashed line). (c) shows the velocity of the x_1 orbits as they cross the major axis of the bar (full line), as well as the maximum velocity along the y-axis they reach at any point (dashed line). (d)–(f) are the same as (a)–(c) but for the x_2 orbits. Note that both curves are superposed in some plots.

are the x_1 and x_2. The x_1 orbits are elongated parallel to the bar and are generally thought to support it in self-consistent systems (see, e.g., Contopoulos 1980). The x_2 (and x_3) orbits are elongated perpendicular to the bar and only occur inside the ILRs. Some properties of the x_1 and x_2 periodic orbits which will be useful in the next sections are summarised in Figure 3.2. We do not consider the retrograde x_4 family here. The inner 4:1 family (four radial oscillations during one revolution) may be important for the structure of rectangular bars. Outside corotation, the dominant periodic orbit families are the x_1' and outer 2:1, corresponding to the "x_i" families inside corotation. The x_1' orbits are elongated parallel to the bar and located outside the outer Lindblad resonance (OLR). The outer 2:1 orbits are elongated perpendicular the bar and located between corotation and the OLR. The short period orbits (SPO) and long period orbits (LPO) are located around the (stable) Lagrange points L_4 and L_5 on the minor axis of the bar.

Figure 3.3 shows the main precession frequencies of models 001 and 086, obtained by azimuthally averaging the mass distribution. The major resonances are easily identified: ILRs ($\Omega_p = \Omega - \kappa/2$), inner ultra-harmonic resonance (IUHR; $\Omega_p = \Omega - \kappa/4$), corotation ($\Omega_p = \Omega$), and OLR ($\Omega_p = \Omega + \kappa/2$). Although the behaviour of the 2:1 periodic orbit families agrees with linear perturbation theory predictions outside corotation, this is not case inside corotation. In particular, despite the presence of ILRs in model 086, no x_2 orbit exists. The presence of ILRs is not enough to guarantee the existence of the x_2 family. Contopoulos & Papayannopoulos (1980) showed that the x_2 family disappears for strong bars. For this mass model, A92a showed that the x_2 orbits are absent for large bar axial ratios a/b, large bar quadrupole moments Q_m, small Lagrangian radii r_L, and for low central concentrations ρ_c (see Figs. 6 and 7 of A92a). It is thus necessary to extend the classical definition of an ILR to the strong bar case. van Albada & Sanders (1982) and A92a proposed that the existence of ILRs could be tied with the existence of the x_2 periodic orbit family and the position of the ILRs assimilated with the minimum and maximum of the x_2 characteristic curve in the characteristic diagram (of course, there might be only one ILR). We will use this definition of the existence and position of ILRs in this chapter, which explains why, despite having two ILRs in the classical sense, model 086 is considered a "no-ILRs" model. Similarly, we will assimilate the position of the IUHR with the maximum of the x_1 characteristic curve before the 4:1 gap in the characteristic diagram (A92a).

3.4 Bar Diagnostics

3.4.1 Detecting Edge-On Bars

Because of the inadequacies of a morphological identification of bars in edge-on spiral galaxies, we aim in this chapter to develop kinematical bar diagnostics, much in the spirit of Kuijken & Merrifield (1995) and Merrifield (1996). Our basic tool to identify bars in edge-on disk galaxies will be PVDs. We obtain those by calculating the projected density of material in our edge-on barred disk models as a function of line-of-sight velocity and projected position along the major axis (for various lines-of-sight). These can then be directly compared with long-slit spectroscopic observations of edge-on spiral galaxies (with the slit positioned along the major axis) or with other equivalent data set. The goal is to identify features in the PVDs which can be unmistakably associated with the presence of a bar. We discuss such features in the next sections.

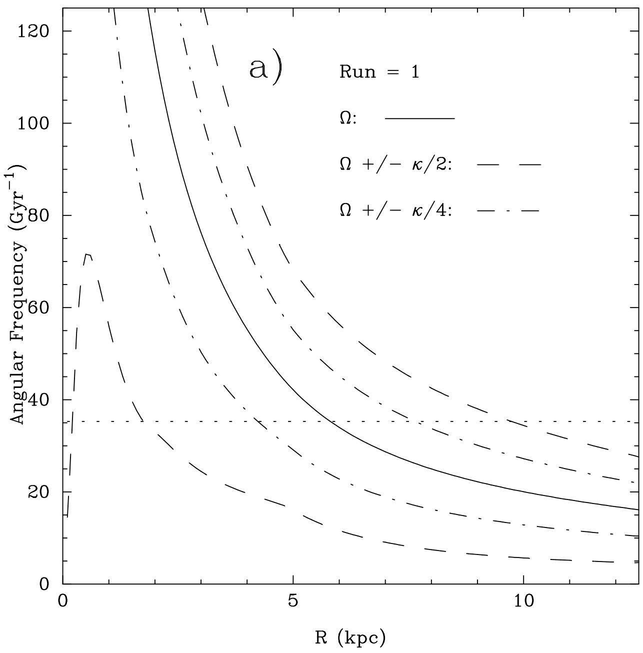

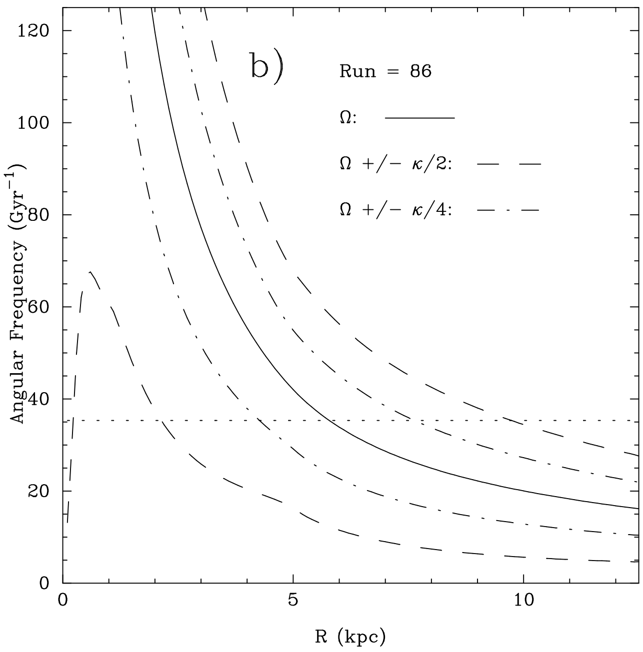

Figure 3.3: (a) Lindblad precession frequencies in the azimuthally averaged mass distribution of model 001. The various frequencies are identified on the plot. The dotted curve shows the pattern speed of the bar Ω_p in the model. (b) is the same as (a) but for model 086.

3.4.2 Model 001 (ILRs)

Figures 3.4, 3.5, and 3.6 show PVDs for, respectively, the x_1, x_2, and outer 2:1 periodic orbit families of model 001, which has ILRs (or, equivalently, has an x_2 family of periodic orbits). Each figure presents the face-on appearance of the entire family of orbits (with orbits equally spaced along the y-axis and the extent of the family limited by gaps in the characteristic curve or the appearance of loops in the orbits) and PVDs obtained using an edge-on projection and various viewing angles with respect to the bar. The viewing angle ψ is defined to be $0°$ when the bar is seen end-on and $90°$ when the bar is seen side-on.

The upper left panel of Figure 3.4 shows that, because of the high curvature of the x_1 orbits on the major axis of the bar (A92a) and the crowding of orbits at its ends, overdensities of material are created which are analogous to those caused by shocks in hydrodynamical simulations (see Sanders, Teuben, & van Albada 1983; Sanders & Tubbs 1980; A92b). As expected, very high radial velocities are present in the PVDs when the bar is seen end-on, because of streaming up and down the bar. Conversely, the velocities are low when the bar is seen side-on, as the movement is mostly perpendicular to the line-of-sight. In the next few paragraphs, we will analyse this effect in more detail, in order to understand the variation of the shape of the signature of the orbits in the PVDs as a function of the viewing angle.

In general, the trace in a PVD of a two-dimensional elongated orbit viewed edge-on can be thought of as a parallelogram. For the sake of simplicity, we will consider here an orbit which is symmetric about two perpendicular axes and which is centered at their origin, like the x_1 and x_2 orbits. If the orbit is seen exactly along one of its symmetry axes, then its trace in a PVD will be a line, both near and far sides of the orbit yielding the same radial velocity at a given projected distance from the center. In addition, the observed radial velocity will switch from positive to negative values at the center (the radial velocity is null at that point). However, for any other viewing angles, the trace of the orbit in a PVD will be strongly parallelogram-shaped, populating the "forbidden" quadrants (top-right and bottom-left quadrants of the PVDs considered here). This shape is due to the fact that, when the line-of-sight is not parallel to one of the axes of symmetry of the orbit, the near and far sides of the orbit yield different radial velocities for a given projected distance from the center, and the position at which the observed radial velocity switches from positive to negative values is not the center, but rather is displaced slightly away from it. One only needs to look at the radial component of the velocity along an elongated orbit to see that. At that position, by definition, the tangent to the orbit is perpendicular to the line-of-sight. Generally, the highest tangential velocity occurs on the minor axis of the orbit and is parallel to its major axis. The opposite is also generally true (but not

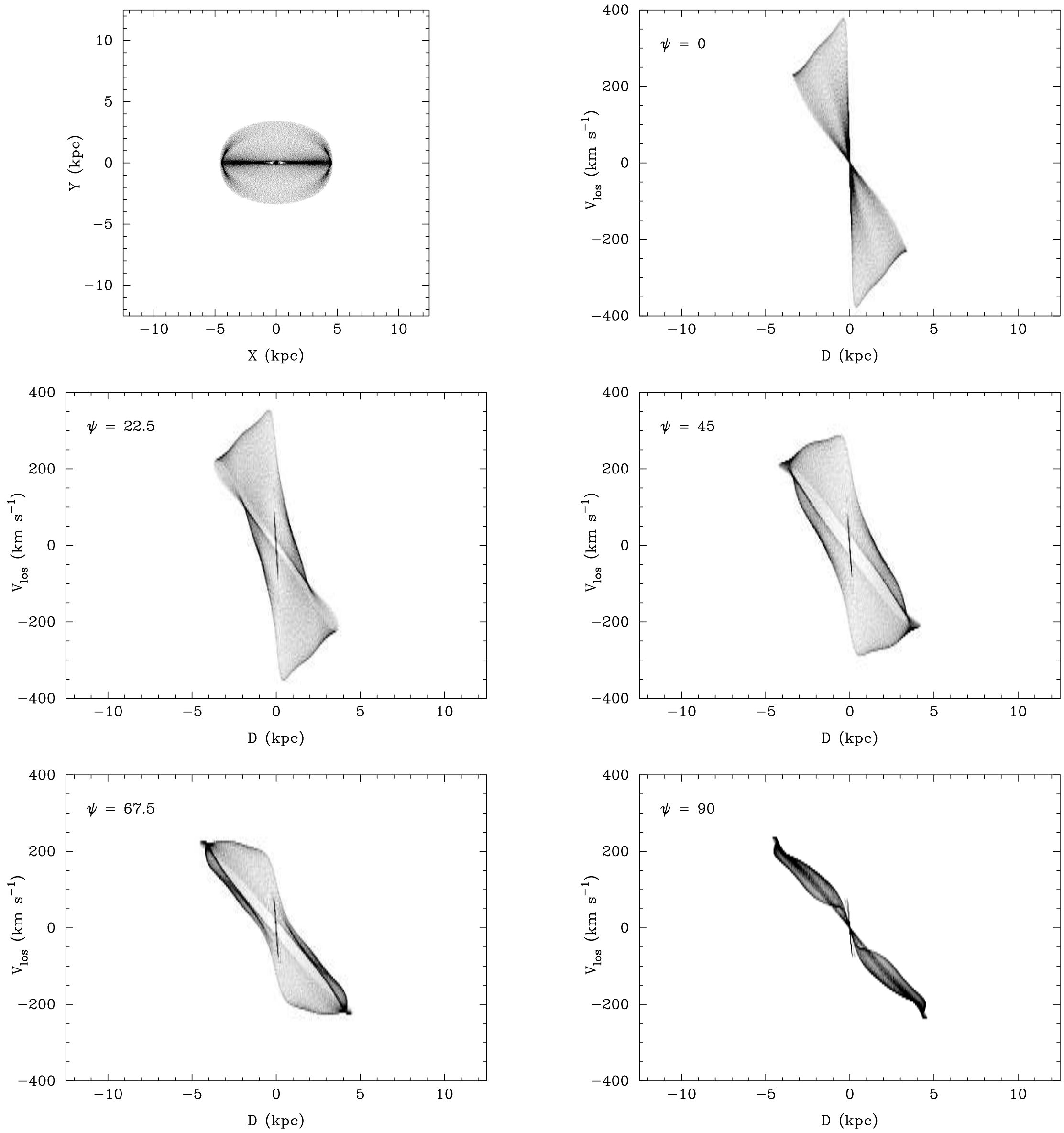

Figure 3.4: Surface density and position-velocity diagrams of the x_1 orbits in model 001. The upper-left plot shows the face-on appearance (surface density) of the orbits, as selected in the text (§ 3.2.2). The bar is horizontal, has a semi-major axis length of 5 kpc, and is rotating clockwise. The other plots show position-velocity diagrams (projected density of material as a function of line-of-sight velocity and projected position along the major axis) of the orbits when the model is viewed edge-on. The angle between the line-of-sight and the bar is indicated in the top-left corner of each diagram, a viewing angle of $\psi = 0°$ indicating that the bar is seen end-on (line-of-sight parallel to the bar) and a viewing angle of $\psi = 90°$ indicating that the bar is seen side-on (line-of-sight perpendicular to the bar).

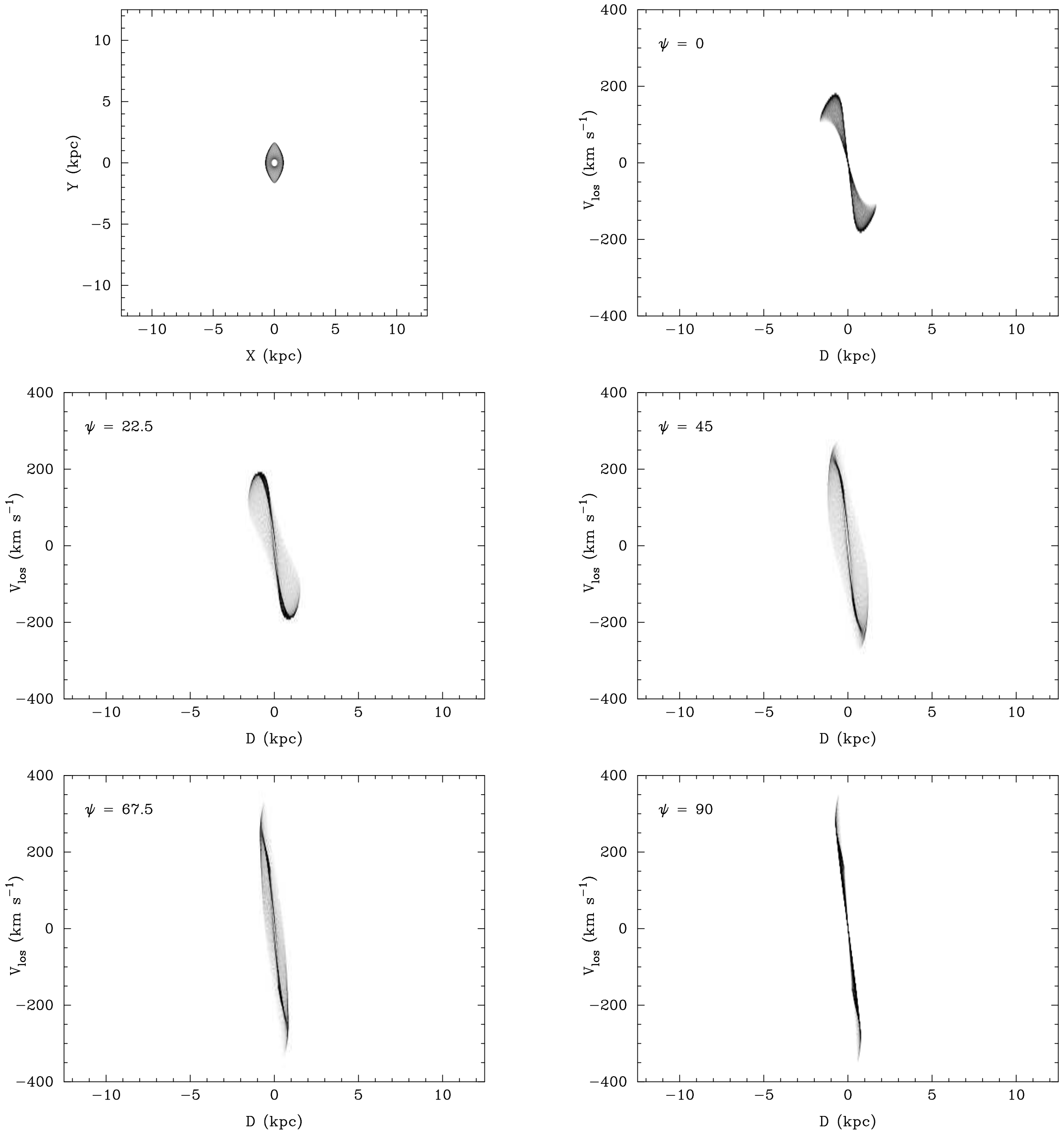

Figure 3.5: Same as Figure 3.4 but for the x_2 family of periodic orbits in model 001.

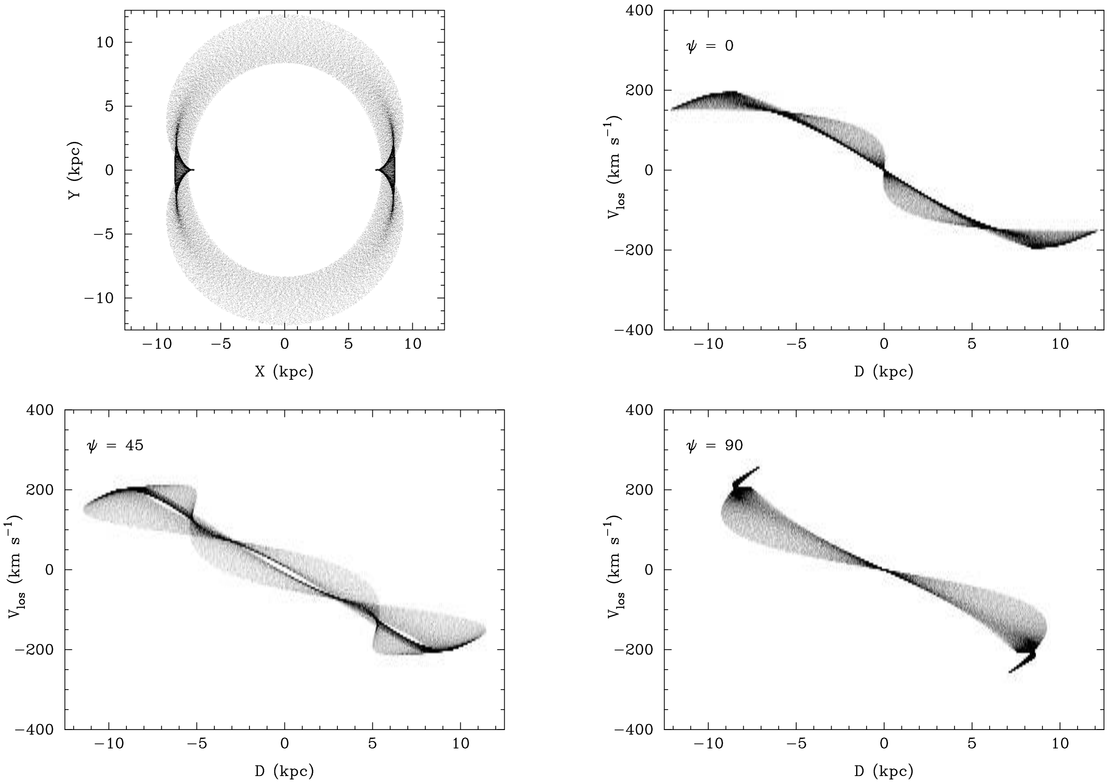

Figure 3.6: Same as Figure 3.4 but for the outer 2:1 family of periodic orbits in model 001. Note that fewer viewing angles are displayed.

always) for the lowest velocity (see, e.g., Fig. 3.2). Therefore, the parallelogram-shaped trace of an elongated orbit in a PVD is narrow but reaches high radial velocities (with respect to the local circular velocity) for viewing angles close (parallel) to its major axis, while it is rather extended and reaches only relatively low radial velocities for viewing angles close to its minor axis. The exact shape of the parallelogram in a PVD depends primarily on the axial ratio of the orbit. For a given azimuthally averaged radius, as the eccentricity of the orbit is increased, the velocity contrast of the orbit (the difference between the highest and lowest tangential velocities) also increases. The viewing angle dependence of the trace of the orbit in a PVD is thus accentuated. At the other end of the eccentricity range, the trace of a circular orbit in a PVD is an inclined straight line passing through the origin and identical for all viewing angles.

The parallelogram-shaped signature of the x_1 orbits of model 001 observed in the PVDs of Figure 3.4 can be understood based on the above principles. The axial ratio of the x_1 orbits generally increases with decreasing radius (except in the very center, see Fig. 3.2a). The inner orbits will thus reach very high radial velocities (compared to the circular velocity) at small projected distances for small viewing angles, while they will reach only low radial velocities at large viewing angles. On the other hand, the projected velocities of the outer orbits will vary little with the viewing angle because they are rounder. They will thus reach radial velocities close to the circular velocity at large projected distances for all viewing angles. Orbits of intermediate radii have intermediate axial ratios and thus intermediate behaviours in the PVDs. As one moves in in radius and in projected distance, the locus of the maxima of the traces of successive orbits in the PVDs will therefore increase rapidly for small viewing angles (see Fig. 3.2b), while it will decrease for large viewing angles (Fig. 3.2c). This is exactly the behaviour observed in the PVDs for the upper part of the envelope of the signature of the x_1 orbits (see Fig. 3.4). For orbits of very small radii, the axial ratio actually decreases rapidly with decreasing radius (the axial ratio reaches a maximum for orbits of minor axis length about 0.2 kpc; Fig. 3.2a). This explains why, for small viewing angles, the envelope of the signature of the x_1 orbits does not increase right to the center, but drops abruptly just before that. The ellipsoidal "holes" in the PVDs at intermediate viewing angles are due to the fact that we stopped the x_1 periodic orbits at the IUHR, not populating the small segments of the x_1 characteristic curve existing past the 4:1 gap in the characteristic diagram (see Fig. 2 of A92a). The holes disappear if we include orbits at larger Jacobi energy E_J (which are also rounder).

In Figure 3.5, the behaviour of the x_2 periodic orbits of model 001 can be contrasted with that of the x_1. As expected, because the x_2 orbits are elongated perpendicular to the bar (see Fig. 3 of A92a), the highest radial velocities are now reached when the bar is seen side-on, and the lowest when the bar is seen end-on. The general parallelogram shape of the PVDs is still present, but its nature is quite different from that of the signature of the x_1 orbits, shown in Figure 3.4. Contrary to the x_1 orbits, the axial ratio of the x_2 orbits generally decreases with decreasing radius (up to about 0.4 kpc, see Fig. 3.2d). The inner orbits have only a short extent and, because they are almost circular, they do not reach high radial velocities. Their projected velocity is close to the circular velocity for all viewing angles. The outer orbits, on the other hand, are highly elongated. They will thus reach only relatively low radial velocities at "large" projected distances for small viewing angles, and high velocities at "large" distances for large viewing angles (they are elongated perpendicular to the bar). The locus of the maxima of the traces of successive orbits of decreasing radius in the PVDs will therefore increase rapidly for small viewing angles (see Fig. 3.2e) and decrease for large viewing angles (Fig. 3.2f). Indeed, this behaviour is observed in the PVDs of Figure 3.5, at least for "large" projected distances. The behaviour at very small radii is dominated by the shape of the circular velocity curve, which rises rapidly with radius.

The observed behaviours of the x_1 and x_2 periodic orbits in the PVDs are qualitatively rather similar. This might be surprising on first thought, as the x_2 orbits behave very differently than the x_1 (see Fig. 3.2), but one could say that the properties of the x_2 orbits are "doubly-inverted" with respect to those of the x_1. The variations of the axial ratio of the x_1 and x_2 orbits with radius are opposite (Fig. 3.2), so the dependence of their signatures on the viewing angle with respect to their major axes will also be opposite. Furthermore, the major axes of the x_1 and x_2 orbits are perpendicular to each other. This "double inversion" leads to the similarity of the signatures in the PVDs. While this is true in a relative manner, it is not true in an absolute manner. Firstly, the envelope of the signature of the x_1 orbits reaches higher radial velocities than that of the x_2 orbits at small viewing angles, and the opposite is observed at large viewing angles. The explanation is simple: for small viewing angles, the radial velocities reached by the x_1 orbits in the *inner parts* are *increased* with respect to the circular velocity (the outer parts are unchanged), while for the x_2 orbits, the radial velocities in the *outer parts* are *decreased* with respect to the circular velocity (the inner parts are unchanged). The opposite is true at large viewing angles. Secondly, in the case of the x_1 orbits, the center of the parallelogram-shaped signature is relatively faint compared to its edges, while for the x_2 orbits, it is the center of the parallelogram which is bright, forming a strong inverted S-shape feature, and the outer parts are relatively faint. The inverted S-shape feature is not due to a single orbit leaving such a trace in the PVDs, but rather to the crowding of the traces of many successive orbits, which explains why it is so bright (an effect comparable to the spiral arms created by rotating slightly similar ellipses of increasing radii; Kalnajs 1973). Furthermore, because the axial ratio of the x_2 orbits increases with radius (outside 0.4 kpc), the trace of the largest orbit in the PVDs is not only the most extended but also is the one with the widest parallelogram shape. It therefore encompasses the traces of all the other orbits and defines largely by itself the envelope of the signature of the x_2 orbits, which is then very faint. The small "holes" present in the center of the PVDs of the x_2 periodic orbits at intermediate viewing angles are due to the fact that, although the elongation of the x_2 orbits generally decreases inward, the x_2 family does not extend up to the center (see Fig. 3.1).

Figure 3.6 illustrates the signature of the outer 2:1 orbits of model 001 in the PVDs. Because the orbits are almost circular, the upper part of the envelope reaches radial velocities close to the circular velocity at large projected distances, independent of the viewing angle. The features seen in the signature of the outer 2:1 orbits are largely due to the "dimples" in the orbits on the major axis of the bar (see Fig. 11 in Sellwood & Wilkinson 1993). As should be expected, the PVDs of the x_1' orbits (not shown) are similar to those of the outer 2:1 orbits if the viewing angles are reversed (e.g. $67.5° \rightarrow 22.5°$), the major axes of the orbits being at right angles. Both families yield a slowly-rising almost solid-body signature in the PVDs for all viewing angles.

Bars in early-type spiral galaxies and in N-body simulations tend to have a rectangular shape rather than an ellipsoidal shape (see, e.g., Sparke & Sellwood

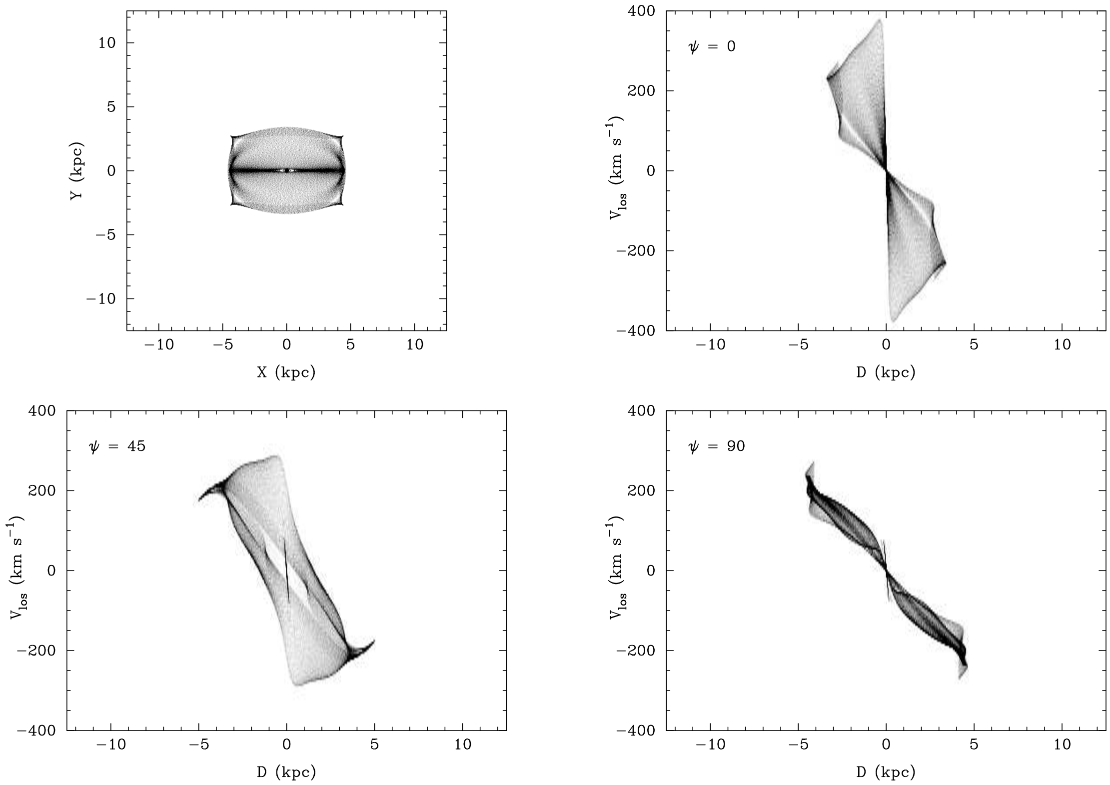

Figure 3.7: Same as Figure 3.4 but for the x_1 and inner 4:1 families of periodic orbits in model 001. Note that fewer viewing angles are displayed. Only the section of the inner 4:1 family lying outside the characteristic curve of the x_1 orbits in the characteristic diagram has been considered.

1987; Athanassoula et al. 1990). Interestingly, the maximum boxiness generally occurs just before the end of the bar (Athanassoula et al. 1990), where the x_1 orbits are slightly boxy and where the rectangular-shaped inner 4:1 orbits are found (see Fig. 3 of A92a). It is thus tempting to associate the branch of the inner 4:1 family of periodic orbits lying outside the characteristic curve of the x_1 orbits in the characteristic diagram (see Fig. 3.1) with the rectangular shape of bars. The 4:1 gap in model 001 is of type 2 (see Contopoulos 1988; A92a), so the lower branch of the 4:1 characteristic is stable and the proposed association makes sense, but this is not necessarily the case in real galaxies. In fact, early-type galaxies seem to have 4:1 gaps of type 1 (Athanassoula 1996). Figure 3.7 shows the surface density and PVDs for both the x_1 family of periodic orbits and the lower branch of the inner 4:1 family in model 001. It shows that indeed the inner 4:1 orbits can create a very rectangular surface density distribution when combined with the x_1 orbits. Although the signature of the inner 4:1 orbits in the PVDs is very peculiar and easily identifiable when taken alone, it is superposed on the signature of the x_1 orbits for most viewing angles and it is hard to disentangle the two families. However, when the bar and the inner 4:1 orbits are seen either end-on or side-on, the inner 4:1 orbits leave a signature in the PVDs distinct from that of the x_1 orbits. The lower limit of the combined envelope of the signatures of the x_1 and inner 4:1 orbits is straight and only slightly inclined at small projected distances, until it does a sharp bend at approximately the position of the IUHR (at a slightly smaller radius when $\psi = 0°$ and slightly larger radius when $\psi = 90°$, following the definition of the IUHR adopted in § 3.3). It then rises vertically until it joins with the upper limit of the envelope. This is easily understandable considering the morphology of the inner 4:1 orbits. The projected edges of the density distribution are sharpest at those viewing angles and the lines-of-sight are parallel to the approximately straight segments of the orbits (see Fig. 3.7).

The advantage of the periodic orbits approach is that various orbital components of a galaxy can be combined together in a multitude of ways. A superposition of the x_1, x_2, and outer 2:1 families of periodic orbits should give a reasonable representation of a prototypical barred galaxy with ILRs. Indeed, in the inner parts, only three direct families exist: the x_1, x_2, and x_3 (see Fig. 3.1). The x_1 orbits, parallel to the bar, are certainly present and, because the x_3 orbits are unstable (e.g. Sellwood & Wilkinson 1993), the x_2 orbits will dominate over the x_3 if orbits perpendicular to the bar are present. In the outer parts, we find the x_1' and outer 2:1 periodic orbit families. The shapes of these orbits are almost identical to those of the two subclasses of outer rings observed in barred spiral galaxies (Buta & Crocker 1991): R_1' outer rings for the outer 2:1 orbits and R_2' for the x_1' orbits. The R_1' class is dominant (Buta 1986), which explains why we considered the outer 2:1 family of periodic orbits. However, as we mentioned, the signature of the x_1' orbits in the PVDs is very similar to that of the outer 2:1 orbits (almost identical if the viewing angles are reversed) and using one or the other does not affect our conclusions or the nature of the bar diagnostics in the PVDs. Both families act as a slowly rising almost solid-body component.

Figure 3.8 shows the surface density and PVDs obtained by superposing the x_1, x_2, LPO, and outer 2:1 families of periodic orbits in model 001. The surface density of the x_1, x_2, and outer 2:1 families is qualitatively similar to what is observed for barred galaxies with an outer ring (at least for the gaseous component). More interesting is the amount of structure present in the PVDs, especially in the inner parts of the model where the effects of the bar are strongest. We find back the signatures of the x_1 and x_2 orbits already discussed above, as well as the features which allow us to determine the viewing angle with respect to the major axis of the bar. The large gap between the signatures of the x_1 and outer 2:1 families of periodic orbits in the PVDs (partially filled in Fig. 3.8) is due to our reconstitution of the density distribution of a prototypical barred galaxy, which also has a gap between the distributions of the x_1 and outer 2:1 families. The only way to make this gap disappear is to populate periodic orbit families close to corotation, but this is not obvious using our periodic orbits approach. Beyond the 4:1 gap in the characteristic diagram, there are higher order n:1 families,

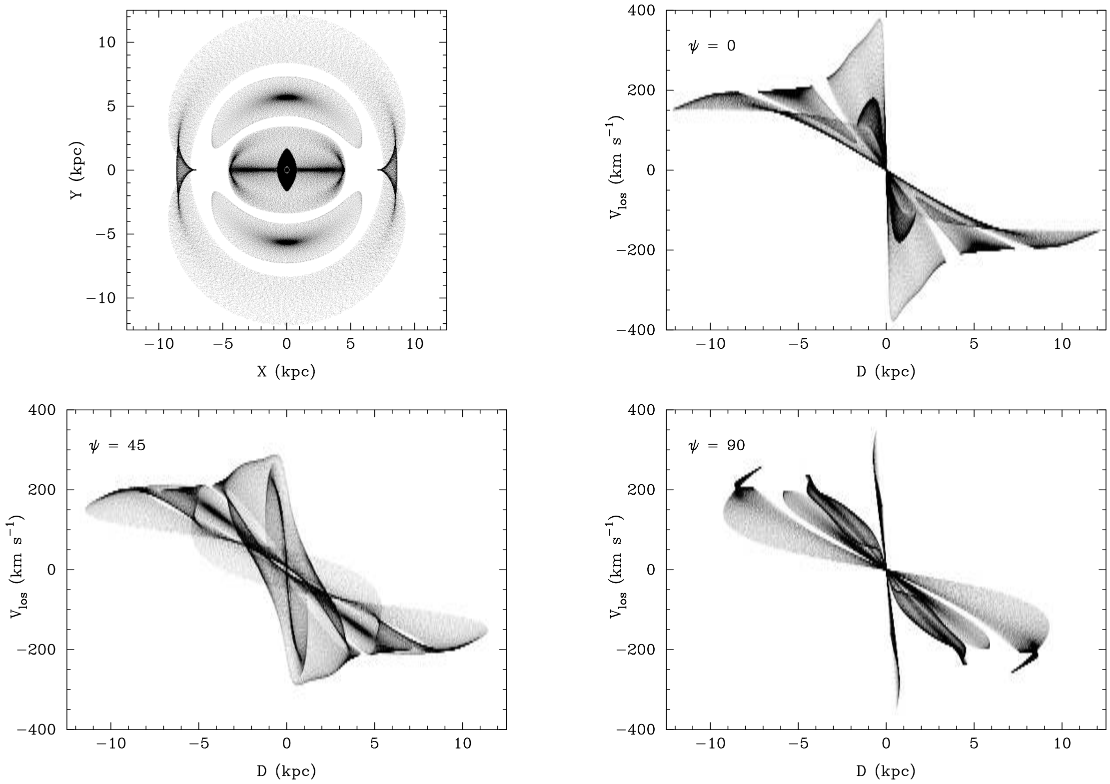

Figure 3.8: Same as Figure 3.4 but for the x_1, x_2, LPO, and outer 2:1 families of periodic orbits in model 001. Note that fewer viewing angles are displayed.

and, between consecutive 2n:1 gaps, short segments of what can still be called x_1 orbits (see Fig. 3.1 and Fig. 2 in A92a). However, as can be seen from the figures of A92b, the gas streamlines continue to be ellipsoidal and elongated along the bar past the IUHR, the extent of this region being very model dependent. Loosely speaking, one could say that, although the gas does not follow precisely the higher order resonance families, it follows their general form. Yet, further out the gas circulates around each of the two stable Lagrange points L_4 and L_5, the streamlines now being associated with the LPO periodic orbits (see Fig. 11 in Sellwood & Wilkinson 1993). The latter are easy to add in our description and have been included in Figure 3.8. Their signature in the PVDs is very similar to that of circular orbits. As expected, because of their location, the signature of the LPO orbits partially fills the gap between the signature of the x_1 orbits and that of the outer 2:1 orbits. The gap is significantly reduced, but many smaller gaps are still present, due to the non-homogeneous distribution of the orbits of the various families. Such gaps could not occur in an axisymmetric spiral galaxy.

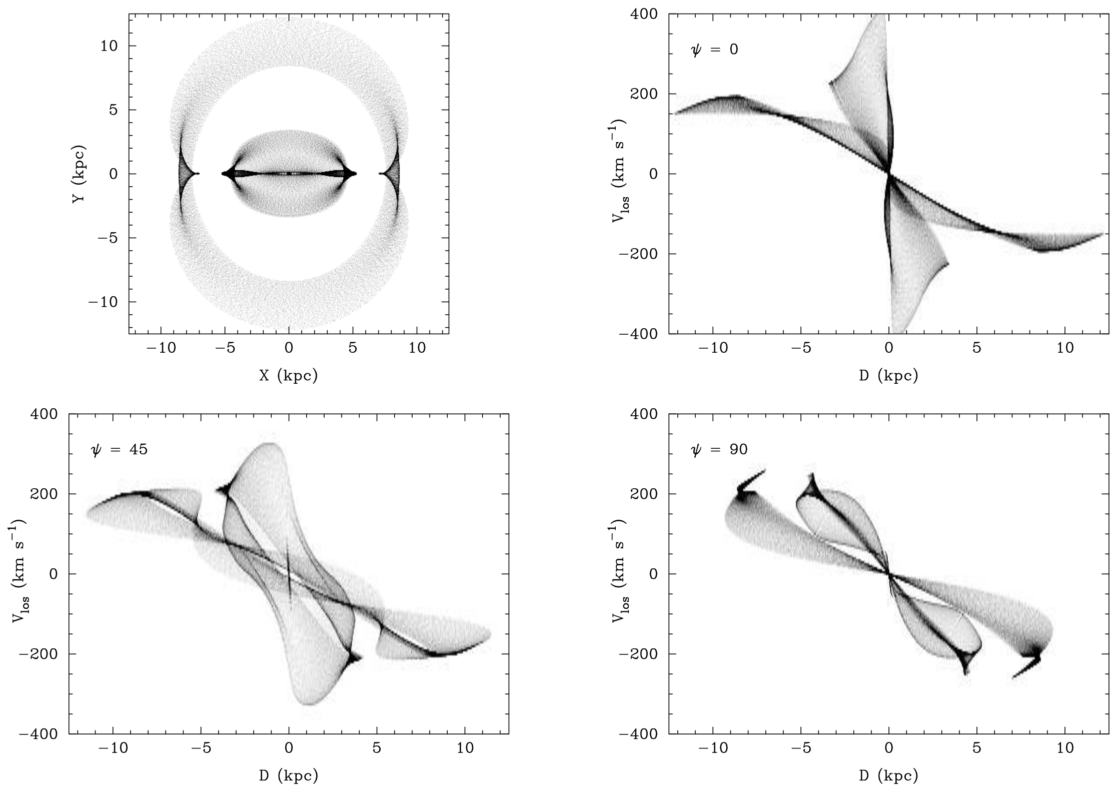

Figure 3.9: Same as Figure 3.4 but for the x_1 and outer 2:1 families of periodic orbits in model 086. Note that fewer viewing angles are displayed.

3.4.3 Model 086 (no-ILRs)

Despite the presence of ILRs in the classical sense (see Fig. 3.3), we consider model 086 a "no-ILRs" model because it does not have an x_2 family of periodic orbits. Its characteristic diagram is very similar to that of model 001 (see Fig. 3.1), differing only in the inner parts, where the x_2 and x_3 families are absent and the x_1 characteristic curve displays an elbow due to the high axial ratio of the bar (see also Fig. 4 of A92a; Pfenniger 1984). In addition, the x_1 orbits possess loops for a certain range of radii. Here, we exceptionally include those orbits to prevent the appearance of an empty region in the x_1 orbits surface density distribution.

Figure 3.9 shows the surface density and PVDs obtained by superposing the x_1 and outer 2:1 families of periodic orbits in model 086. The surface density distribution is again similar to that observed for the gaseous component of barred spiral galaxies. In the PVDs, as expected, the signature of the outer parts of the model has not changed compared to model 001, the outer 2:1 family of periodic orbits behaving again like a slowly-rising solid-body component (see Fig. 3.6). In the inner parts, the obvious difference with the PVDs of model 001 (Fig. 3.8) is the absence of any x_2 orbit signature (the LPO orbits have been omitted in Fig. 3.9 for clarity). On a qualitative level, the signature of the x_1 orbits has changed only slightly, the envelope still being generally parallelogram-shaped. The main difference with the signature of the x_1 orbits in model 001 is that the envelope of the signature has more curved edges, due to the presence of orbits with loops, and it reaches more extreme radial velocities (compared to the circular velocity), due to the higher axial ratio of the bar yielding more eccentric orbits (see Fig. 10 in A92a). The gap between the signatures of the x_1 and outer 2:1 orbits is again due to the absence of populated orbits near corotation in our model.

3.4.4 Other Models

Now that we understand the general structure of the PVDs produced by models with and without ILRs, we can extend our study to investigate how the bar diagnostics might change when the free parameters of the mass model are varied. To do this, we borrow heavily on the results of A92a, who studied how the orbital structure of the mass model varies within most of the volume of parameter space likely to be occupied by real galaxies. We do not expect the outer parts of the models to vary significantly since the influence of the bar falls off rapidly with radius. The outer families of periodic orbits will always produce slowly-rising almost solid-body signatures in the PVDs. We will thus concentrate on understanding the behaviour of the periodic orbits in the inner parts of the models.

The parallelogram-shaped signatures of the x_1 and x_2 periodic orbits in the PVDs will be mainly affected by the eccentricity and extent of the orbits. The results of A92a concerning the eccentricity of the x_1 orbits can be summarised as follows (see Fig. 10 in A92a): as the axial ratio of the bar a/b is increased, the Lagrangian radius r_L increased, the central concentration ρ_c increased, and/or the quadrupole moment of the bar Q_m decreased, the eccentricity of the x_1 orbits is increased. The counterintuitive behaviour of the eccentricity of the x_1 orbits with Q_m stems from the fact that for Q_m to be increased, the bulge mass and therefore the central density of the model has to be decreased (the total mass within a given radius being fixed), leading to a decrease of the eccentricity of the orbits. The eccentricity of the x_2 orbits behaves in the same way as that of the x_1 orbits, except with respect to the axial ratio of the bar (again, see Fig. 10 in A92a). In that case, the x_2 orbits become less eccentric as the bar axial ratio is increased. Because higher eccentricity means more extreme radial velocities compared to the circular velocity in the PVDs (very high radial velocities when an orbit is seen end-on and very low velocities when an orbit is seen side-on), the envelopes of the signatures of the x_1 and x_2 orbits in the PVDs should be most extreme (in the above sense) for high bar axial ratios (except for the x_2 orbits), high Lagrangian radii, high central densities, and/or low bar quadrupole moments. This was certainly the case for model 086, which has a higher bar axial ratio than model 001 (see Fig.3.4 and 3.9).

A92a showed that the radial extent of the x_1 family of periodic orbits is mainly affected by the pattern speed of the bar and changes very little as the other parameters of the mass model are varied (see Fig. 6 and 7 of A92a). For the x_2 orbits, the major factor affecting their signature in the PVDs will be their existence or non-existence, depending on the model considered. A92a showed that the radial range of the x_2 orbits is reduced when the bar axial ratio a/b and/or bar quadrupole moment Q_m are increased, and when the central density ρ_c and/or Lagrangian radius r_L are decreased (again, see Fig. 6 and 7 of A92a). Furthermore, as exemplified by model 086, the x_2 orbits can be completely absent for high bar axial ratios and/or bar quadrupole moments, and for low central densities and/or Lagrangian radii. The presence and extent of the inverted S-shape signature of the x_2 orbits in the PVDs depends therefore strongly on the parameters of the mass model.

Full sequences of PVDs as each parameter of the mass model is varied will be provided in Chapter 4, using hydrodynamical simulations. We do not present them here using the periodic orbits approach to avoid unnecessary repetition.

3.5 Discussion

The bar diagnostics we have developed in the previous sections are all based on the use of periodic orbit families in the equatorial plane of a barred spiral galaxy mass model. Periodic orbits, however, are only an approximation to the dynamical structure of either the gas or the stars in galaxies and the PVDs presented in the previous sections should only be used as a *guide* when interpreting kinematical data.

The ability of the gaseous component to dissipate energy changes its behaviour from that predicted by the periodic orbits, particularly near shocks, which occur at the transition regions between different orbit families and near periodic orbits with loops. The kinematics of the stars on regular orbits are relatively well approximated by that of the periodic orbits, since the former are trapped around the latter. On the other hand, stars on chaotic orbits give a totally different signature in the PVDs, and the percentage of stars on such orbits may well be non-negligible, particularly in strongly barred galaxies. In addition, when populating the periodic orbit families, we have not attempted to make the models self-consistent. We have only calculated the shape of the signature in the PVDs of each family of periodic orbits of the models, but not the relative weights of the families or the relative weights of the orbits within them. Nevertheless, in order to assess how much our results depend on the method adopted to populate the orbits, we have also produced PVDs for the x_1 and x_2 periodic orbits of model 001 using equal increments of the Jacobi energy between orbits (rather than equal Δy). As expected, the envelope of the signature of the x_1 orbits in the PVDs does not change, but, because of the form of the x_1 characteristic curve (see Fig. 3.1), the central parts are much stronger. Similarly, the signature of the x_2 orbits changes very little.

Independent of those issues, the relative amplitudes of the components of the PVDs will also vary depending on the emission line observed, this simply because the components arise from different parts of the galaxy, where the line might be produced in different ways. For example, increased star formation and/or shocks in some components will lead to different emission line strengths in those components, and the ratios between the components will depend on the line used to measure the kinematics.

When interpreting data based on the PVDs produced here, one should therefore take into account the following effects: 1) the kinematical signature observed might be somewhat different from that calculated here because periodic orbits are only an approximation to the gaseous or stellar dynamics of a galaxy, 2) the relative amplitudes of the components will be different from those calculated here because the building blocks approach used may not represent the relative weights correctly, and 3) the relative amplitudes of the components will be different from those calculated here because the intensity of a line depends not only on the density of the emitting material but also on the production mechanism of the line, which is not considered here. The hydrodynamical simulations reported in Chapter 4 address the first of those problems, although the gas is still not treated self-consistently. Being self-consistent, the N-body simulations reported in Paper III cover both the first and second problems (for stellar systems). However, to remedy the third problem raised above, one would need to consider both stellar evolution and the detailed physical conditions in the gas.

Another effect which might hinder our ability to detect bars in edge-on spiral galaxies is the presence of dust. Because dust in spiral galaxies is mostly confined to a thin layer, it can make disks optically thick at optical wavelengths if they are viewed edge-on. If this is the case, there are two ways around the opacity problem. Firstly, it is possible to select objects which are not perfectly edge-on. The line-of-sight then reaches the central parts of the galaxy, where the bar resides, while still going through a substantial fraction of the disk. However, if the inclination is too large, the bar diagnostics developed here will not work, as they depend on the line-of-sight going through most of the disk. Secondly, it is possible to use observations in a part of the spectrum where even a dusty disk is likely to be optically thin. Long-slit spectroscopy in the near-infrared (e.g. using the Brγ line at K-band) is attractive, but most lines are weak in non-active galaxies and near-infrared spectrographs with sufficient resolution for kinematical work are still uncommon. A better option is to use H I line-imaging with a radio synthesis telescope. Even very dusty edge-on spiral galaxies are probably optically thin at 21 cm. In addition, it is possible to use a higher spectral resolution than available with most optical long-slit spectrographs. However, because of limited sensitivity and spatial resolution, radio synthesis observations are useful only for large H I-rich galaxies. Using a large sample of galaxies, we will address in more detail in Chapter 5 the question of dust extinction when identifying bars in edge-on spiral galaxies.

3.6 Summary and Conclusions

Our main goal in this chapter was to develop kinematical bar diagnostics for edge-on spiral galaxies. Considering a well-studied mass model including a Ferrers bar, we identified the major periodic orbit families and briefly reviewed the orbital structure in the equatorial plane of barred spiral galaxies. We considered only orbits which are direct, singly-periodic, and non-self-intersecting. Using a simple method to populate the orbits, we then used the families of periodic orbits as building blocks to model the structure of real galaxies.

We constructed position-velocity diagrams (PVDs) of the models using an edge-on projection and various viewing angles with respect to the bar. We considered mainly two models which are prototypes of models with and without inner Lindblad resonances. The PVDs obtained show a complex structure which would not occur in an axisymmetric galaxy (see Fig. 3.8 and 3.9). The *global* appearance of the PVDs can therefore be used as a reliable bar diagnostic in edge-on disks. Specifically, the presence of gaps between the signatures of the various periodic orbit families in the PVDs follows directly from the non-homogeneous distribution of the orbits in a barred galaxy. The x_1 orbits lead to a parallelogram-shaped feature in the PVDs which reaches very high radial velocities with respect to the outer parts of the model when the bar is seen end-on and rather low velocities when the bar is seen side-on. This feature occupies all four quadrants of the PVDs, i.e. including the two forbidden quadrants. This signature would dominate the structure of the PVD produced by the stellar component of a barred spiral galaxy, and can be used as an indicator of the viewing angle with respect to the bar in an edge-on disk. When present, x_2 orbits can also be used reliably as a bar diagnostic and behave similarly to the x_1 orbits in the PVDs. However, the highest velocities are now reached when the bar is seen side-on and the signature is spatially much more compact. The signature of the x_2 orbits would dominate the structure of the PVD produced by the gaseous component of a barred spiral galaxy.

The mass model we adopted had four free parameters, allowing to reproduce the range of properties observed in real galaxies. Using the results of A92a, we analysed how the structures present in the PVDs vary when the parameters of the mass model are changed. We predicted that the signatures of the x_1 and x_2 periodic orbits should be more extreme for high bar axial ratios (except for the x_2 orbits), high Lagrangian radii, high central densities, and/or for low bar quadrupole moments. In addition, the extent of the x_2 family is reduced and the orbits can completely disappear when the bar axial ratio and/or bar quadrupole moment are increased and when the Lagrangian radius and/or central density are decreased. The shape and presence of the signatures of the x_1 and x_2 families of periodic orbits in a PVD can therefore provide strong constraints on the mass distribution of an observed galaxy.

We briefly discussed the application of the models to the interpretation of real data. The major limitations of the models are the approximation of the disk kinematics by that of periodic orbits, the treatment of the orbits as "test particles", and the ignorance of the production mechanism of the line observed. The understanding of the traces of individual periodic orbits in the PVDs, and of the signatures of the periodic orbit families, will prove very useful in Chapter 4 and in Paper III. In those, using hydrodynamical and N-body simulations, we will develop bar diagnostics similar to the ones discussed here and addressing some of the above limitations.

References

Athanassoula, E. 1992a, MNRAS, 259, 328 (A92a)

———. 1992b, MNRAS, 259, 345 (A92b)

———. 1996, in Spiral Galaxies in the Near-IR, ed. D. Minniti, and H.-W. Rix (Springer: Berlin), 147

Athanassoula, E., Bienayme, O., Martinet, L., & Pfenniger, D. 1983, A&A, 127, 349

Athanassoula, E., & Bureau, M. 1999, in preparation. (Paper III)

Athanassoula, E., Morin, S., Wozniak, H., Puy, D., Pierce, M. J., Lombard, J., & Bosma, A. 1990, MNRAS, 245, 130

Beaulieu, S. F. 1996, Ph. D. Thesis, The Australian National University

Binney, J., Gerhard, O. E., Stark, A. A., Bally, J., & Uchida K. I. 1991, MNRAS, 252, 210

Blitz, L., & Spergel, D. N. 1991, ApJ, 379, 631

Burstein, D. 1979a, ApJS, 41, 435

———. 1979b, ApJ, 234, 829

Buta, R. 1986, ApJS, 61, 609

Buta, R., & Crocker, D. A. 1991, AJ, 102, 1715

Combes, F., Debbasch, F., Friedli, D., & Pfenniger, D. 1990, A&A, 233, 82

Combes, F., & Sanders, R. H. 1981, A&A, 96, 164

Contopoulos, G. 1980, A&A, 81, 198

———. 1988, A&A, 201, 44

Contopoulos, G., & Grosbøl, P. 1989, A&A Rev., 1, 261

Contopoulos, G., & Papayannopoulos, T. 1980, A&A, 92, 33

de Carvalho, R. R., & da Costa, L. N. 1987, A&A, 171, 66

Ferrers, N. M. 1877, Q.J. Pure Appl. Math., 14, 1

Fux, R. 1997, A&A, 327, 983

———. 1997, Ph. D. Thesis, Université de Genève

Hamabe, M., & Wakamatsu, K. 1989, ApJ, 339, 783

Kalnajs, A. J. 1973, PASA, 2, 174

Kuijken, K., & Merrifield, M. R. 1995, ApJ, 443, L13

Kuzmin, G. 1956, AZh, 33, 27

Merrifield, M. R. 1996, in Barred Galaxies, ed. R. Buta, D. A. Crocker, and B. G. Elmegreen (ASP: San Francisco), 179

Mulder, W. A., & Liem, B. T. 1986, A&A, 157, 148

Papayannopoulos, T., & Petrou, M. 1983, A&A, 119, 21

Peters, W. L. 1975, ApJ, 195, 617

Pfenniger, D. 1984, A&A, 134, 373

Press, W. H., Flannery, B. P., Teukolsky, S. A., & Vetterling, W. T. 1986, Numerical Recipes (Cambridge: Cambridge University Press)

Raha, N., Sellwood, J. A., James, R. A., & Kahn, F. D. 1991, Nature, 352, 411

Sandage, A. 1961, The Hubble Atlas of Galaxies (Washington: Carnegie Institution)

Sanders, R. H., Teuben, P. J., & van Albada, G. D. 1983, in Internal Kinematics and Dynamics of Galaxies, ed. E. Athanassoula (Reidel: Dordrecht), 221

Sanders, R. H., & Tubbs, A. D. 1980, ApJ, 235, 803

Schwarz, M. P. 1985, MNRAS, 212, 677

Schwarzschild, M. 1979, ApJ, 232, 236

Sellwood, J. A., & Wilkinson, A. 1993, Re. Prog. Phys., 56, 173

Sevenster, M. S., Saha, P., Valls-Gabaud, D., & Fux, R. 1997, MNRAS, submitted.

Sparke, L. S., & Sellwood, J. A. 1987, MNRAS, 225, 653

Teuben, P., & Sanders, R. H. 1985, MNRAS, 201, 303

Toomre, A. 1963, ApJ, 138, 385

Tsikoudi, V. 1980, ApJS, 43, 365

van Albada, T. S., & Sanders, R. H. 1982, MNRAS, 201, 303

Wada, K., Taniguchi, Y., Habe, A., & Hasegawa, T. 1994, ApJ, 437, L123

Wakamatsu, K., & Hamabe, M. 1984, ApJS, 56, 283

Weiland, J. L., et al. 1994, ApJ, 425, L81

Weiner, B. J., & Sellwood, J. A. 1995, BAAS, 186, 884

Wozniak, H. 1994, A&A, 286, L5

Chapter 4

Bar Diagnostics in Edge-On Spiral Galaxies. II. Hydrodynamical Simulations

Abstract

We develop diagnostics based on the gas kinematics to identify the presence of a bar in an edge-on spiral galaxy and determine its orientation. We use position-velocity diagrams (PVDs) obtained by projecting edge-on two-dimensional hydrodynamical simulations of the gas flow in a barred galaxy mass model. We show that when a nuclear spiral is formed, the presence of a gap in the PVDs, between the signature of the nuclear spiral and that of the outer parts of the disk, reliably indicates the presence of a bar. This gap is due to the presence of shocks and inflows in the simulations, leading to a depletion of the gas in the main and outer bar regions. If no nuclear spiral signature is present in a PVD, only indirect arguments can be used to argue for the presence of a bar. The shape of the signature of the nuclear spiral, and to a lesser extent that of the outer bar region, allows us to determine the orientation of the bar with respect to the line-of-sight. The presence of dust can also help to discriminate between viewing angles on either side of the bar. Simulations covering a large fraction of parameter space allow us to constrain the bar properties and mass distributions of observed galaxies. The strongest constraint comes from the presence or absence of the signature of a nuclear spiral in the PVD.

4.1 Introduction

The importance of bars in the structure of spiral galaxies is recognised in the Hubble sequence for the classification of galaxies (Sandage 1961). Theoretical studies of barred spiral galaxies branched early-on in a few directions, each providing insight into an aspect of barred galaxy structure. Studies of resonances and periodic orbits (see e.g. Contopoulos 1980; Contopoulos & Papayannopoulos 1980) provided a basic understanding of the general morphology and structure of barred spirals. Hydrodynamical simulations, either treating the gas as a collection of particles (e.g. Schwarz 1981; Combes & Gerin 1985) or as a continuous medium (e.g. Sanders & Huntley 1976; van Albada 1985), aimed to understand the particular distribution and kinematics of the gaseous component of barred galaxies, taking into account the effects of collisions and/or dissipation. N-body simulations, in most cases self-consistent, modelled the distribution and kinematics of the dominating stellar component of spirals (e.g. Combes & Sanders 1981; Sellwood 1981). These different approaches persist today but they are highly complementary (see e.g. Sellwood & Wilkinson 1993).

In Chapter 3, we highlighted the difficulties involved in the identification of bars in edge-on spiral galaxies. It is clear that the detection of such bars based on photometric or morphological criteria (e.g. de Carvalho & da Costa 1987; Hamabe & Wakamatsu 1989) is uncertain. Kuijken & Merrifield (1995; see also Merrifield 1996) were the first to show that the particular kinematics of barred disks could be used to identify bars in edge-on spirals. They showed that the periodic orbits in an edge-on barred galaxy produce characteristic double-peaked line-of-sight velocity distributions, which can be taken as the signature of a bar. In Chapter 3, we improved on the work of Kuijken & Merrifield (1995). We studied the signatures of individual periodic orbit *families* in the position-velocity diagrams (PVDs) of edge-on spirals (before combining them to model real galaxies), and examined how the PVDs depend on the viewing angle. We adopted a widely used mass model and a well-defined method to populate the orbits. Our aim was to provide insight into the projected kinematical structure of barred disks, and to provide guidance for interpreting stellar and gaseous kinematical observations of edge-on spirals.

We showed in Chapter 3 that the global appearance of a PVD can be used as a diagnostic to detect the presence of a bar in an edge-on disk. The signatures of the various periodic orbit families leave gaps in the PVDs which are a direct consequence of the non-homogeneous distribution of orbits in barred spiral galaxies. The signature of the x_1 periodic orbits is parallelogram-shaped and occupies all four quadrants of the PVDs, reaching very high radial velocities when the bar is seen end-on and only low velocities when the bar is seen side-on. The signature of the x_2 orbits, when present, is similar to that of the x_1 but reaches its maximum radial velocities at opposite orientations. Those features can be used to determine the viewing angle with respect to the bar in an edge-on disk. However, even if carefully chosen and populated, periodic orbits provide only an approximation to the structure and kinematics of the stellar and gaseous components of spiral galaxies. For example, a number of stars can be on irregular orbits, and no shock can develop.

In this chapter, we concentrate on developing bar diagnostics in edge-on disks using the gaseous component alone. We use the simulations of Athanassoula (1992b; hereafter A92b), designed to study the gas flow and shock formation in barred spiral galaxies. Unlike Chapter 3, these simulations properly take into account the fact that the gas is not a collisionless medium. The shocks and inflows which develop in the simulations lead to better bar diagnostics than those of Chapter 3. In addition, we run simulations covering a large fraction of the parameter space likely to be occupied by real galaxies. The PVDs produced can thus be directly compared with observations not only to detect the presence of bars in edge-on spiral galaxies, but also to constrain the mass distribution of the systems observed. In particular, in Chapter 5, we will apply those diagnostics to long-slit spectroscopic observations of a large sample of edge-on spiral galaxies, most of which have a boxy or peanut-shaped bulge. Our hope is to determine the formation mechanism of these objects and to study the vertical structure of bars. In Paper III, we will develop similar bar diagnostics for the stellar (collisionless) component of barred spiral galaxies, using fully self-consistent three-dimensional N-body simulations.

We describe the mass model and hydrodynamical simulations used in this chapter in § 4.2. In § 4.3, we study the signatures in the PVDs of the various components present in the simulations, and we develop bar diagnostics for edge-on disks. The influence of the parameters of the mass model are also discussed. The effects of dust extinction are illustrated in § 4.4, and we discuss the limitations of our models for the interpretation of real data in § 4.5. We conclude in § 4.6 with a brief summary of our main results.

4.2 Hydrodynamical Simulations

For the hydrodynamical simulations, we use the flux-splitting second-order scheme of G. D. van Albada (van Albada & Roberts 1981; van Albada, van Leer, & Roberts 1982; van Albada 1985). It is the same code as that used by A92b so we will only briefly review its main properties here.

The simulations are two-dimensional (infinitely thin) and time-dependent, and the gas is treated as ideal, isothermal, and non-viscous. We do not consider the self-gravity of the gas, so the flow is calculated using the potential described in Chapter 3 (see also Athanassoula 1992a; hereafter A92a). The mass model has two axisymmetric components, a Kuzmin/Toomre disk (Kuzmin 1956; Toomre 1963) and a bulge-like spherical density distribution. They combine to yield a flat rotation curve in the outer parts of the disk. We use a homogeneous ($n = 0$)

or inhomogeneous ($n = 1$) Ferrers spheroid (Ferrers 1877) as a third component representing the bar. Each model is described by four main parameters: the bar axial ratio a/b, the bar quadrupole moment Q_m (proportional to the mass of the bar), the Lagrangian radius r_L (the radius of the Lagrange points L_1 and L_2 on the major axis of the bar), and the central concentration ρ_c. We recall that the bar semi-major axis is fixed at $a = 5$ kpc, but refer the reader to A92a and Chapter 3 for a more detailed discussion of the mass model.

The simulations are started with a massless bar and an additional axisymmetric component of mass equal to that of the desired final bar. Mass is transfered from that component to the bar over 10^8 yr and the simulations are run until the gas flow is roughly stationary in the frame of reference corotating with the bar (about 10 bar revolutions). An 80×160 cells grid is used to cover a disk of 16 kpc radius, assuming bisymmetry. The inner half of the simulations is then regridded to the 80×160 grid, and the simulations continued for another 5 bar revolutions using this increased spatial resolution (0.1×0.1 kpc^2 cell size; see van Albada & Roberts 1981). Because we only analyse simulations which have reached a steady state, the path of the fluid elements coincide with the streamlines considered in this chapter. Star formation and mass loss are modelled crudely. The gas density is lowered artificially in high density regions and gas is added uniformly over the grid. This process is governed by the equation

$$d\rho_g/dt = \alpha\rho_{g,init}^2 - \alpha\rho_g^2, \tag{4.1}$$

where ρ_g is the gas density, α is a constant (set to 0.3 $M_\odot^{-1}$ pc^2 Gyr^{-1} in most runs), and $\rho_{g,init} = 1 M_\odot$ pc^{-2} is the uniform initial gas density. It therefore takes about 3 Gyr for the gas to be reprocessed.

As in Chapter 3, the models considered are those of A92a (see her Table 1). We will also use her units: 10^6 $M_\odot$ for masses, kpc for lengths, and km s^{-1} for velocities. It is essential to understand the orbital structure of the models to interpret properly the results of the simulations. Orbital properties have been discussed in A92a and Chapter 3, but also in Athanassoula et al. (1983), Papayannopoulos & Petrou (1983), Teuben & Sanders (1985), and others. Here, we will mainly use A92a and Chapter 3 for comparison. We will also draw heavily on the results of A92b, who used the same set of simulations but for different purposes.

4.3 Bar Diagnostics

4.3.1 Detecting Edge-On Bars

The main goal of Chapter 3 and of this chapter is to develop kinematical bar diagnostics in edge-on spiral galaxies, in order to remedy the inadequacies of an identification based exclusively on the light distribution of the objects. Our main tool is the PVDs, representing the projected density of material in the edge-on disks as a function of line-of-sight velocity and projected position along the major axis (see also Kuijken & Merrifield 1995; Merrifield 1996). In distinction to Chapter 3, where we had to choose a simple method to combine the families of periodic orbits and model the gas distribution of real galaxies, the present hydrodynamical simulations inherently produce the gas density and velocities simultaneously, so that the "right" orbits are naturally populated. The PVDs produced in this chapter can therefore be directly compared with emission line spectroscopic observations of edge-on spiral galaxies (long-slit spectroscopy, Fabry-Perot observations, radio synthesis line-imaging, etc. . .).

The PVDs presented were obtained by projecting the simulations edge-on and observing them from various viewing angles. Since we are mostly interested in the bar region, we use only the inner 8×8 kpc^2 of the simulations, covered by the high resolution grid. Because the force of the bar decreases steeply with radius, the motion of the gas at large radii can, to first order, be considered circular, and including the outer region would make no difference to our PVDs.

In this section, we will concentrate on understanding the PVDs of two inhomogeneous bar models which are prototypes of models with and without inner Lindblad resonances (ILRs). As suggested in A92a, we will identify the existence and position of the ILRs with the existence and extent of the x_2 periodic orbits. The two models considered are the same as in Chapter 3: model 001 ($a/b = 2.5$, $Q_m = 4.5\times10^4$, $r_L = 6.0$, $\rho_c = 2.4\times10^4$) and model 086 ($a/b = 5.0$, $Q_m = 4.5\times10^4$, $r_L = 6.0$, $\rho_c = 2.4 \times 10^4$). We will then extend our results to other models and analyse how the bar diagnostics developed vary as the parameters of the mass model are changed.

4.3.2 Model 001 (ILRs)

Figure 4.1 shows the face-on surface density of the gas and PVDs for model 001, which has ILRs. Unlike the models of Chapter 3, which are symmetric about both the minor and major axes of the bar, the present simulations are only bisymmetric, so we need to cover a viewing angle range of 180°. The viewing angle ψ is defined to be 0° for a line-of-sight parallel to the major axis of the bar and 90° for a line-of-sight perpendicular to it, increasing counterclockwise in the surface density plots.

As was shown in A92b (see Fig. 2 of that paper, or the surface density plot in Fig. 4.1), there is very little gas in the main and outer bar regions. The two strong parallel narrow segments represent offset shocks on the leading sides of the bar, displaying strong density enhancements, sharp velocity gradients, and

Figure 4.1: Gas distribution and position-velocity diagrams of model 001. The upper-left plot shows the face-on logarithmic gas surface density of the simulation. We use logarithmic values (for the density distribution alone) because the dynamic range of the gas surface density is high. Dark shades denote low density regions. The bar is at 45° to the horizontal, has a semi-major axis length of 5 kpc, and is rotating clockwise. The size of the box is 8×8 kpc^2. The other plots show position-velocity diagrams (projected density of material as a function of line-of-sight velocity and projected position along the major axis) of the gas when the simulation is viewed edge-on. For those plots, dark shades denote high density regions. The angle between the line-of-sight and the bar is indicated in the top-left corner of each diagram, a viewing angle of $\psi = 0°$ indicating that the bar is seen end-on (line-of-sight parallel to the bar) and a viewing angle of $\psi = 90°$ indicating that the bar is seen side-on (line-of-sight perpendicular to the bar). The viewing angle increases counterclockwise in the surface density plots.

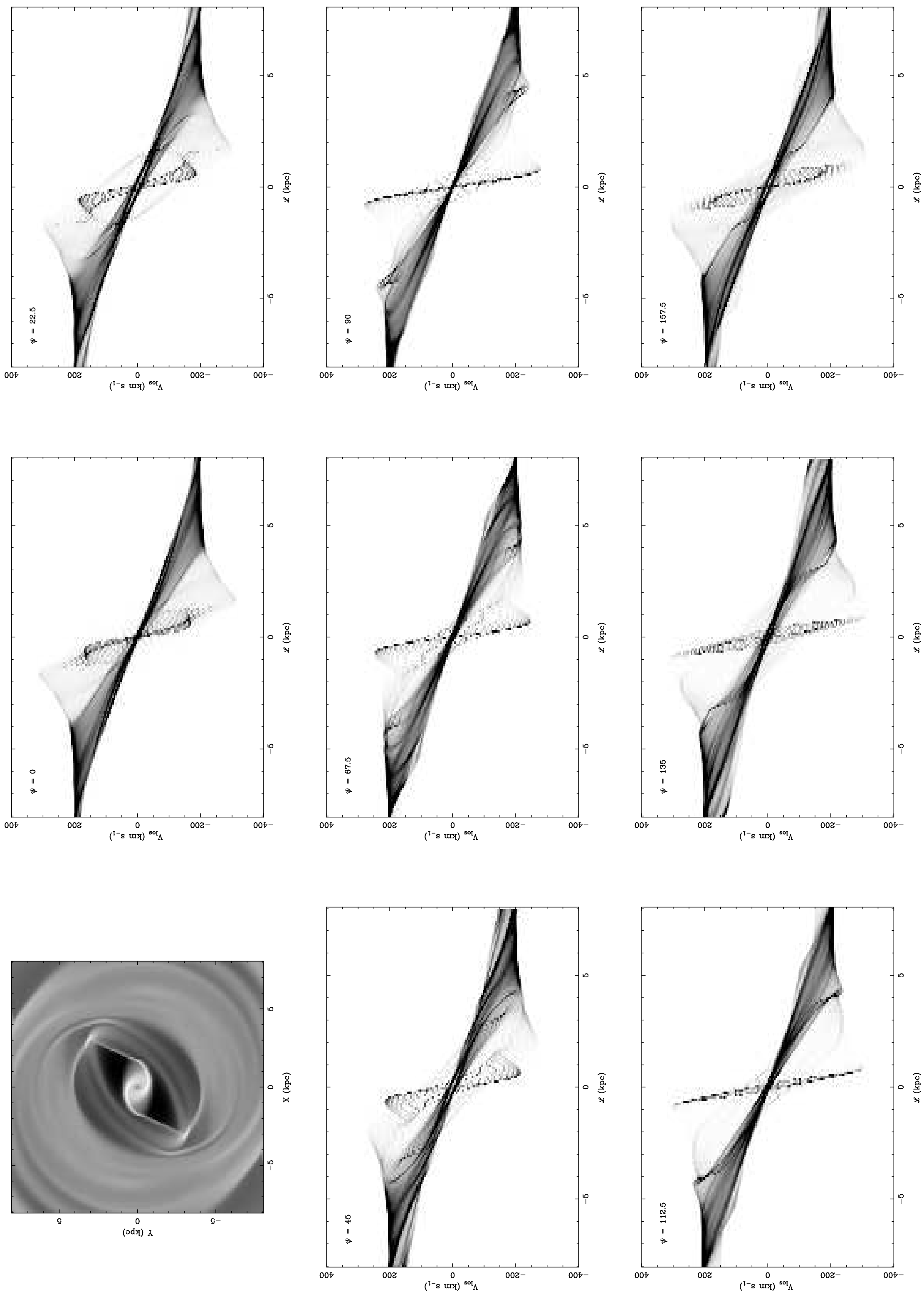

Figure 4.1: *See caption previous page.*

regions of high shear (A92b). They can be identified with the dust lanes observed in barred spiral galaxies. Strong density enhancements can also be seen at the ends of the bar major axis, roughly perpendicular to it. In the inner parts of the bar is a very intense two-armed "nuclear spiral", connecting with the offset shocks. Outside the bar region, the surface density is almost featureless; only a few spiral arms segments are seen. In the outer bar region, the streamlines have roughly the shape and the orientation of the x_1 periodic orbits. As one moves inward, the streamlines change gradually to the shape and orientation corresponding to the x_2 periodic orbits. This flow pattern leads to the offset shocks and results in an inflow of gas toward the nuclear region, accounting for the gas distribution in the bar: low densities in the main and outer parts of the bar, and high densities in the center (A92b). As we already mentioned, the flow is almost circular outside the bar region.

The PVDs in Figure 4.1 show the existence of three distinct regions: an inner region, corresponding to the nuclear spiral; an intermediate region, corresponding to the main and outer parts of the bar; and an external region, corresponding to the region outside the bar. It is important to notice how low the density of the intermediate region is, compared to that in the other two regions. This is no surprise since, as mentioned in A92b and above, most of the bar region has very low gas density, with the exception of the central region and the two shock loci. Let us now examine each of the three regions separately, by keeping only the gas in the targeted region (and masking out the gas in the other regions) when calculating the PVDs.

Figure 4.2 shows the surface density and PVDs of model 001 when considering the low density main and outer bar regions only. Because the high density regions have been masked out and because we are looking only at relatively low density regions, we see much more structure in the PVDs of Figure 4.2 than in the corresponding sections of the PVDs of Figure 4.1.

To see what the various components of the gas density contribute to the PVDs, we have also masked out all areas except for the shock loci along the leading sides of the bar, or the density enhancements near the ends of the bar major axis (not shown). The gas in the shock loci does not contribute any very outstanding features to the PVDs, the main reason being that the amount of gas integrated along most lines-of-sight is small, since the features are very narrow. At $\psi = 22.5°$, when the line-of-sight is parallel to the shock loci, they contribute the two linear segments which separate the "dark" and "light" regions of the PVD slightly inside $L = \pm 2$. The high density enhancements near the ends of the bar major axis contribute the very strong straight line segments going through the center at $\psi = 0°$ and 22.5°. For these angles, they are seen roughly as segments of circles. For viewing angles near 90°, they give rise to the undulating parts of the PVDs

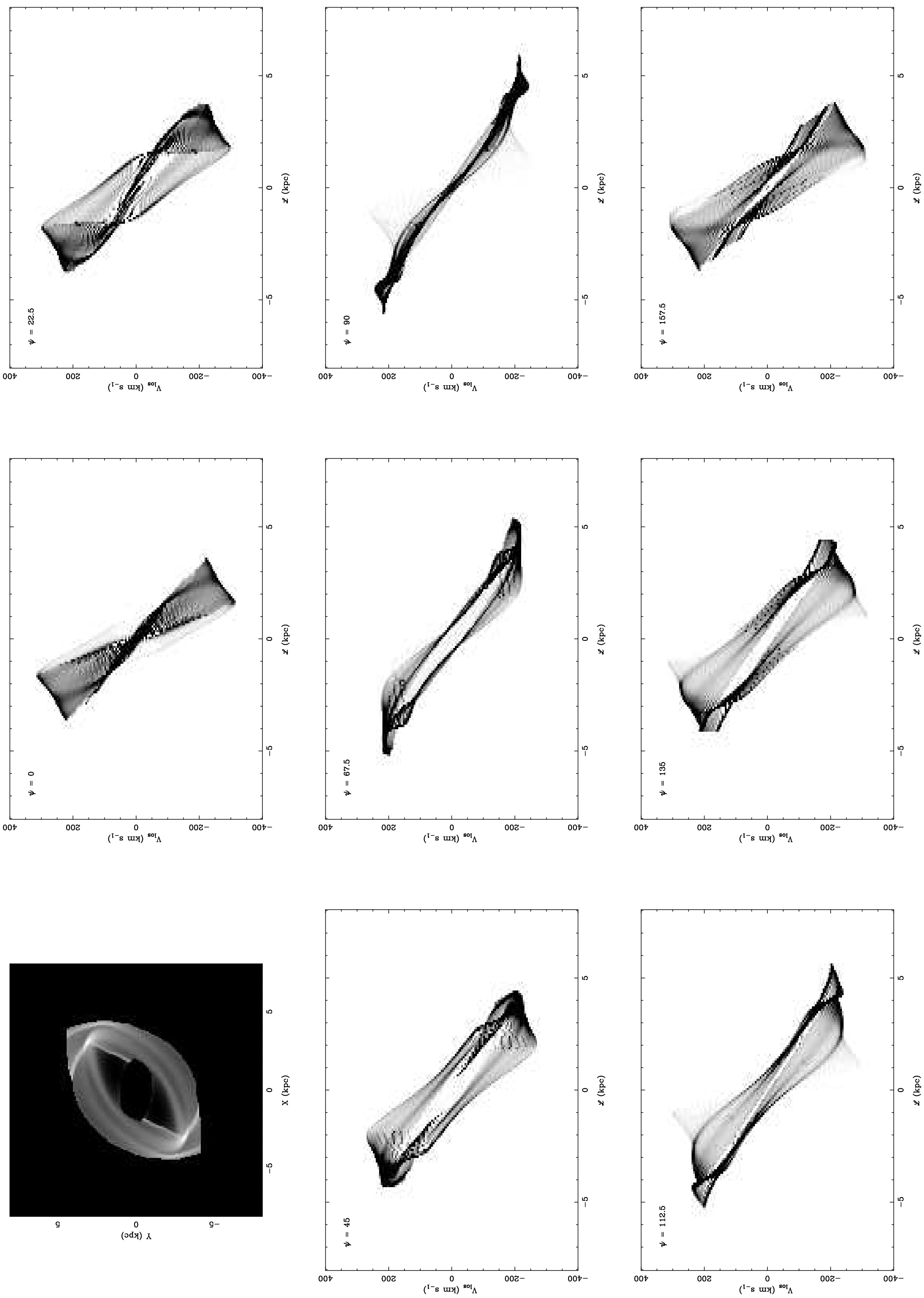

Figure 4.2: Same as Figure 4.1 but for the low density main and outer bar regions of model 001 only.

at large radii.

When compared with Figure 3.4, Figure 4.2 shows, at first glance, many similarities, but also, when scrutinised more closely, a number of differences. This could be expected since the gas streamlines follow loosely, but not exactly, the shape and orientation of the x_1 orbits, which are elongated parallel to the bar.

The parallelogram-shaped signature of the x_1 orbits in Figure 3.4 is again observed here and the "forbidden" quadrants are again populated. This is due to the fact that both the x_1 orbits and the streamlines in the main and outer bar regions are not circular, but elongated. In the gas, however, the parallelogram shape is also present for $\psi = 0°$, while the PVD of the x_1 orbits showed a bow-shaped feature. The reason is that, unlike the x_1 orbits, the streamlines do not have their major axes parallel to that of the bar, but rather at an angle of about 20° to it (see A92b). Also, at $\psi = 90°$, the x_1 orbits show a near-linear PVD, while the gas shows an additional faint bow-shaped feature near the center (the feature is visible for $67.5° \lesssim \psi \lesssim 135°$). Masking a larger fraction of the simulation (not shown), it is possible to show that the extra feature, which reaches high radial velocities, arises from the very low density regions just inside the offset shocks, close to the major axis of the bar. In this section of the bar region, the flow differs substantially from the behaviour of the x_1 periodic orbits.

The elongated "hole" in the center of the PVDs, seen at intermediate viewing angles, is present in both sets of PVDs, and is due to the way the x_1 orbit family was terminated and the way the gas density was masked. This causes in both cases an absence (or low-density) of quasi-circular streamlines near the end of the bar.

For $\psi = 0°$, the maximum velocity in the PVD occurs near the center; for $\psi = 90°$, it occurs at the largest radii. This was also found for the PVDs of the x_1 orbits in Chapter 3, where it was explained by considering the trace of an elongated orbit in a PVD as a function of the viewing angle and (average) distance from the center. The explanation is analogous here. Because the streamlines in the main and outer bar regions become more elongated with decreasing radius, the envelope of their signature in the PVDs increases rapidly with decreasing projected distance for viewing angles close to 0°/180°, and decreases with decreasing projected distance for viewing angles close to 90° (the streamlines are elongated parallel to the bar in those regions). We refer the reader to Chapter 3 for a fuller explanation. There is also a reduced degree of symmetry with respect to the viewing angles 0° and 90°, in particular as far as the angles 67.5° and 112.5° are concerned. They are, of course, identical in the periodic orbits PVDs of Chapter 3. This is because the flow is strongly bisymmetric, as opposed to being almost symmetric with respect to both axes of the bar (see Fig. 2 of A92b).

In Figure 4.2, we see that the radial velocities are maximum (compared to the circular velocity) for lines-of-sight almost parallel to the bar (highest values for $0°$ and $157.7°$), and decrease as ψ increases, to reach a minimum when the line-of-sight is roughly along the bar minor axis (lowest values for $90°$ and $67.5°$). This was to be expected since, like the x_1 orbits, the streamlines in the main and outer parts of the bar are elongated parallel to it. Similarly, the position where the maximum occurs moves out as the viewing angle increases from $\psi = 0°$ to $\psi = 90°$ (see above). However, the maxima generally occur at a larger distance from the center than in the case of the x_1 orbits (this is easily seen by comparing Fig. 3.4 and 4.2). This is due to the fact that the x_1-like flow does not extend up to the center of the hydrodynamical simulation, contrary to the x_1 periodic orbits of Chapter 3, but is truncated at a certain radius. For example, the nuclear spiral, which has an x_2-like behaviour, extends to about 1.6 kpc on the bar minor axis, which is exactly the projected distance at which the envelope of the signature of the main bar region drops abruptly for $\psi = 0°$.

We can repeat the masking process to keep only the region of the simulation containing the nuclear spiral, as shown in Figure 4.3. Comparing the PVDs thus obtained with those of the x_2 family of periodic orbits (Fig. 3.5), we again find both similarities and differences. In both cases, we see inverted S-shaped features or near straight segments passing through the center. This is explained by the decrease of the streamlines eccentricity with decreasing radius (see Ch. 3 for a more thorough explanation). More similarity is found if we compare PVDs at viewing angles differing by about $20°$, i.e. comparing the gaseous PVD at $\psi = 112.5°$ with the orbital one at $\psi = 90°$. This offset corresponds to the offset of the straight shocks with respect to the major axis of the bar (A92b). Also, the PVDs of the nuclear spiral are more asymmetric with respect to the viewing angles $0°$ and $90°$ (e.g. comparing the PVDs at $\psi = 22.5°$ and $\psi = -22.5° = 157.5°$) than the PVDs of the main and outer bar regions. This effect is due to the stronger bisymmetry of the nuclear spiral.

Because the streamlines in the central region are elongated perpendicular to the bar, like the x_2 orbits, higher radial velocities (compared to the circular velocity) are reached when the bar is seen side-on than when the bar is seen end-on. Considering the maximum velocity of the PVDs as a function of the viewing angle, we find that it is highest for $\psi = 112.5°$ and $135°$ and lowest for $\psi = 0°$ and $22.5°$, in agreement with the offset mentioned above. The "hole" in the parallelogram-shaped signature of the x_2 orbits (see Fig. 3.5) has completely disappeared in the hydrodynamical simulation, because the x_2-like behaviour of the gas flow persists past the inner ILR and the flow becomes almost circular in the very center.

Figure 4.4 isolates the signature of the region outside the bar in the PVDs. Because the influence of the bar decreases rapidly with radius, the flow outside the bar is close to circular. A perfectly circular orbit would yield an identical

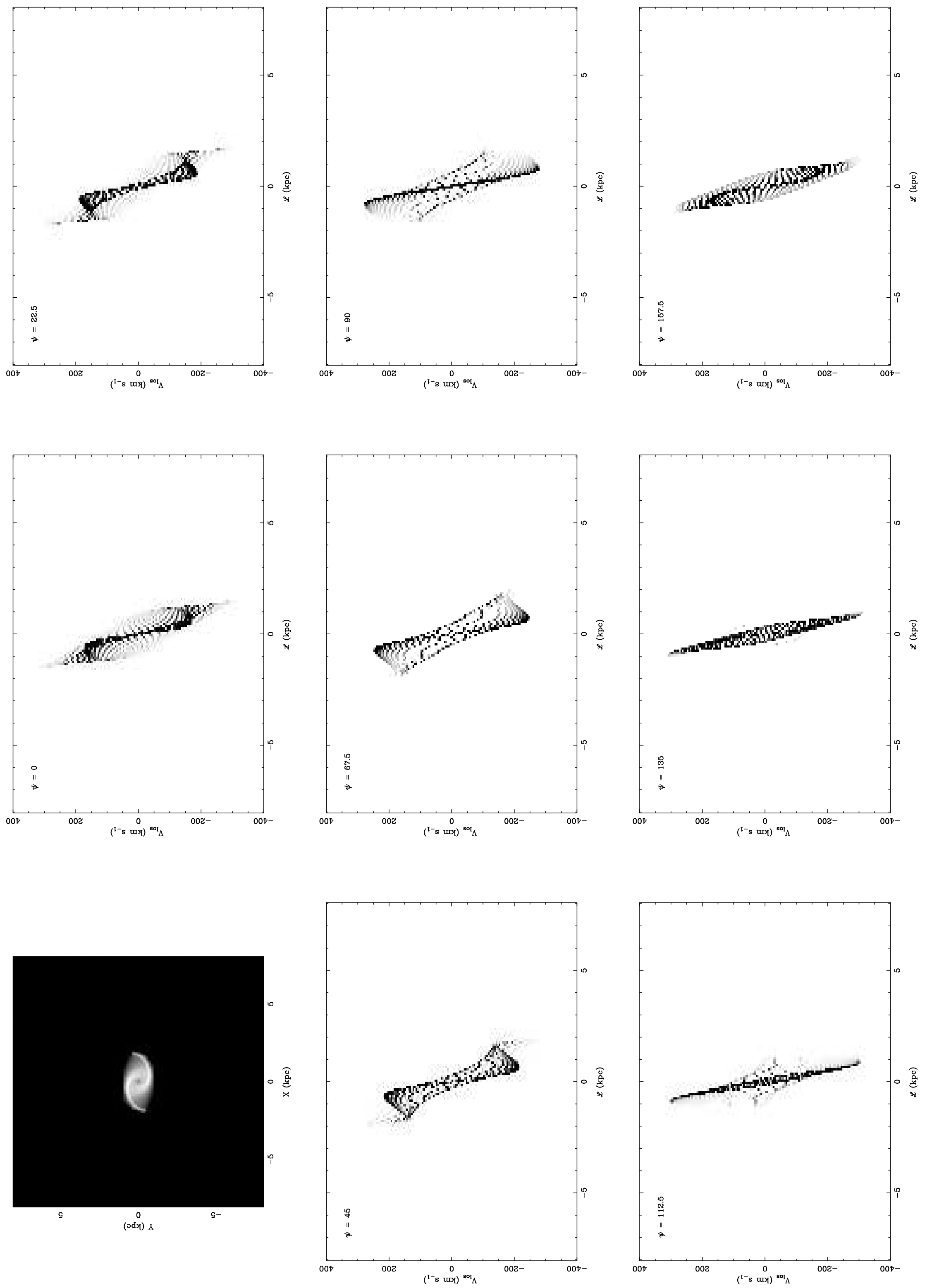

Figure 4.3: Same as Figure 4.1 but for the high density nuclear spiral region of model 001 only.

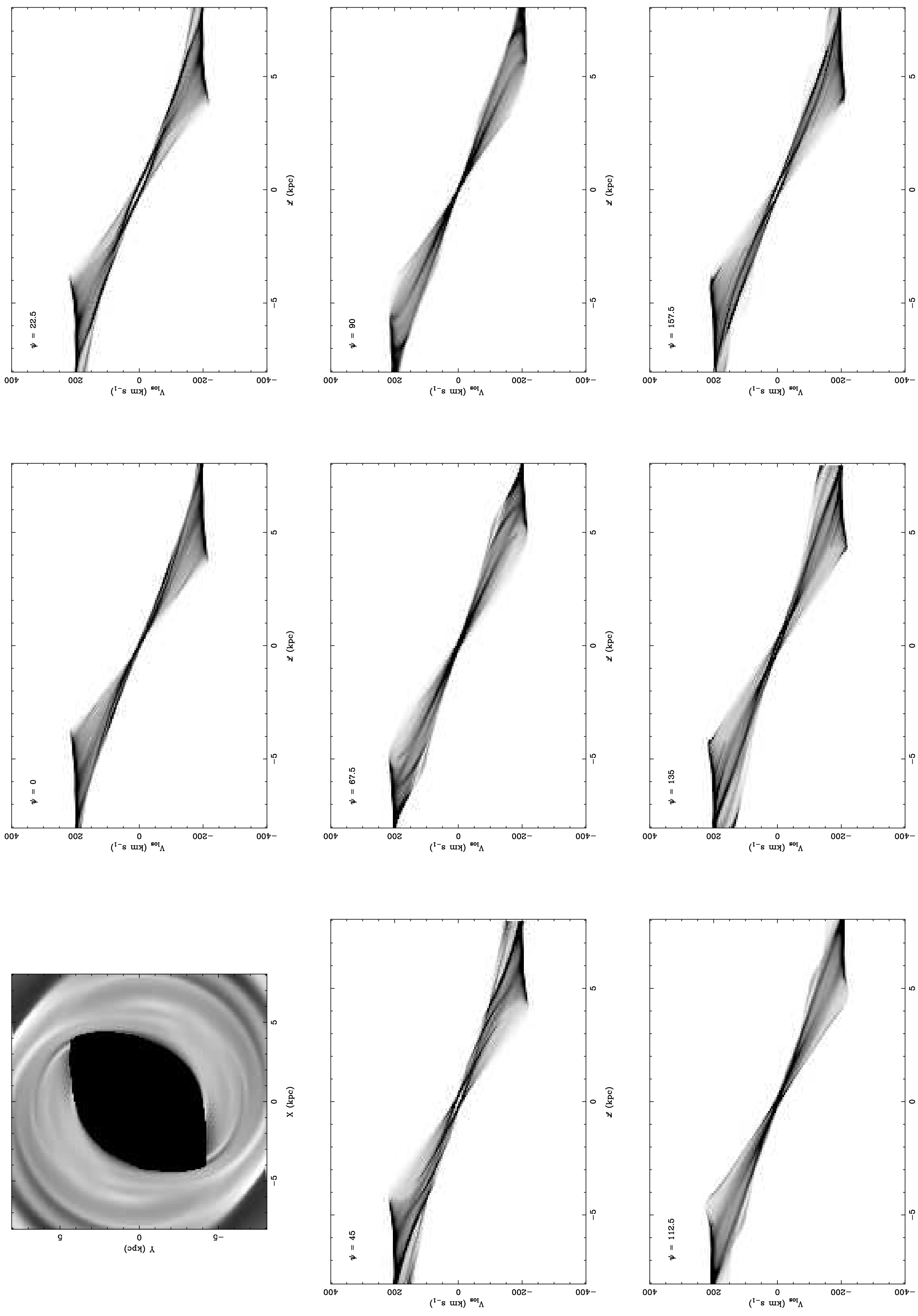

Figure 4.4: Same as Figure 4.1 but for the high density outer regions of model 001 only.

inclined straight line passing through the origin in all PVDs. The structure seen here can thus be thought of as a succession of near-circular orbits of increasing radii, yielding the "bow tie" signature observed. The "hole" seen in the center of the PVDs at certain viewing angles (e.g. $\psi = 45°$) is again due to the fact that the orbits are not perfectly circular (see Fig. 3.6). The strong almost solid-body features forming loop-like structures near the upper and lower limits of the envelope of the signature are due to tightly wound spiral arms in the outer disk.

4.3.3 Model 086 (no-ILRs)

Figure 4.5 shows the face-on surface density distribution of model 086, which has no ILRs (or, equivalently, has no x_2 periodic orbits), and the PVDs obtained using an edge-on projection. The main difference from the density distribution of model 001 is the absence of any significant nuclear spiral. The strong straight and narrow features in the center of the bar are centered shocks, caused by the high curvature of the streamlines near the major axis of the bar (see Fig. 4 in A92b). Similarly, the x_1 orbits in this model have high curvatures or loops near their major axes. The shock loci do not curve near the center because no streamlines perpendicular to the bar exist; there are no x_2 periodic orbits in this model. The shocks, however, still drive an inflow of gas, resulting in the *entire* bar region being gas depleted. As expected, the region outside the bar is almost unaffected by the change in the bar axial ratio compared to model 001.

The PVDs in model 086 reflect all of the above properties. In particular, they lack the central feature associated with the nuclear spiral in model 001, and the signature of the main and outer bar regions is very faint (Fig. 4.5 should be contrasted with Fig. 4.1). Because of the absence of an x_2-like flow in the central region of the simulation, the x_1-like flow extends inward all the way to the center. In good agreement with what happens for the periodic orbits (see Ch. 3 or A92a), the streamlines are also much more eccentric than those of model 001. The parallelogram-shaped envelope of the signature of the main and outer bar regions in the PVDs therefore reaches even more extreme radial velocities (compared to the circular velocity) than in model 001, and the rising part of the envelope extends almost all the way to the center for viewing angles close to $0°/180°$ (see also Fig. 3.9). When the bar is seen close to end-on, radial velocities more than twice those in the outer parts are reached. These velocities decrease rapidly as the viewing angle approaches $\psi = 90°$. As in the case of model 001, the regions outside the bar lead to a strong almost solid-body component in all PVDs.

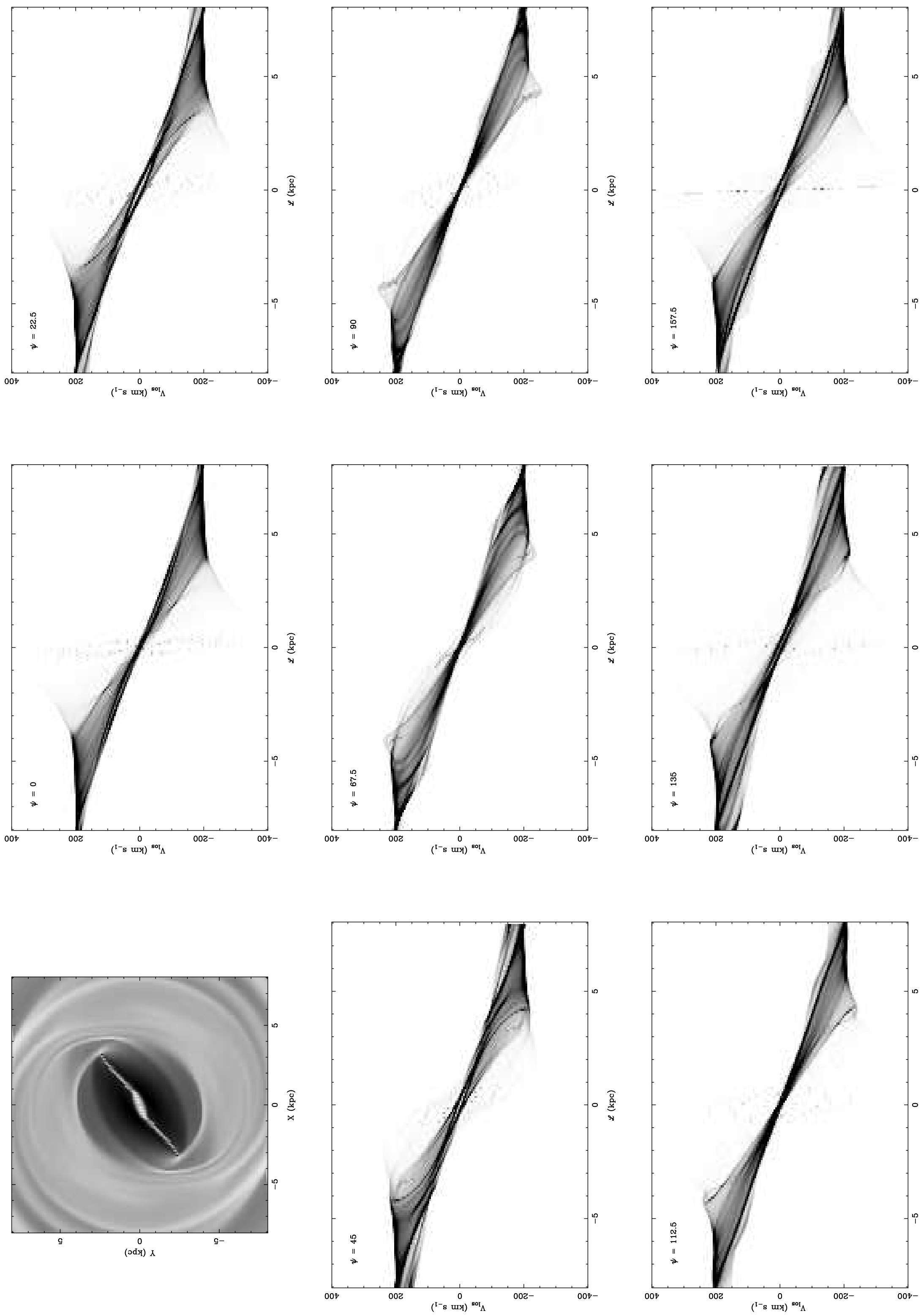

Figure 4.5: Same as Figure 4.1 but for model 086.

4.3.4 Other Models

Now that the general characteristics of the gas flow in models with and without ILRs are understood, it is possible to explore how the gas behaviour changes when the parameters of the mass model are varied. We can hope thereby not only to extend the diagnostics developed to identify bars in edge-on spiral galaxies (and their orientations relative to the line-of-sight), but also to develop criteria allowing us to constrain the bar properties and mass distribution of the systems. To achieve this, we will analyse sequences of simulations corresponding to the ranges along the axes of parameter space likely to be occupied by real galaxies. We will concentrate on understanding the gas flow within the barred region of the simulations, and will use extensively for that purpose the results of A92a and A92b. In particular, A92b showed that nuclear spirals occur in models with an extended x_2 family of periodic orbits and lead to offset shocks, while centered shocks occur in models with no or shortly extended x_2 orbits. She also showed that x_1 periodic orbits with a high curvature near the bar major axis are essential to the formation of shocks, and that such shocks lead to an inflow of gas toward the central region of the simulations, depleting the main and outer bar regions.

Figure 4.6 shows a sequence of simulations with varying bar axial ratio a/b (the other parameters are kept fixed at those of model 001). The figure shows, for each simulation, the face-on surface density distribution and the velocity field (with a few streamlines) in the frame of reference corotating with the bar. It also shows the PVDs obtained for various viewing angles with respect to the bar when the simulation is viewed edge-on. To limit the number of figures, and since there is some degree of symmetry with respect to $\psi = 0°$ and $90°$, we do not show any PVDs with $\psi > 90°$. Nevertheless, such viewing angles were considered, and the corresponding results will be included in the discussion whenever necessary.

For small bar axial ratios, when the effect of the bar is similar to that of an oval distortion and the shocks are short and curved, the main bar region is not strongly gas depleted and its signature is easily visible in the PVDs. As we consider simulations with increasingly higher bar axial ratios, the density in the region of the PVDs which corresponds to the main and outer bar regions drops considerably. It reaches its lowest values for the highest bar axial ratio considered ($a/b = 5$), for which the shock loci are straight and close to the bar major axis.

In Figure 4.6, the envelope of the signature of the main and outer bar regions in the PVDs becomes more extreme as the bar axial ratio is increased: the maximum radial velocities reached for small viewing angles increase and the positions of the maxima get closer to the center. The opposite is true for large viewing angles. This is easily understood because, as the bar axial ratio increases, the eccentricity of the streamlines in the main and outer bar regions (and that of the x_1 orbits, see A92a) also increases, leading to higher velocities along the line-of-sight when

Figure 4.6: Gas distribution and position-velocity diagrams for a sequence of models of increasing bar axial ratio a/b. The models are 010, 005, 001, 083, and 086, with, respectively, $a/b = 1.5$, 2.0, 2.5, 3.0, and 5.0. The other parameters of the models are kept fixed at those of model 001. The first row of plots shows the face-on logarithmic gas surface densities of the simulations. We use logarithmic values (for the density distributions alone) because the dynamic range of the gas surface densities is high. Dark shades denote low density regions. The bar is at 45° to the horizontal, has a semi-major axis length of 5 kpc, and is rotating clockwise. The size of the box is 8×8 kpc^2. The second row of plots shows velocity vectors and gas streamlines in the frame of reference corotating with the bar. The following rows of plots show position-velocity diagrams (projected density of material as a function of line-of-sight velocity and projected position along the major axis) of the gas when the simulations are viewed edge-on. For those plots, dark shades denote high density regions. The angle between the line-of-sight and the bar is indicated in the top-left corner of the first diagram of each row, a viewing angle of $\psi = 0°$ indicating that the bar is seen end-on (line-of-sight parallel to the bar) and a viewing angle of $\psi = 90°$ indicating that the bar is seen side-on (line-of-sight perpendicular to the bar). The viewing angle increases counterclockwise in the surface density plots.

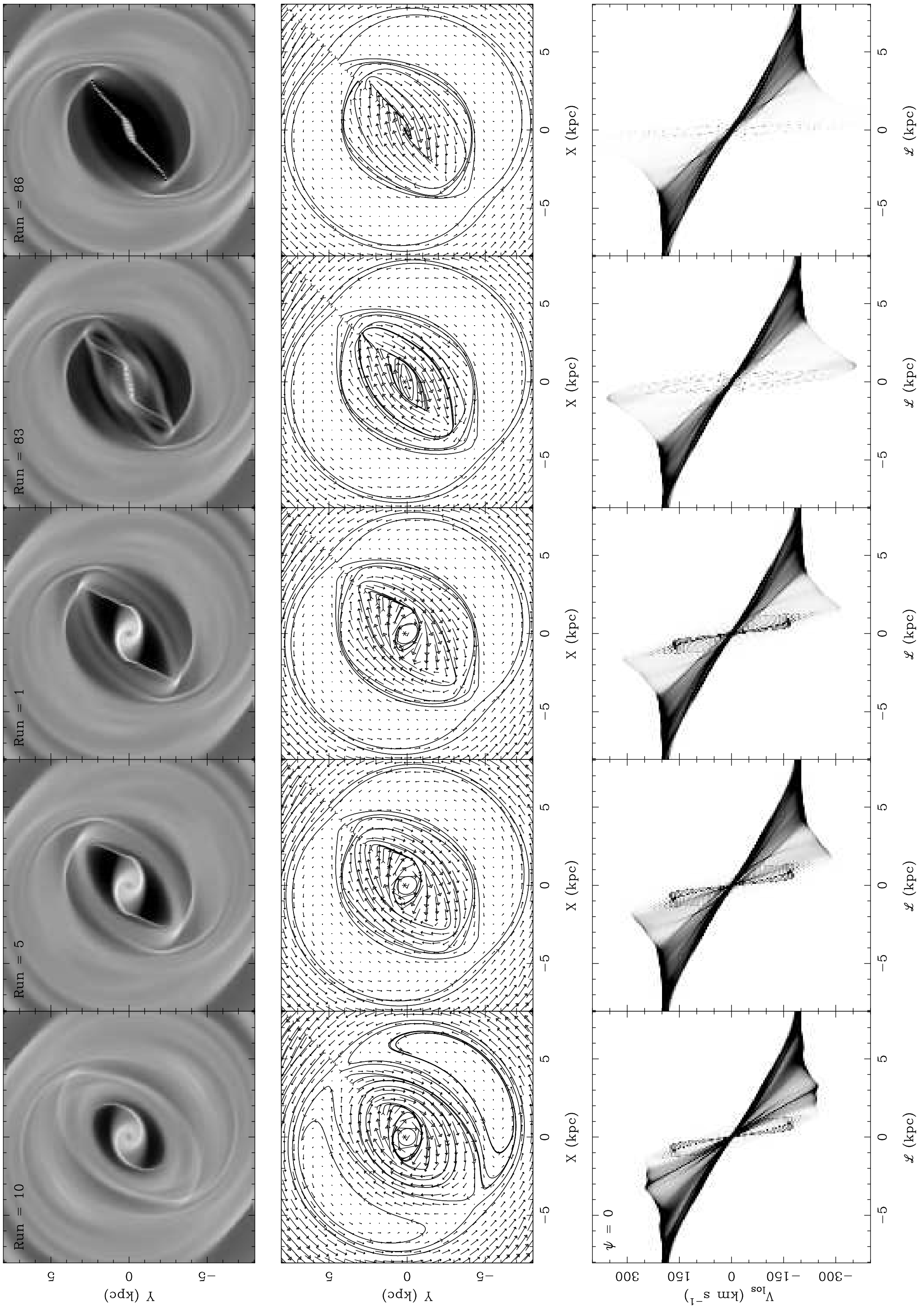

Figure 4.6: *See caption previous page.*

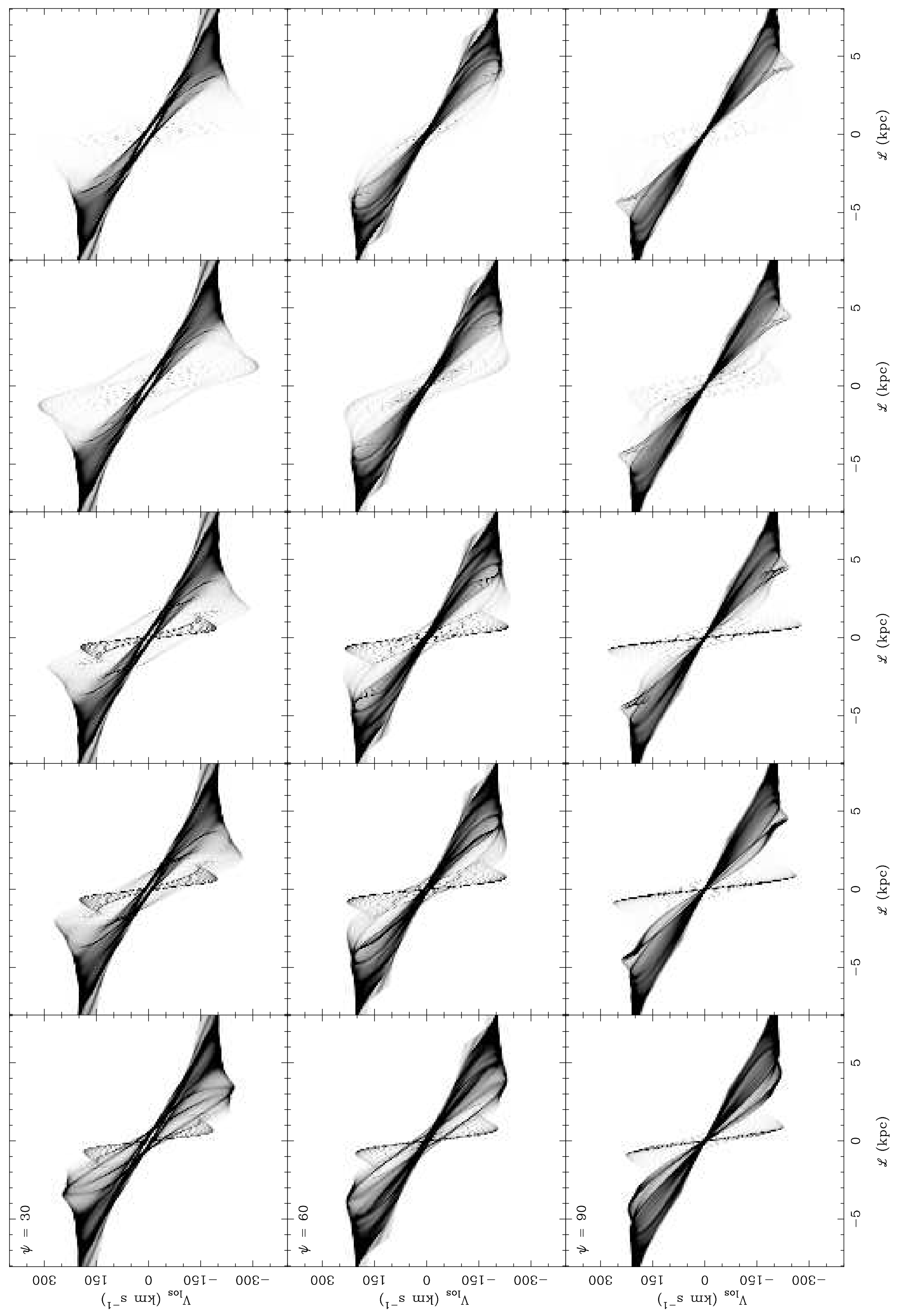

Figure 4.6: *Continued.*

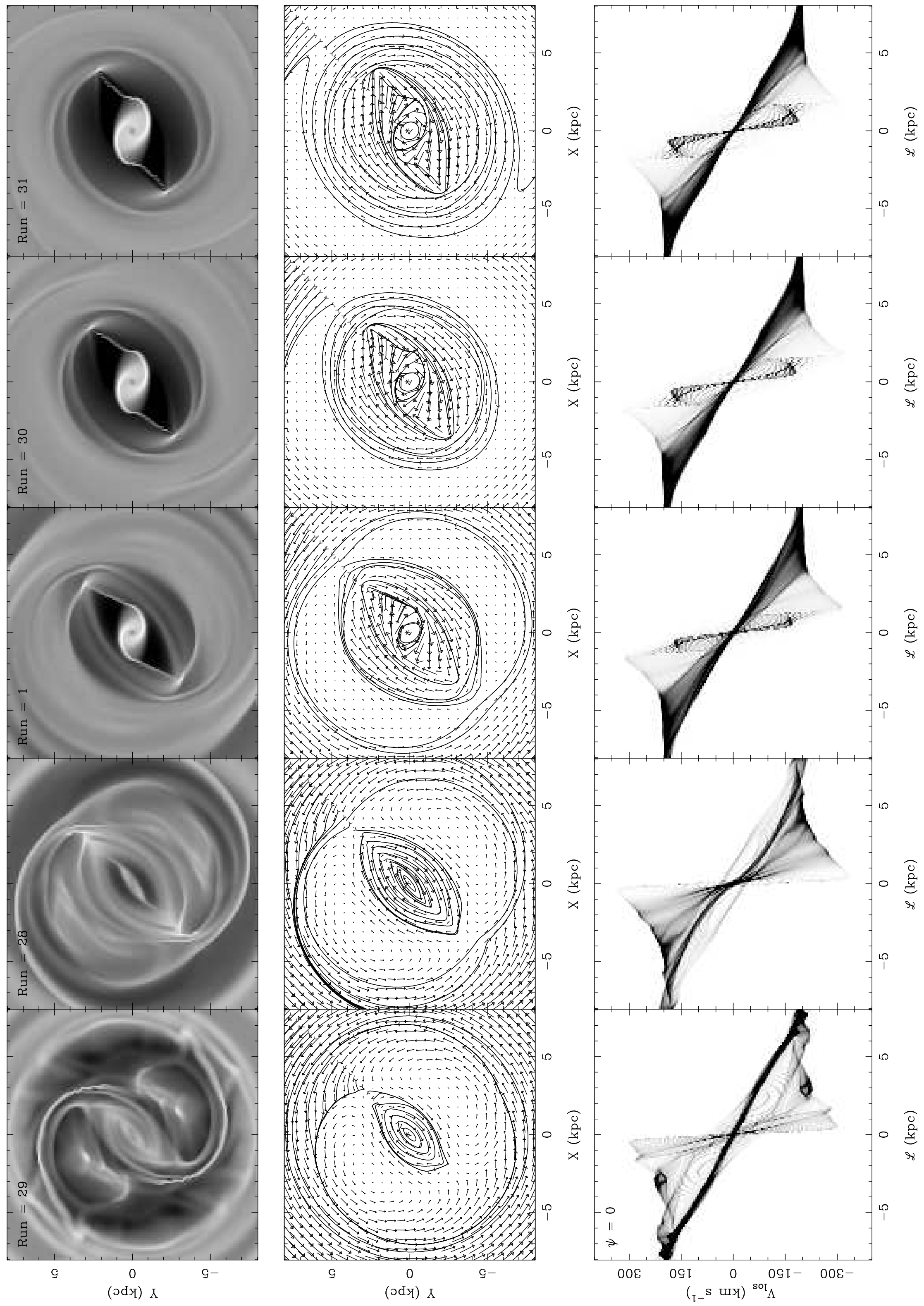

Figure 4.7: Same as Figure 4.6 but for a sequence of models of increasing Lagrangian radius r_L. The models are 029, 028, 001, 030, and 031, with, respectively, $r_L = 4.0$, 5.0, 6.0, 7.0, and 8.0. The other parameters of the models are kept fixed at those of model 001.

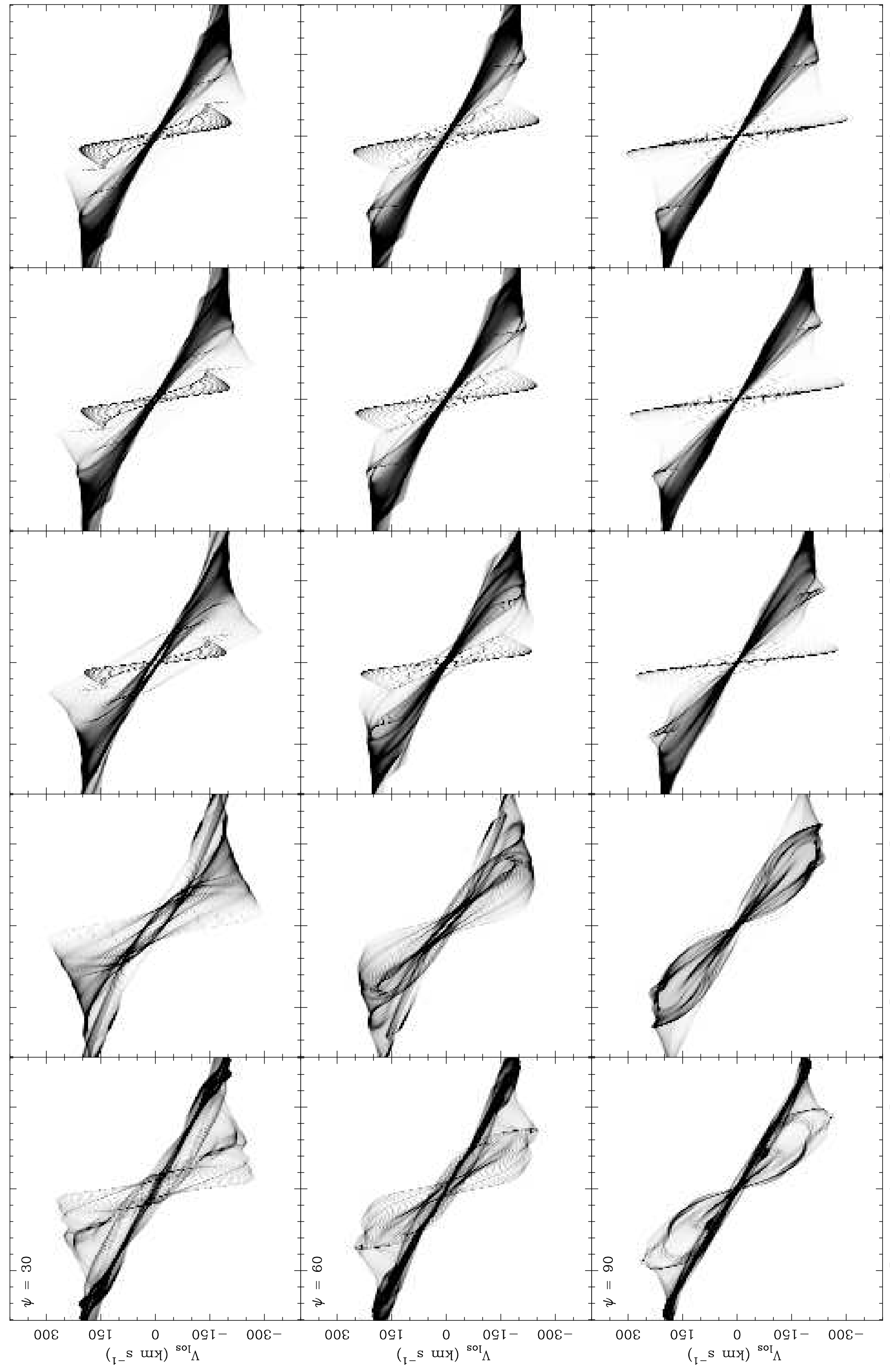

Figure 4.7: *Continued.*

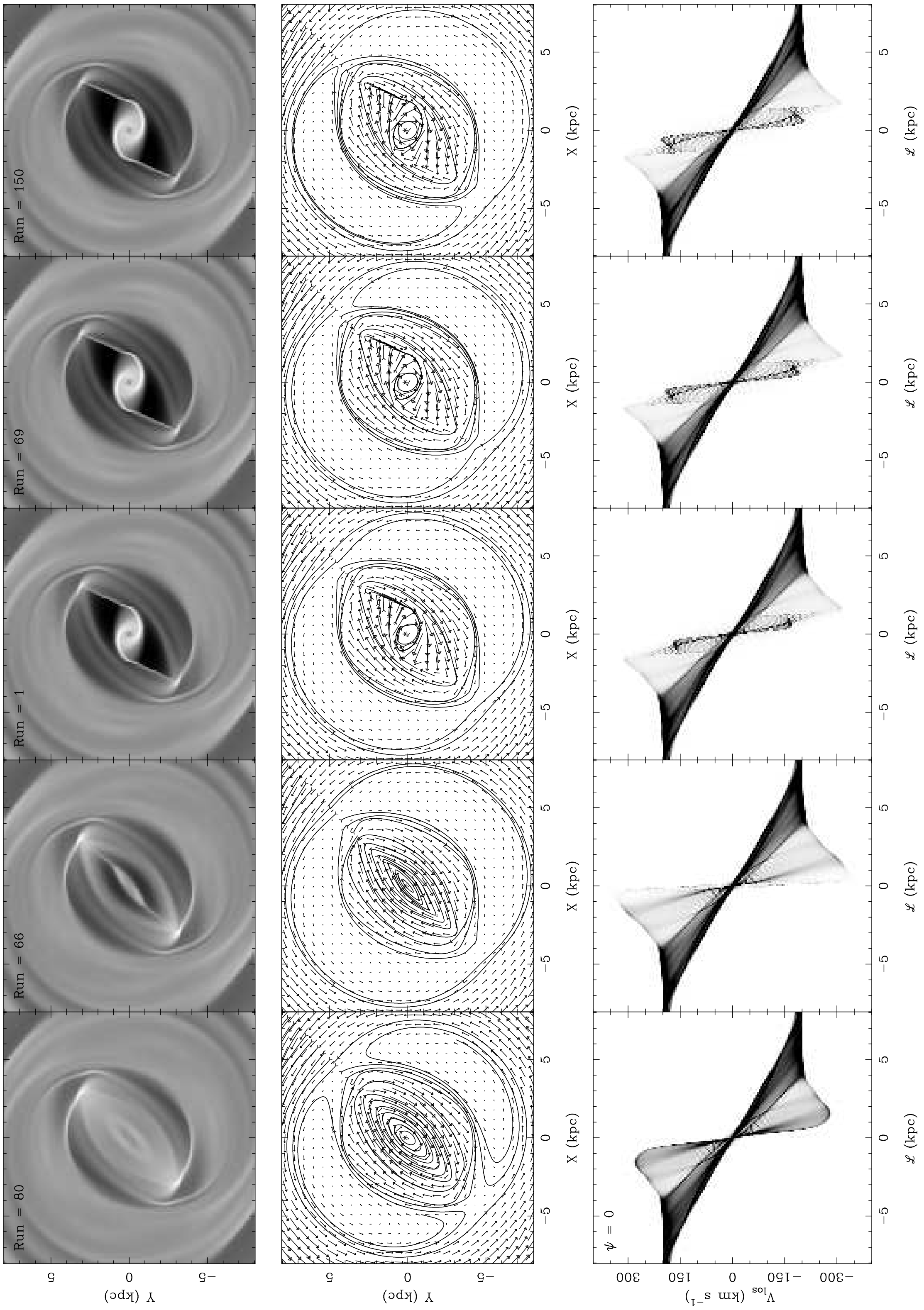

Figure 4.8: Same as Figure 4.6 but for a sequence of models of increasing central density ρ_c. The models are 080, 066, 001, 069, and 150, with, respectively, $\rho_c = 0.4 \times 10^4$, 1.6×10^4, 2.4×10^4, 3.2×10^4, and 4.0×10^4. The other parameters of the models are kept fixed at those of model 001.

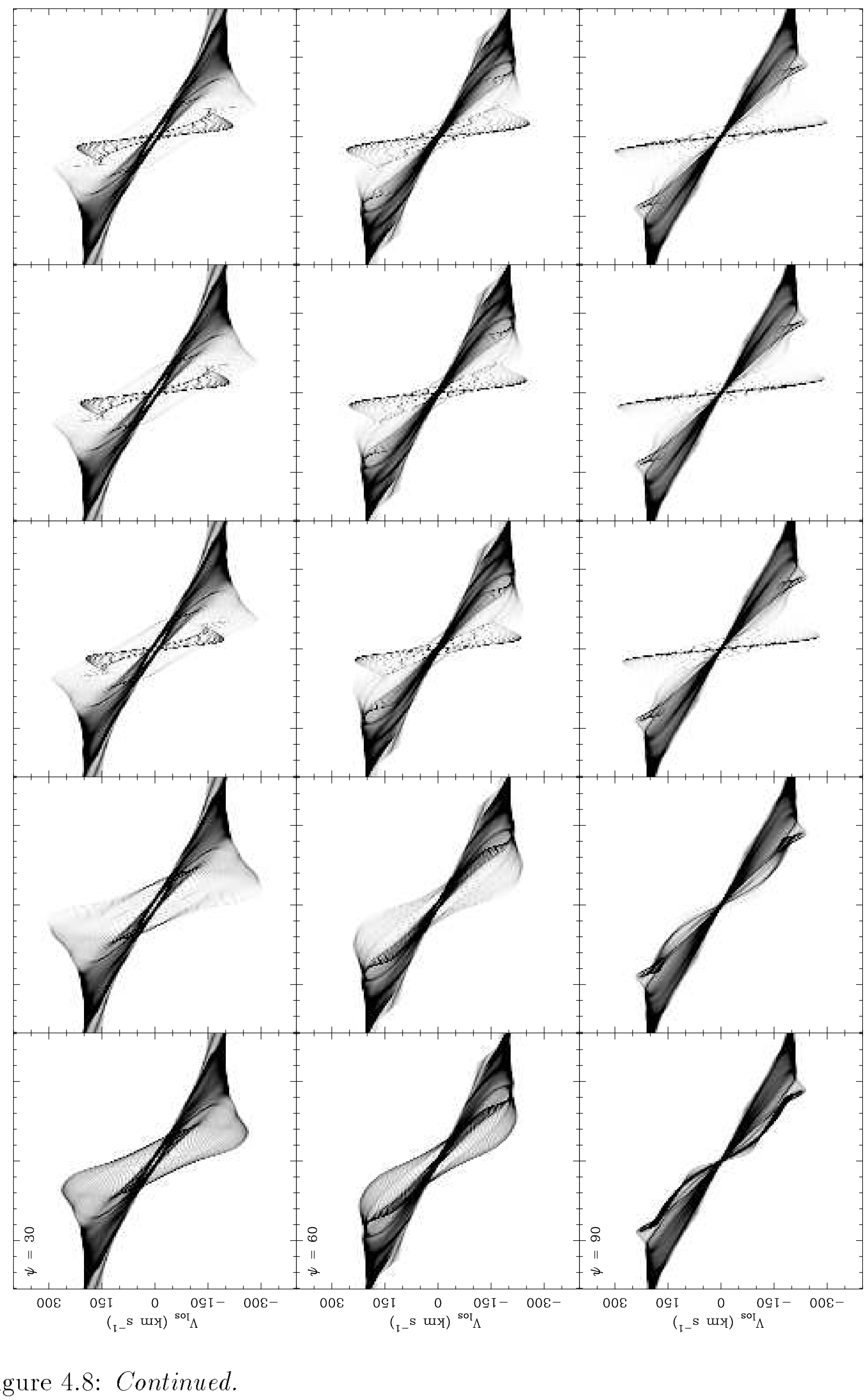

Figure 4.8: *Continued.*

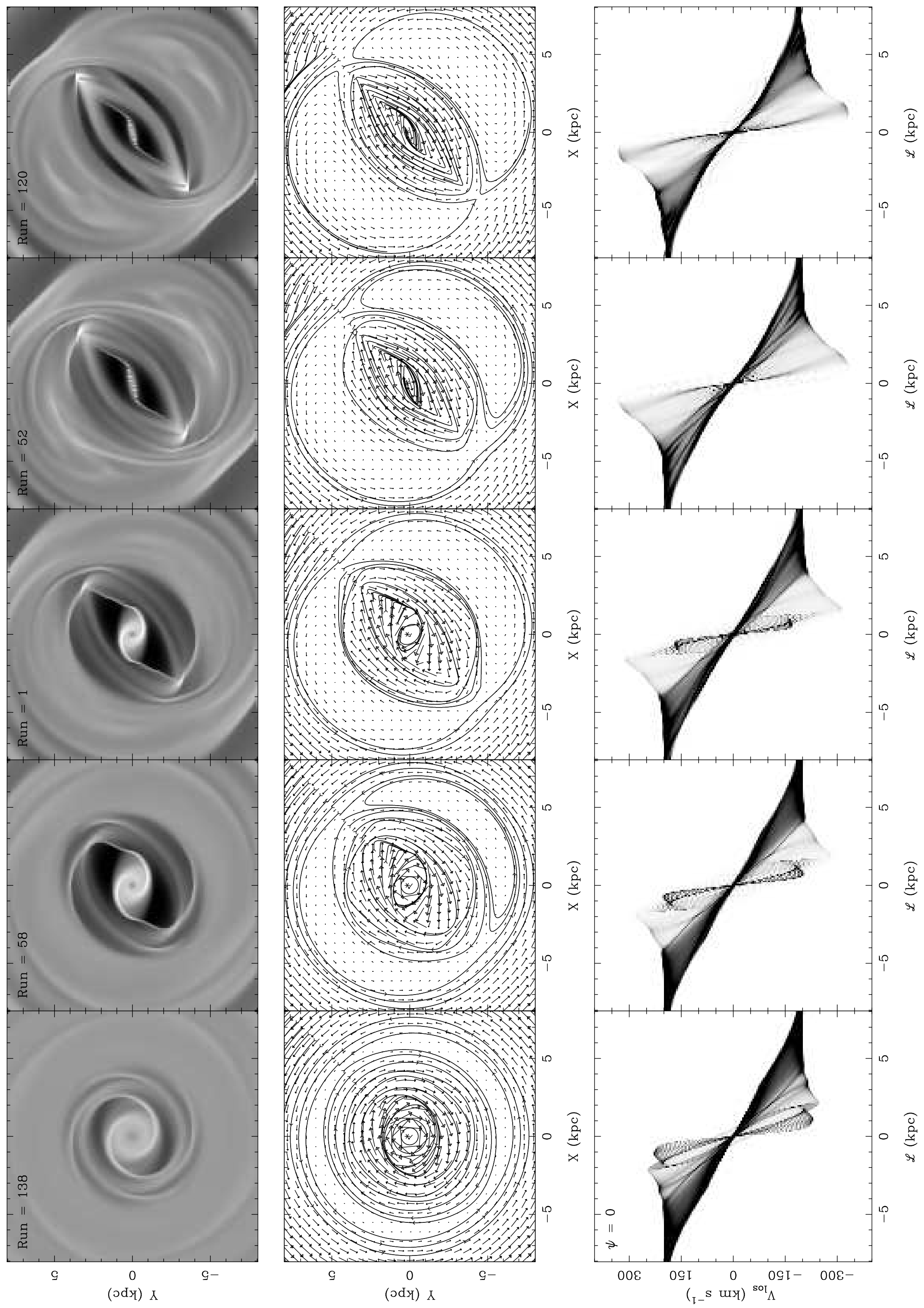

Figure 4.9: Same as Figure 4.6 but for a sequence of models of increasing bar quadrupole moment Q_m. The models are 138, 058, 001, 052, and 120, with, respectively, $Q_m = 0.5 \times 10^4$, 2.5×10^4, 4.5×10^4, 6.0×10^4, and 8.0×10^4. The other parameters of the models are kept fixed at those of model 001.

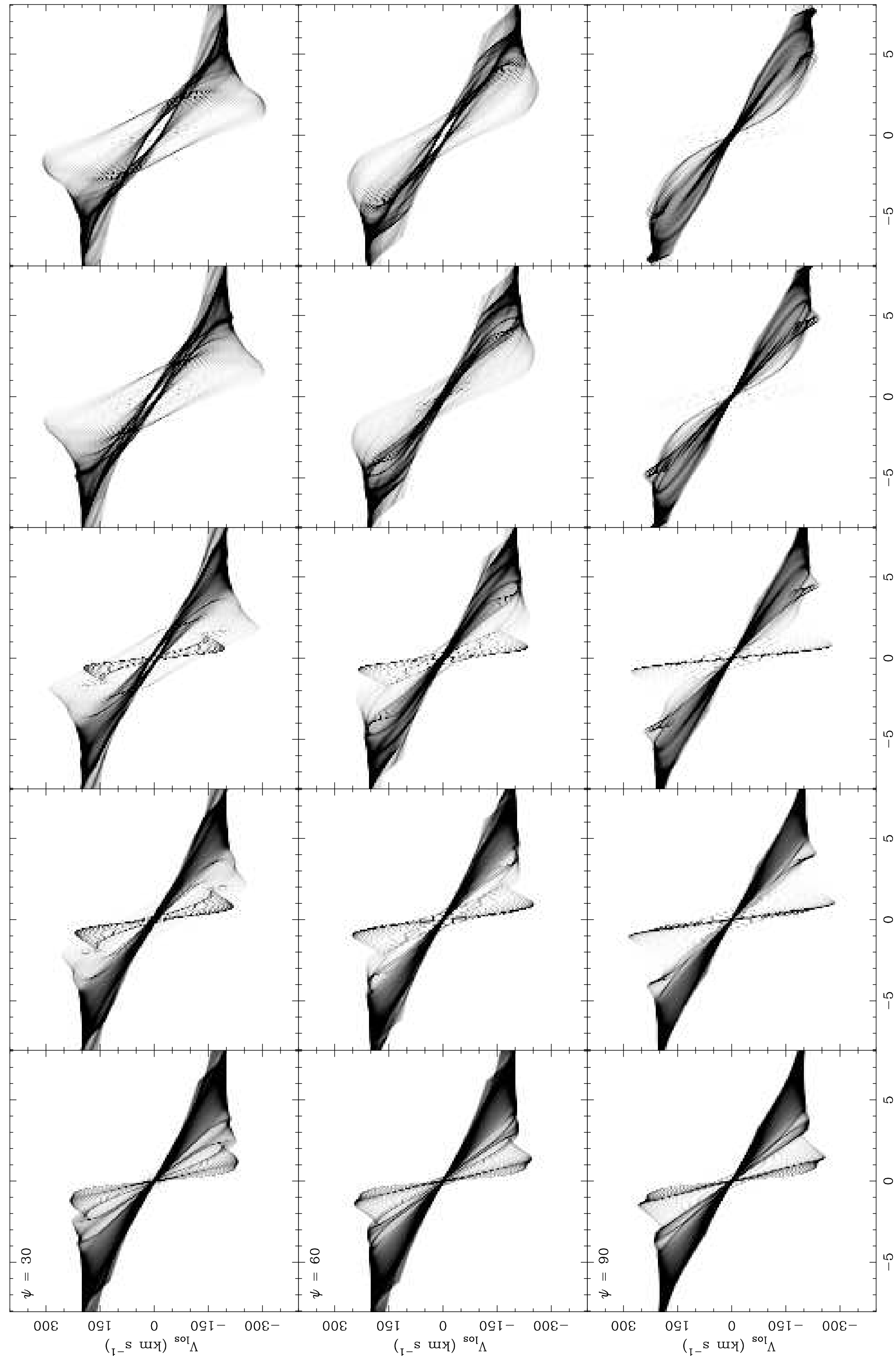

Figure 4.9: *Continued.*

the bar is seen end-on and smaller velocities when it is seen side-on. The most important effect of an increase of the axial ratio of the bar is the disappearance of the nuclear spiral for axial ratios $a/b \gtrsim 2.7$. Because the nuclear spiral is associated with an x_2-like flow, and because the range of radii occupied by the x_2 orbits decreases rapidly as the bar axial ratio is increased (see Fig. 6 of A92a), the nuclear spiral and its associated inverted S-shaped signature in the PVDs disappear for large bar axial ratios. The maximum radial velocity reached by the signature of the nuclear spiral varies little with the bar axial ratio (when present).

Figure 4.7 shows how the gas density and kinematics change when the Lagrangian radius of the mass model is varied. Model 029 is probably unphysical, as the corotation radius (which is almost equal to the Lagrangian radius) would be within the bar. This is very unlikely to happen in a real galaxy, as there would be no x_1 periodic orbits at the end of the bar to support it self-consistently (see, e.g., Contopoulos 1980). A92b showed that the shock loci within the bar are offset toward its leading sides and of the form observed in early-type barred spiral galaxies only for a restricted range of Lagrangian radii, namely $r_L = (1.2 \pm 0.2)a$. All the observational estimates for strongly barred early-type spirals also give values in that range (see, e.g., A92b; Elmegreen 1996). We will thus concentrate on those Lagrangian radii here. Model 028, the limiting case with $r_L = 5.0$, shows strong spiral arms starting at the end of the bar and extending to large radii. The spiral arms are easily identified in the PVDs as long filamentary structures. This model has no nuclear spiral, and thus no corresponding inverted S-shaped feature in the PVDs. This is not the case for models with lower pattern speeds, or, equivalently, larger Lagrangian radii. Those models have extended x_2 periodic orbit families and therefore nuclear spirals (see A92b). As the pattern speed of the bar is decreased, the radial range occupied by the x_2 periodic orbits is increased (A92a), and the nuclear spiral becomes more predominant. The main and outer bar regions decrease accordingly. This effect is clearly seen in the PVDs of Figure 4.7. For increasing Lagrangian radii, they show an increase of the radial extent of the nuclear spiral signature, and a decrease of the radial extent of the signature of main and outer bar regions. There is also an increase of the maximum radial velocity of the x_2 feature, but the effect is rather small.

Figure 4.8 shows the behaviour of the gas as the central concentration of the mass model is varied. For low central concentrations, the gas streamlines are oval and aligned with the bar, there are no shocks, and the barred region is only slightly gas depleted. The signature of the main and outer bar regions in the PVDs is then clear. As the central concentration is increased, the streamlines become more eccentric, and the envelope of the signature of the main and outer bar regions extends further to high velocities. Once the central concentration reaches $\rho_c \approx 2.2 \times 10^4$, an x_2-like flow appears in the center of the bar and a nuclear spiral and offset shocks are formed. These changes are also easily seen in the

PVDs, which acquire an inverted S-shaped feature, while the density in the main and outer bar regions drops. The region occupied by the x_2 orbits then increases with increasing central concentration (A92a), and so does the radial extent of the nuclear spiral signature in the PVDs. An increase in the central concentration of the mass model has similar effects to an increase of the Lagrangian radius (see Fig. 4.7). This is not surprising, since both changes influence the location of the resonances similarly.

Figure 4.9 shows a sequence of simulations with different values of the bar quadrupole moment. For the lowest quadrupole moment, the bar is weak and the flow is close to circular, with only a weak spiral shock in the center. This does no cause substantial inflow, and the gas density in the main and outer bar regions is relatively high. The velocity field shows that there is a transition from a x_1-like flow to a x_2-like flow in the central region, but the effect is not strong since the eccentricity of the streamlines is weak. All these effects reflect themselves in the PVDs. For somewhat higher bar quadrupole moments, the nuclear spiral is well-developed and its signature strong in the PVDs, with a gap present between it and the solid-body signature of the outer parts of the galaxy. As the bar quadrupole moment is increased further, the envelope of the signature of the main and outer bar regions in the PVDs becomes more extreme, reaching higher maximum velocities and extending closer to the center. For $Q_m \gtrsim 5.5 \times 10^4$, the nuclear spiral disappears. Those two effects are due to the fact that the eccentricity of the streamlines increases significantly with increasing bar quadrupole moment, while the region occupied by the x_2 orbits decreases until it disappears completely (see A92a). Because the bar is so strong for high quadrupole moments, the flow is non-circular even in the outer parts of the simulations, and a "hole" is present in the center of the PVDs at intermediate viewing angles. Not surprisingly, the variations in the gas distribution and kinematics are similar when the bar quadrupole moment is increased and when the axial ratio of the bar is increased.

4.4 Dust Extinction

It is interesting to note that the PVDs discussed so far have a limited degree of symmetry with respect to the viewing angles $0°$ and $90°$. This means that although it is relatively easy to determine whether a line-of-sight is close to the major or minor axis of a bar ($|\psi|$), it is considerably harder to determine in which half of the PVD (positive or negative projected distances from the center) the near side of the bar is located ($\pm\psi$).

This situation can be contrasted to that in the Galaxy, where most studies have no difficulty identifying the quadrant in which the near side of the Galactic bar is located. Studies using infrared photometry (e.g. Dwek et al. 1995; Binney, Gerhard, & Spergel 1997), star counts (e.g. Weinberg 1992; Stanek et al. 1997), gaseous or stellar kinematics (e.g. Binney et al. 1991; Wada et al. 1994; Zhao, Spergel, & Rich 1994; see also Beaulieu 1996; Sevenster et al. 1997), and microlensing events (e.g. Paczynski et al. 1994) all indicate a bar making an angle of 15° to 45° with respect to the line-of-sight to the Galactic center (positive values indicating that the near side of the bar is at positive Galactic longitude). In the case of the Galaxy, at least two effects help the observer determine the exact orientation of the bar. Firstly, projection effects (both in longitude and latitude) mean two lines-of-sight on each side of the Galactic center reach correspondingly different parts of the bar (e.g. Binney et al. 1991). Secondly, the large difference between the distances to each side of the bar means point sources in the far side of the bar will appear significantly fainter than corresponding sources in the near side (e.g. Stanek et al. 1997). In addition, the far side of the bar will appear thinner than the near side (e.g. Dwek et al. 1995). For a distant galaxy, no such projection effects are present. However, extinction within an edge-on disk can play a similar role to that of distance in the Galaxy, and can help to constrain the orientation of a bar. If dust is present in significant amount, the spectroscopic signature of the far side of the bar in the PVDs should be fainter than that of the nearer side.

Figure 4.10 shows the surface density and PVDs of model 001 when considering a dust distribution proportional to the surface density of the gas (we take a constant absorption coefficient per unit mass κ; $\kappa = 0.1$ for Fig. 4.10). To illustrate the effects of the dust, we have decreased the surface densities in the surface density plot of Figure 4.10 to reflect the effective contribution of each point to the projected density at a viewing angle $\psi = 45°$. Unlike Figure 4.1, the PVDs are now far from symmetric with respect to the viewing angles $\psi = 0°$ and 90°. In addition, individual PVDs are no longer antisymmetric with respect to the center. This is mainly because the nuclear spiral obscures most of the material behind it, breaking the symmetry of the parallelogram-shaped signature of the x_1-like flow in the main and outer bar regions. For viewing angles $0° \lesssim \psi \lesssim 90°$, the nuclear spiral obscures mostly material moving away from the observer in the outer bar region, and obscures only a small amount of material moving toward the observer in the same region. Thus, the signature of the x_1-like flow in the PVDs is weakened for positive radial velocities, leading to a much fainter signature of the main and outer bar regions in the upper halves of the PVDs than in the lower halves. The opposite is true for viewing angles $90° \lesssim \psi \lesssim 180°$, where the signature of the main and outer bar regions is now much fainter in the lower halves. This effect is strongest and least extended for viewing angles of about 110° to 150°, as the line-of-sight is then parallel or at a small angle to the major axis of the nuclear spiral (which is slightly offset from that of the x_2 periodic orbits). Some effects

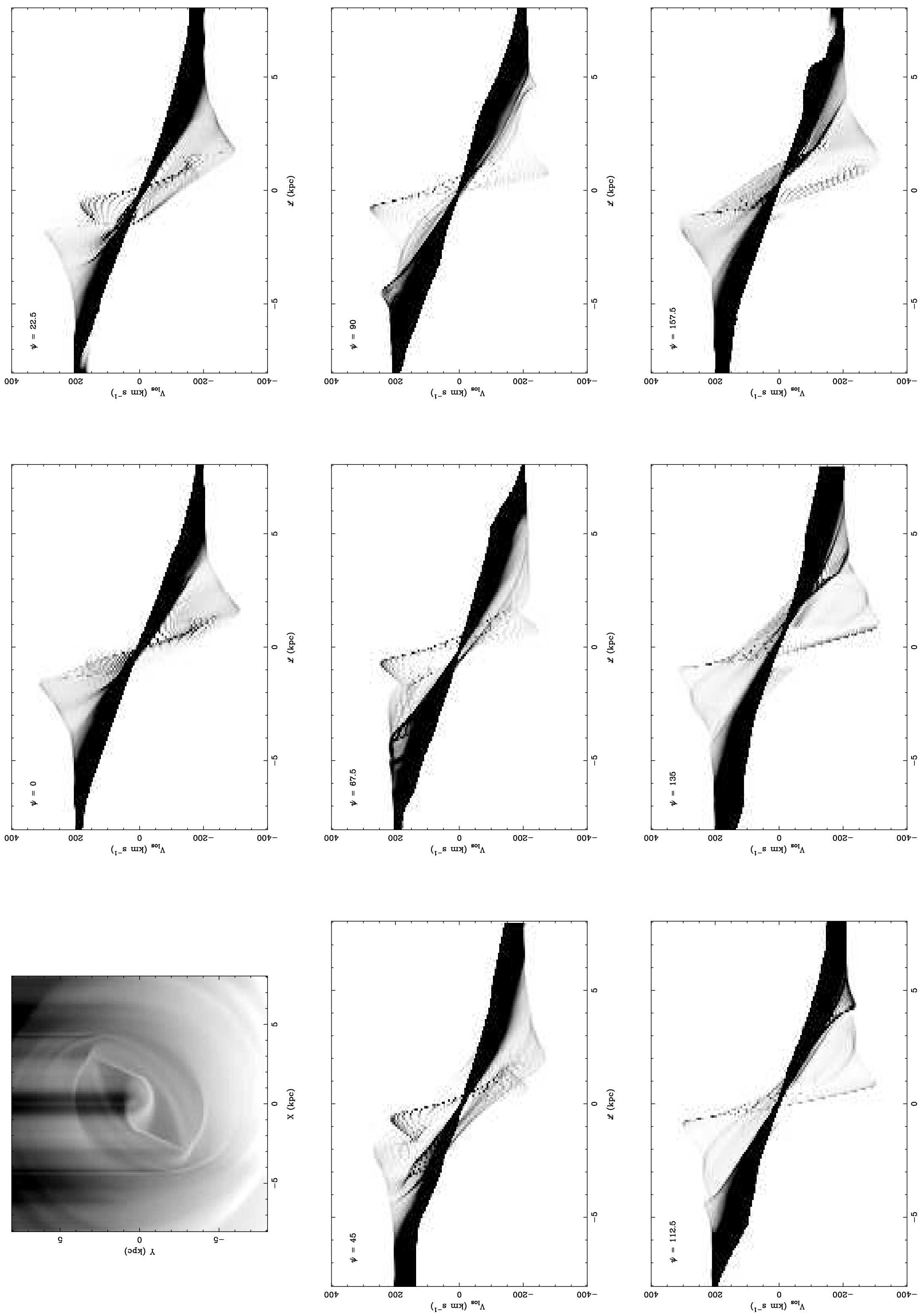

Figure 4.10: Same as Figure 4.1 but considering a dust distribution proportional to the gas surface density. The surface densities in the top-left plot have been decreased to reflect the effective contribution of each point to the integrated density along the line-of-sight for a viewing angle $\psi = 45°$. New features in the PVD for $\psi = 45°$ can thus be directly related to new features in the surface density plot.

on the signature of the nuclear spiral itself and on the signature of the outer parts of the simulation are present, but they are less pronounced.

In addition to the diagnostics suggested in the previous sections to identify a bar in an edge-on spiral galaxy, and determine whether it is seen end-on or side-on, the introduction of dust in the models has allowed us to develop criteria to determine in which half of the galaxy the near side of the bar is located. Of course, the distribution of dust in real galaxies will inevitably be more complex than the highly idealised distribution adopted here. Nevertheless, the features due to dust in the PVDs of Figure 4.10 can probably still be used as a guide to interpret asymmetries present in real data.

4.5 Discussion

Unlike periodic orbits studies (Kuijken & Merrifield 1995; Ch. 3), where one has to adopt a way of populating the orbits, hydrodynamical simulations provide both the density and the velocity of the gas. Furthermore, if some periodic orbit families intersect, it is not necessary to make a choice between them, since the simulations will reveal which family the gas follows in each region. Nevertheless, as we will discuss later in this section, the comparison with observations can still present some problems, since observations involve the strength of a given emission line rather than the gas density. Hydrodynamical simulations also make a number of approximations about the properties of the interstellar medium (ISM), and these may limit the applicability of the simulations to the interpretation of real data. We discuss such limitations for our simulations later on in this section as well.

Notwithstanding the problem of populating the orbits, there is generally a good agreement between the PVDs obtained from the periodic orbits approach in Chapter 3 and those obtained here from hydrodynamical simulations. This is because there are several similarities between the periodic orbits structure of the models and the gas flow (see A92b). We have in both cases a central component in the PVDs, which we identified in Chapter 3 with the x_2 orbits and in this chapter with the nuclear spiral. Further out, we have the domain of the x_1 orbits, which covers the main and outer regions of the bar in the simulations. In Chapter 3, by studying in detail the signatures of various periodic orbit families in the PVDs, we gained useful insight into the structure and kinematics of the gas from first principles. This allowed us to obtain a deeper understanding of the PVDs produced in the hydrodynamical simulations.

The main feature of the PVDs is the gap (fainter region), present at all viewing angles, between the signature of the nuclear spiral and that of the outer parts of the simulations. Such a structure would not be possible in an axisymmetric galaxy and it can unmistakably reveal the presence of a bar or oval in an edge-on disk. This gap occurs because of the large-scale shocks which develop in the bar, driving an inflow of gas toward the center, and depleting the main and outer bar regions.

The gaps present in the PVDs produced with periodic orbits (see Kuijken & Merrifield 1995; Ch. 3) are different in nature from the ones observed here, being mainly due to the absence of populated orbits in certain regions of the models, particularly around corotation. As a result, the low density region extends well beyond corotation in these studies, although the exact extent depends on which orbits are neglected (e.g. as self-intersecting) and how the other orbits are populated. For example, in Figure 1 of Kuijken & Merrifield (1995), the gap extends to almost twice the corotation radius. We recall that three-dimensional N-body simulations of rotating disks produce bars which, when viewed edge-on, appear boxy-shaped if seen end-on and peanut-shaped if seen side-on (see, e.g., Combes & Sanders 1981; Combes et al. 1990; Raha et al. 1991). Taking the maximum height of the boxy/peanut-shaped bars to occur at half the corotation radius (Combes et al. 1990), we find that, in Kuijken & Merrifield's (1995) case, the ratio of the radial extent of the low density region of the PVDs to the radius where the maximum height of the peanut-shaped bulges occurs should be approximately 4 (associating the bulges with edge-on bars). On the other hand, in the hydrodynamical simulations presented here, the low density region of the PVDs reflects the low density region in the main and outer bar regions, and should thus be within corotation. When a bar is seen side-on, the ratio of the extent of the low density region to the radius of maximum height of the peanut-shaped bulge should thus be approximately 2. Kuijken & Merrifield (1995) report that this ratio is about 2 for the two galaxies they studied, in agreement with the prediction of our hydrodynamical simulations. These results can only be reconciled with the periodic orbits approach if the maximum height of the peanut-shaped bulges occurs near corotation (rather than halfway).

As we pointed out in § 4.3.2, the shape of the features present in the PVDs varies with the viewing angle, and can thus in principle be used to constrain the viewing angle to the bar in an observed galaxy. The envelope of the signature of the main and outer bar regions in the PVDs reaches very high radial velocities (compared to the outer parts of a simulation) for viewing angles close to the bar and relatively low velocities for viewing angles perpendicular to it. However, the envelope is so faint in most cases that it is unlikely to be of much use with real data (see § 4.3.4). The signature of the nuclear spiral has an inverted S-shape for $0^\circ \lesssim \psi \lesssim 90^\circ$ and is almost solid-body for $90^\circ \lesssim \psi \lesssim 180^\circ$. That feature is rather thick and does not show much fine structure, however, so it may be hard to use in conjunction with observations. The best viewing angle diagnostic is probably provided by the ratio of the maximum radial velocity reached by the nuclear spiral component and the velocity in the outer parts of a galaxy. This ratio should be greater than unity for viewing angles perpendicular to the bar and smaller than unity for viewing angles parallel to it. Other properties of a PVD, such as the faintness of the signature of the main and outer bar regions, can also help to constrain the mass distribution and bar properties of an observed galaxy (see § 4.3.4). In practice, however, the analysis and modelling of spectroscopic data should not be a trivial task.

If a barred system has no nuclear spiral (or, equivalently, does not have an extended x_2 family of periodic orbits), there will not be a nuclear spiral component in the PVDs and no gap or double-peaked structure. An example of such a model was discussed in § 4.3.3. The only component likely to be detected observationally is then the solid-body signature of the outer parts of the galaxy. Thus, the kinematical detection of the presence of a bar is not straightforward. The first step would be to rule out such a slowly rising rotation curve (the rotation curve being defined as the upper limit of the envelope of an observed PVD), for example by calculating the shape of the rotation curve expected from the surface photometry. However, this would only show that the type of gas observed (ionised, H I, or molecular) is not present in sufficient quantities in the central region of the galaxy, but it would not provide any information on the cause of this depletion. It is thus probably necessary to use stellar kinematics to identify the bar in such systems. Because a large percentage of the stars in the central regions of barred disks are trapped around the x_1 orbits, there should be a clear bar signature in the stellar PVDs. We shall discuss the stellar kinematics and corresponding PVDs in Paper III. Let us note, however, that cases with no nuclear spiral component should be a minority, at least among strongly barred early-type spiral galaxies, since observational evidence argue that these systems possess ILRs (see, e.g., Athanassoula 1991; A92b). In particular, the fact that the dust lanes in most early-type strongly barred galaxies are offset along the leading sides of the bar, rather than centered and close to its major axis, is a strong argument for the existence of ILRs (A92b). Nevertheless, the existence of ILRs deserves further study, particularly for later type spirals. This can be done, for example, either by high resolution kinematical studies, to show the change of direction of the orbits or streamline ellipticities in the central parts of galaxies (e.g. Teuben et al. 1986), or by calculating the families of periodic orbits in galaxy potentials derived from observations, to show the existence or non-existence of the x_2 (and x_3) family.

Although our simulations cover a fair fraction of the available parameter space (see Table 1 in A92a), we have never come across a PVD showing a clear "figure-of-eight", as suggested by Kuijken & Merrifield (1995). In other words, the upper envelope of the low density region of the simulated PVDs is never as pronounced as it is in NGC 5746 or, to a lesser extent, in NGC 5965 and NGC 6722 (see Kuijken & Merrifield 1995; Fig. 5.1). By plotting the hydrodynamical PVDs with a logarithmic scale, or different grayscale levels, it is possible to show that, in some cases, the upper envelope of the signature of the main and outer bar regions has a higher density than the rest of the signature at lower radial velocities. The effect, however, is never as strong as it is in NGC 5746. This feature thus needs further study. Somehow, these galaxies must be able to accumulate material at the ends of the bar on its *minor* axis. We note, however, that this feature is unusual. It is not present in most of the edge-on barred spiral galaxies identified in Chapter 5 (see Fig. 5.1).

Contrary to the "building blocks" approach of Chapter 3, which used combinations of periodic orbit families to model the structure and kinematics of barred galaxies, the hydrodynamical simulations presented here inherently take into account the collisional nature of gas, so the kinematics of the gaseous component of barred spirals is more accurately modelled. Approximations to the gas properties are nevertheless necessary, and we recall that the gas was treated as ideal, isothermal, infinitely thin, and non-self-gravitating. How much do our results depend on these assumptions, or, in other words, how model dependent are they?

The interstellar medium is a complicated multi-phase mixture, which can only be described schematically, particularly in non-local studies covering an object the size of a galaxy. Two different approaches have been developed so far. In the first one, the gas is treated as ballistic particles which, when they collide, loose energy according to pre-specified recipes (e.g. Miller, Prendergast, & Quirk 1970; Schwarz 1981, 1984; Combes & Gerin 1985). Unfortunately, the results of these simulations can depend on the adopted collision law (Guivarch & Athanassoula, in preparation), at least as far as the shocks in a barred region are concerned. The second approach is hydrodynamical, solving the Euler equations either with the help of a grid (e.g. van Albada & Roberts 1981; van Albada, van Leer, & Roberts 1982; Mulder 1986; Piner, Stone, & Teuben 1995), Smooth Particles Hydrodynamics (Lucy 1977; Gingold & Monaghan 1977; Hernquist & Katz 1989), or beams (Sanders & Prendergast 1974). A number of these studies assume an isothermal equation of state, following the model of Cowie (1980). He calculated the equation of state for an ensemble of clouds and found that it could be described as isothermal, provided the clouds have an equilibrium mass spectrum.

Comparing the results of all these schemes is beyond the scope of this paper. In all the approaches, the more reliable codes produce shocks in barred regions. Those shocks result in an inflow of gas and a substantial lowering of the density in the main and outer bar regions. However, the location, shape, and persistence of the shocks differ. Our main justification for adopting the present hydrodynamical code is that it gave good results in many previous studies (see A92b).

Since dissipation ensures that the gas layer in spiral galaxies remains thin, the two-dimensional nature of the simulations should not be a factor limiting the applicability of the results to the interpretation of real data. A further question concerns the effect of self-gravity. Because our mass model represents best early-type barred spirals (see A92a), where the fraction of the total mass in gas is typically less than 10%, the contribution of the gas to the potential and large scale forces of real systems would be small. Lindblad, Lindblad, & Athanassoula (1996) found that including self-gravity in their model of NGC 1365 made very little difference to the global picture. It may well be, however, that locally, and in particular near high density structures such as the nuclear spiral, the self-gravity of the gas plays a role. This question should be explored in future work.

When using the bar diagnostics developed to interpret observational data, one has to take into account the fact that the PVDs were calculated using the gas *density* in the simulations and not the strength of a given gaseous emission line, which is what one usually observes. Physical conditions in the gas vary across the simulated disks, and will lead to different excitation mechanisms dominating in different parts of the disks. Regions of high density and low shear, such as the area around corotation, are likely to have higher star formation rates and thus more photoionised gas than elsewhere. Conversely, the gas in or near shocks, such as the nuclear spiral, will be mainly shock-excited (see Binette, Dopita, & Tuohy 1985; Dopita & Sutherland 1996), with possible star formation depending on the shear. Because different excitation mechanisms lead to different emission line ratios, the relative amplitudes of the various components of a PVD (e.g. the intensity of the signature of the outer parts of the disk versus that of the nuclear spiral) will depend on the emission line used in the observations. For example, we show in Chapter 5 that, for many objects, the signature of the nuclear spiral is very strong in the [N II] λ6548,6584 lines but is almost absent in the Hα line, probably indicating that it is shock-excited (the other components of the PVDs show [N II] λ6584/Hα ratios typical of H II regions). The PVDs were not corrected for stellar absorption, however, so these results should be interpreted with caution. Nevertheless, our PVDs should only be as guide when interpreting kinematical data. We stress that the morphology of the PVDs (the multiple components) is a more significant bar diagnostic than the distribution of intensity (the relative amplitudes of the components).

Similarly, under certain assumptions about the physical conditions in the gas, it is possible to use observed emission line ratios (e.g. Hα/Hβ) to measure the extinction due to dust. This could prove useful to interpret asymmetries in observed PVDs (see § 4.4 for a more complete discussion of likely dust effects).

4.6 Summary and Conclusions

Our main aim in this chapter, similarly to Chapter 3, was to develop diagnostics to identify bars in edge-on spiral galaxies, using the particular kinematics of the gaseous component of barred disks. To achieve this goal, we ran two-dimensional hydrodynamical simulations of the gas flow in the potential of a barred spiral galaxy mass model including a Ferrers bar, neglecting the self-gravity of the gas. We constructed position-velocity diagrams (PVDs) from those simulations using an edge-on projection and various viewing angles with respect to the major axis of the bar. The presence of shocks and inflows in the simulations allowed us to develop better bar diagnostics than those presented in Chapter 3.

We analysed in detail two simulations which are prototypes of simulations for models with and without inner Lindblad resonances (which we associate with the existence of x_2 periodic orbits). We showed that, for models allowing x_2 orbits, the nuclear spiral which is present in the center of the simulations produces a strong inverted S-shaped signature in the PVDs. This signature reaches high radial velocities (compared to those in the outer parts of the simulations) when the bar is seen side-on and relatively low velocities when the bar is seen end-on. The flow in the main and outer bar regions (the entire bar region if no nuclear spiral is present) produces a parallelogram-shaped signature in the PVDs, being associated with the x_1 periodic orbits. Because the flow is mostly parallel to the bar in that region, the highest velocities are now reached for viewing angles close to the bar major axis. In the outer parts of the simulations, the flow is almost circular and produces a strong almost solid-body signature in the PVDs for all viewing angles.

Shocks within the bar are present in most simulations and lead to a depletion of the gas in the region of the bar occupied by the x_1-like flow. Thus, if a nuclear spiral is present, a bar can easily be identified in an edge-on spiral galaxy, as there will be a gap in the PVD between the signature of the nuclear spiral and that of the outer parts of the galaxy. If there is no nuclear spiral, it may still be possible to detect a bar with the help of photometry and/or stellar kinematics. The envelope of the signature of the nuclear spiral, and to a lesser extent that of the main and outer bar regions, is most useful to determine the orientation of a bar with respect to the line-of-sight. Nevertheless, it is hard to discriminate between two viewing angles on either side of the bar. We showed that adding dust to the simulations helps break this degeneracy.

We also produced PVDs for a range of simulations covering most of the fraction of parameter space likely to be occupied by strongly barred early-type spiral galaxies. These simulations can be used to constrain the mass distribution and bar properties of an observed system. In particular, the presence or absence of the signature of a nuclear spiral in a PVD places strong constraints on the values our mass model parameters may take. The nuclear spiral can be absent for high bar axial ratios and/or bar quadrupole moments, and for low Lagrangian radii and/or central concentrations.

References

Athanassoula, E. 1991, in Dynamics of Disk Galaxies, ed. B. Sundelius (CTH: Göteborg), 149

———. 1992a, MNRAS, 259, 328 (A92a)

———. 1992b, MNRAS, 259, 345 (A92b)

Athanassoula, E., Bienayme, O., Martinet, L., & Pfenniger, D. 1983, A&A, 127, 349

Athanassoula, E., & Bureau, M. 1999, in preparation. (Paper III)

Beaulieu, S. F. 1996, Ph. D. Thesis, The Australian National University

Binette, L., Dopita, M. A., & Tuohy, I. R. 1985, ApJ, 297, 476

Binney, J., Gerhard, O., & Spergel, D. 1997, MNRAS, 288, 365

Binney, J., Gerhard, O. E., Stark, A. A., Bally, J., & Uchida, K. I. 1991, MNRAS, 252, 210

Combes, F., & Gerin, F. 1985, A&A, 150, 327

Combes, F., & Sanders, R. H. 1981, A&A, 96, 164

Combes, F., Debbasch, F., Friedli, D., & Sanders, R. H. 1990, A&A, 233, 82

Contopoulos, G. 1980, A&A, 81, 198

Contopoulos, G., & Papayannopoulos, T. 1980, A&A, 92, 33

Cowie, L. L. 1980, ApJ, 236, 868

de Carvalho, R. R., & da Costa, L. N. 1987, A&A, 171, 66

Dopita, M. A., & Sutherland, R. S. 1996, ApJS, 102, 161

Dwek et al. 1995, ApJ, 445, 716

Elmegreen, B. 1996, in Barred Galaxies, ed. R. Buta, D. A. Crocker, and B. G. Elmegreen (ASP: San Francisco), 197

Ferrers, N. M. 1877, Q.J. Pure Appl. Math., 14, 1

Gingold, R. A., & Monaghan, J. J. 1977, MNRAS, 181, 375

Hamabe, M., & Wakamatsu, K. 1989, ApJ, 339, 783

Hernquist, L., & Katz, N. 1988, ApJ, 349, 562

Kuijken, K., & Merrifield, M. R. 1995, ApJ, 443, L13

Kuzmin, G. 1956, AZh, 33, 27

Lindblad, P. A. B., Lindblad, P. O., & Athanassoula, E. 1996, A&A, 313, 65

Lucy, L. B. 1977, AJ, 82, 1013

Merrifield, M. R. 1996, in Barred Galaxies, ed. R. Buta, D. A. Crocker, and B. G. Elmegreen (ASP: San Francisco), 179

Miller, R. H., Prendergast, K. H., Quirk, W. J. 1970, ApJ, 161, 903

Mulder, W. A. 1986, A&A, 156, 354

Paczynski, B., Stanek, K. Z., Udalski, A., Szymanski, M., Kaluzny, J., Kubiak, M., Mateo, M., & Krzeminski, W. 1994, ApJ, 435, L113

Papayannopoulos, T., & Petrou, M. 1983, A&A, 119, 21

Piner, B. G., Stone, J. M., Teuben, P. J. 1995, ApJ, 449, 508

Raha, N., Sellwood, J. A., James, R. A., & Kahn, F. D. 1991, Nature, 352, 411

Sandage, A. 1961, The Hubble Atlas of Galaxies (Washington: Carnegie Institution)

Sanders, R. H., & Huntley, J. M. 1976, ApJ, 209, 53

Sanders, R. H., & Prendergast K. H. 1974, ApJ, 188, 489

Schwarz, M. P. 1981, ApJ, 247, 77

———. 1984, MNRAS, 209, 93

Sellwood, J. A. 1981, A&A, 99, 362

Sellwood, J. A., & Wilkinson, A. 1993, Re. Prog. Phys., 56, 173

Sevenster, M., Saha, P., Valls-Gabaud, D., & Fux, R. 1997, MNRAS, submitted.

Stanek, K. Z., Udalski, A., Szymanski, M., Kaluzny, J., Kubiak, M., Mateo, M., & Krzeminski, W. 1997, ApJ, 477, 163

Teuben, P., & Sanders, R. H. 1985, MNRAS, 201, 303

Teuben, P. J., Sanders, R. H., Atherton, P. D., & van Albada G. D. 1986, MNRAS, 221, 1

Toomre, A. 1963, ApJ, 138, 385

van Albada, G. D. 1985, A&A, 142, 491

van Albada, G. D., & Roberts, W. W. 1981, ApJ, 246, 740

van Albada, G. D., van Leer, B., & Roberts, W. W. 1982, A&A, 108, 76

Wada, K., Taniguchi, Y., Habe, A., & Hasegawa, T. 1994, ApJ, 437, L123

Weinberg, M. D. 1992, ApJ, 384, 81

Zao, H. S., Spergel, D. N., & Rich, R. M. 1994, AJ, 108, 2154

Chapter 5

The Nature of Boxy/Peanut-Shaped Bulges in Spiral Galaxies

Abstract

We present a systematic observational study of the relationship between bars and boxy/peanut-shaped (B/PS) bulges in spiral galaxies. We first review and discuss proposed mechanisms for the formation of B/PS bulges, focussing on accretion and bar-buckling scenarios. Using new methods relying on the kinematics of edge-on disks, we look for bars in a large sample of edge-on spiral galaxies with B/PS bulges and in a smaller control sample of edge-on spirals with more spheroidal bulges. We present position-velocity diagrams of the ionised gas obtained from optical long-slit spectroscopy. We show that almost all B/PS bulges are due to a thick bar viewed edge-on, while only a few extreme cases are likely due to the accretion of external material. This strongly supports the bar-buckling mechanism for the formation of B/PS bulges. None of the galaxies in the control sample shows evidence for a bar, which suggests conversely that bars are generally B/PS.

We consider the effects of dust in the disk of the galaxies, but conclude that it does not significantly affect our results. Unusual emission line ratios correlating with kinematical structures are observed in many objects, and we argue that this is consistent with the presence of strong bars in the disk of the galaxies. More work is required to determine the orientation of the bars in B/PS bulges.

The reliable identification of bars in edge-on spiral galaxies opens up for the first time the possibility of studying observationally the vertical structure of bars.

5.1 Introduction

Many spiral galaxies display boxy or peanut-shaped bulges when viewed edge-on. Statistical studies of the incidence of these objects have not used objective criteria to quantify the boxiness of the bulges. They are therefore hard to compare and yield moderately different results. Nevertheless, it seems clear that at least 20–30% of edge-on spirals possess a boxy/peanut-shaped (B/PS) bulge (see Jarvis 1986; Shaw 1987; de Souza & dos Anjos 1987). Spiral galaxies with B/PS bulges are therefore a significant class of objects.

The fact that the boxy/peanut shape is seen only in edge-on spirals indicates that the shape is related to the vertical distribution of the light. B/PS bulges have excess light above the plane at large galactocentric radii, compared to the usual $R^{1/4}$ law for the light distribution of spheroids (see Shaw 1993). Their three-dimensional light distribution must be even more extreme than the projected surface brightness (see, e.g., Binney & Petrou 1985 for axisymmetric models). In addition, B/PS bulges appear to rotate cylindrically, i.e. their rotation is independent of the height above the plane (e.g. Kormendy & Illingworth 1982; Rowley 1986).

Several models have been proposed to explain the structure of these bulges (e.g. Combes & Sanders 1981; May, van Albada, & Norman 1985; Binney & Petrou 1985). However, despite their prevalence and interesting structural and dynamical properties, they remain poorly studied observationally, probably because the edge-on projection makes the interpretation of observational data difficult.

In this chapter, we present new kinematical data for a large sample of spiral galaxies with a B/PS bulge. Our goal is to determine their three-dimensional structure and to identify their likely formation mechanism. We use our data to argue that B/PS bulges are simply bars viewed edge-on.

In § 5.2, we discuss the two main scenarios proposed for the formation of B/PS bulges – accretion of satellite galaxies and buckling of a bar. In § 5.3, we describe ways to discriminate between the two formation scenarios using kinematical data. The observations are presented in § 5.4 and the results discussed in § 5.5. We conclude in § 5.6.

5.2 Formation Mechanisms

5.2.1 Accretion

In early studies, the accretion of external material such as satellite galaxies was the favoured mechanism to explain the formation of B/PS bulges in spiral galaxies.

Binney & Petrou (1985) and Rowley (1986, 1988) showed that it is possible to construct axisymmetric cylindrically rotating B/PS bulges from relatively simple distribution functions. Binney & Petrou adopted a distribution function with a third integral of motion, in addition to the energy E and angular momentum along the symmetry axis L_z. This integral favoured orbits reaching a particular height above the plane. Rowley adopted a two-integral distribution function, with a truncation depending on both E and L_z. Both authors argued that the required distribution function could form naturally through the accretion of material onto a host spiral galaxy. Binney & Petrou (1985) additionally argued that, for the accreted material to form a B/PS bulge, the velocity dispersion of the accreted satellite must be much lower than the orbital speed, and the decay timescale must be much longer that the orbital time. This ensures that the accreted material stays clustered in phase space.

Accretion scenarios face several problems. At one extreme, one can consider the accretion of several small satellite galaxies. However, only a narrow range of orbital energy and angular momentum can lead to the formation of a B/PS bulge (Binney & Petrou 1985), so it is improbable that many satellite galaxies would all share these properties. Remaining satellites should then be present but they are not observed (Shaw 1987). The accretion of a single large companion is also ruled out by the large velocity dispersion and small decay timescale involved (Binney & Petrou 1985). Similarly, the merger of two spiral galaxies of similar sizes (or of a spiral and a small elliptical) seems an unlikely route to form B/PS bulges. This would require a fairly precise alignment of the spin and orbital angular momenta of the two galaxies. We recall that about a third of spiral galaxy bulges must be formed in this way (e.g. Shaw 1987).

From the arguments presented above, it seems that the accretion of a small number of moderate-sized satellites is the only accretion scenario which may lead to the formation of B/PS bulges. In favour of accretion is the fact that the best examples of B/PS bulges are found in small groups (e.g. NGC 128 and ESO 597-G 036), although we note that spirals with a B/PS bulge are not found preferentially in clusters (Shaw 1987). In addition, the possibly related X-shaped galaxies can form through the accretion of a satellite (e.g. Whitmore & Bell 1988; Hernquist & Quinn 1989). On the other hand, no evidence of accretion (arcs, shells, filaments, etc.) were detected by Shaw (1993) near spirals with a B/PS bulge, which argues against any kind of accretion. We are thus led to the conclusion that, while accretion of external material may play a role in the formation of some B/PS bulges, it is unlikely to be the primary formation mechanism.

5.2.2 Bar-Buckling

Bars can form naturally in N-body simulations of rotationally supported stellar disks (e.g. Sellwood 1981; Athanassoula & Sellwood 1986), due to global bisymmetric instabilities (e.g. Kalnajs 1971, 1977). Based on 3D N-body simulations, Combes & Sanders (1981) were the first to suggest that B/PS bulges could arise from the thickening of bars in the disks of spiral galaxies. Their results were confirmed and their suggestion supported by many later studies (see, e.g., Combes et al. 1990; Raha et al. 1991). Essentially, soon after a bar develops, it buckles, and settles with an increased thickness and vertical velocity dispersion, appearing boxy-shaped when seen end-on and peanut-shaped when seen side-on. The B/PS bulges thus formed are cylindrically rotating, as required.

Toomre (1966) first considered the buckling of disks, using idealised models, and found that if the vertical velocity dispersion in a disk is less than about a third of the velocity dispersion in the plane, the disk will be unstable to buckling modes (fire-hose or buckling instability; see also Fridman & Polyachenko 1984; Araki 1985). Bar formation in a disk makes the orbits within the bar more eccentric, without significantly affecting their perpendicular motions, thereby providing a natural mechanism for the bar to buckle. Resonances between the rotation of the bar and the vertical oscillations of the stars can also make the disk vertically unstable (see Pfenniger 1984; Combes et al. 1990; Pfenniger & Friedli 1991). The final shape of the bar is probably due to orbit trapping around the 2:2:1 periodic orbit family (see, e.g., Pfenniger & Friedli 1991).

Bar-buckling is the currently favoured mechanism for the formation of B/PS bulges. The fraction of edge-on spiral galaxies possessing a B/PS bulge is similar to the fraction of strongly barred spirals in face-on systems ($\approx 30\%$; e.g. Sellwood & Wilkinson 1993). In addition, bar-buckling provides a natural way to form B/PS bulges in isolated spiral galaxies, which accretion scenarios cannot do. We recall that spiral galaxies with a B/PS bulge are not found preferentially in clusters (Shaw 1987). We also note that, in a few cases, a bar can be directly associated with a B/PS bulge from morphological arguments (see, e.g., Bettoni & Galletta 1994 for NGC 4442).

The main observational problem faced by the bar-buckling mechanism is that B/PS bulges appear to be shorter (relative to the disk diameter) than real bars or strong bars formed in N-body simulations. However, this might simply be due to projection (a given surface brightness level is reached at a smaller radius in a more face-on disk) and no proper statistics have yet been compiled. The long term secular evolution of bars is also poorly understood. For example, it is known that bars can transfer angular momentum to a spheroidal component very efficiently (e.g. Sellwood 1980; Weinberg 1985). However, Debattista & Sellwood (1998) showed that, while the bar can be slowed down, it continues to grow and the boxy/peanut shape is preserved. It is less clear what happens if a bar is strongly perturbed. Norman, Sellwood, & Hasan (1996) also showed that if a bar is destroyed through the growth of a central mass concentration (e.g. Friedli & Benz 1993; Hasan & Norman 1990), the boxy/peanut shape is also destroyed.

The merits of the bar-buckling mechanism outweigh these potential problems, and the bar-buckling scenario remains largely unchallenged at the moment, despite very little direct observational confirmation (see, however, Kuijken & Merrifield 1995). The main aim of this chapter is to directly test this hypothesis by looking for bars in a large sample of spiral galaxies with a B/PS bulge.

Although it is not part of our program, the Milky Way is the first example of such a galaxy. The Galactic bulge is boxy-shaped (Weiland et al. 1994) and it is now well established that it is bar-like (e.g. Binney et al. 1991; Paczyński et al. 1994; see Kuijken 1996 for a brief review of the subject).

We note that "hybrid" scenarios have been proposed to explain the formation of B/PS bulges. An interaction or merger can excite (or accelerate) the development of a bar in a disk which is stable (or quasi-stable) against bar formation (e.g. Noguchi 1987; Gerin, Combes, & Athanassoula 1990; Miwa & Noguchi 1998). Bars formed this way are free to evolve to a boxy/peanut shape in the manner described above (see, e.g., Mihos et al. 1995), and the bulges thus formed owe as much to interaction as they do to the bar-buckling instability. However, the *shape* of the bulges is due to the buckling of the bars and interaction is merely a way to start the process of bar formation. In that sense, hybrid scenarios for the formation of B/PS bulges are really bar-buckling scenarios, and the possible accretion of material is unrelated to the shape of the bulges.

5.3 Observational Diagnostics

The main purpose of the observations presented in this chapter is to search for bars in the disks of spiral galaxies possessing a B/PS bulge. There is no straightforward photometric method to identify a bar in an edge-on spiral galaxy. The presence of a plateau in the major-axis light profile of the disk has been invoked as an indicator of the presence of a bar (e.g. de Carvalho & da Costa 1987; Hamabe & Wakamatsu 1989). However, axisymmetric features (e.g. a lens) can be mistaken for a bar and end-on bars may remain undetected. Kuijken & Merrifield (1995) were the first to demonstrate that bars could be identified kinematically in external edge-on spiral galaxies. They showed that the periodic orbits in a barred galaxy model produce characteristic double-peaked line-of-sight velocity distributions when viewed edge-on (see also Merrifield 1996). This gives long-slit spectra a spectacular "figure-of-eight" (or X-shaped) appearance, which they were able to observe in two systems with a B/PS bulge, namely NGC 5746 and NGC 5965 (see Fig. 5.1 for examples). Their approach is analogous to that used in the Galaxy with longitude-velocity diagrams (e.g. Peters 1975; Mulder & Liem 1986; Binney et al. 1991).

In Chapter 3, we refined the dynamical theory of Kuijken & Merrifield (1995). We used periodic orbit families in a barred galaxy model as building blocks to model the structure and kinematics of real galaxies. We showed that the global structure of a position-velocity diagram[1] (PVD) taken along the major axis of an edge-on system is a reliable bar diagnostic, particularly the presence of gaps between the signatures of the different periodic orbit families. In Chapter 4, we developed similar bar diagnostics using hydrodynamical simulations of the gaseous component alone. We showed that, when a nuclear spiral is present (corresponding to the existence of x_2 orbits, or equivalently of an inner Lindblad resonance), the presence of a gap in the PVD between the signature of the nuclear spiral and that of the outer parts of the disk reliably indicates the presence of a bar. If no nuclear spiral is present, one must rely on indirect evidence to argue for the presence of a bar. These gaps are a direct consequence of the shocks which develop in relatively strong bars. These shocks drive an inflow of gas toward the center of the galaxies and deplete the main and outer bar regions (see, e.g., Athanassoula 1992). The simulations in Chapter 4 can be directly compared with the emission line spectra presented here, and will form the basis of our argument.

These models can also be used to determine the viewing angle with respect to a bar, as the features present in the PVDs change with the orientation of the line-of-sight (see Ch. 3 and 4). In particular, when a bar is seen end-on, the signature of the flow associated with the x_1 orbits (the main bar region, elongated parallel to the bar) reaches very high radial velocities, while the signature of the flow associated with the x_2 orbits (the nuclear spiral, elongated perpendicular to the bar) shows only relatively low velocities. The opposite is true when a bar is seen side-on. In addition, the presence or absence of a nuclear spiral signature can somewhat constrain the mass distribution and bar pattern speed of an observed galaxy.

We have not developed specific observational criteria to identify past or current accretion of material in the observed galaxies. As discussed in § 5.2.1, accretion will occur through interaction or merger events. We will take as the signature of such events, and of possible accretion, the presence of irregularities in the observed PVDs, in particular strong asymmetries about the center of an object (see Fig. 5.1 for examples).

[1] Position-velocity diagrams (PVDs) show the projected density of material as a function of line-of-sight velocity and projected position.

5.4 Observations

5.4.1 The Sample

Our sample of galaxies consists of 30 edge-on spirals selected from the catalogues of Jarvis (1986), Shaw (1987), and de Souza & dos Anjos (1987) (spiral galaxies with a B/PS bulge), and from the catalogue of Karachentsev, Karachentseva, & Parnovsky (1993) (spiral galaxies with extreme axial ratios; see also Karachentsev et al. 1993). In order to have enough spatial resolution for the long-slit spectroscopy, but still be able to image the galaxies relatively quickly with a small-field near-infrared camera, we have selected objects with bulges larger than about $0\farcm6$ in diameter and disks smaller than about $7\farcm0$ (at the 25 B mag arcsec^{-2} level). All objects are accessible from the south ($\delta \leq 15°$). Two-thirds (21/30) of the galaxies either have probable companions or are part of a group or cluster. A few of these may be chance alignments, but it is fair to say that we are not biased either against or in favour of galaxies in a dense environment. We should therefore be able to estimate reliably the relative importance of accretion in the formation of B/PS bulges.

Of the sample galaxies described above, 80% (24/30) have a boxy or peanut-shaped bulge, while 20% (6/30) have a bulge of spheroidal morphology. Of the former group, 17 galaxies have emission lines extending far enough in the disk that we can apply the diagnostics developed in Chapters 3 and 4 using the ionised gas; all galaxies in the control group fulfill this condition. In this chapter, we will thus concentrate on a main sample of 17 edge-on spiral galaxies with B/PS bulges and on a "control" sample of 6 edge-on spiral galaxies with more spheroidal bulges. The galaxies in each sample are listed in Tables 5.1 and 5.2, along with information on their properties and environment. The galaxies with no or confined emission are listed in Table 5.3. We note that the galaxy type listed is not very reliable, as it is difficult to classify edge-on spirals.

Other than the catalogue of Karachentsev et al. (1993), we are not aware of any general catalogue of edge-on spiral galaxies. It is thus difficult to construct a large and varied control sample including edge-on spiral galaxies with large bulges (the Karachentsev et al. 1993 catalogue is restricted to galaxies with a major to minor axis ratio $a/b \geq 7$). Such a catalogue would be very useful.

5.4.2 Observations and Data Reduction

Our spectroscopic data were acquired over a total of 39 nights between December 1995 and May 1997, using the Double Beam Spectrograph on the 2.3 m telescope at Siding Spring Observatory. A 1752 $\times$ 532 pixels SITE ST-D06A

Table 5.1: Main Sample

Galaxy	Type	Bulge	Environment	Structure	Notes
NGC 128	S0 pec	Peanut	In group	Bar[a]	···
ESO 151- G 004	$S0^0$	Peanut	In group	Bar	···
NGC 1886	Sab	Boxy	Isolated	Bar	···
NGC 2788A	Sb	Peanut	In cluster	Bar	Dusty
IC 2531	Sb	Peanut	In cluster	Bar[b]	Dusty
NGC 3390	Sb	Boxy	Companions?	Accretion	···
NGC 4469	SB(s)0/a?	Peanut	Companions	Axisymmetric	···
NGC 4710	$SA(r)0^+$	Boxy	Isolated	Bar	···
PGC 44931	Sbc	Peanut	Isolated	Bar	···
ESO 443- G 042	Sb	Peanut	Companions?	Bar	Dusty
NGC 5746	SAB(rs)b?	Peanut	Isolated	Bar	···
NGC 6722	Sb	Peanut	Isolated	Bar	···
NGC 6771	$SB(r)0^+$?	Peanut	In group	Bar	···
IC 4937	Sb	Peanut	In cluster	Bar	Dusty
ESO 597- G 036	$S0^0$ pec	Peanut	In group	Accretion	Dusty
IC 5096	Sb	Boxy	Companions?	Bar	···
ESO 240- G 011	Sb	Boxy	In group	Bar	···

[a] Emsellem & Arsenault (1997)
[b] Bureau & Freeman (1997)

Table 5.2: Control Sample

Galaxy	Type	Bulge	Environment	Structure	Notes
NGC 1032	S0/a	Spheroidal	Companions	Axisymmetric	Dusty
NGC 3957	$SA0^+$	Spheroidal	In cluster	Axisymmetric	···
NGC 4703	Sb	Spheroidal	Isolated	Axisymmetric	Dusty
NGC 5084	S0	Spheroidal	In cluster	Accretion	···
NGC 7123	Sa	Spheroidal	Isolated	Accretion	Dusty
IC 5176	SAB(s)bc?	Spheroidal	Companions?	Axisymmetric	···

Table 5.3: Galaxies with No or Confined Emission

Galaxy	Type	Bulge	Environment	Notes
NGC 1381	SA0	Boxy	In cluster	···
NGC 1596	SA0	Boxy	In group	···
NGC 2310	S0	Boxy	Isolated	···
ESO 311- G 012	S0/a?	Boxy	Isolated	···
NGC 3203	$SA(r)0^+$?	Boxy	In group	···
IC 4767	S pec	Peanut	In cluster	···
ESO 185- G 053	SB pec	Peanut	In cluster	···

thinned CCD was used. The observations discussed in this chapter were obtained with the red arm of the spectrograph centered on the Hα λ6563 emission line. All galaxies were observed using a $1\farcs8 \times 400''$ slit aligned with the major axis. For objects with a strong dust lane, the slit was positioned just above it. The spectral resolution is about 1.1 Å FWHM (0.55 Å pixel^{-1}) and the spatial scale is $0\farcs9$ pixel^{-1}. These data can be directly compared with the PVDs obtained from the hydrodynamical simulations of Chapter 4. When no emission line was detected in an object, the red arm of the spectrograph was moved to the Ca II absorption line triplet. The blue arm was always centered on the Mg *b* absorption feature. These data will form the core of a future paper discussing the stellar kinematics of the sample galaxies (including the galaxies in Table 5.3). Total exposure times on both arms ranged from 12000 to 21000 s per object.

The spectra were reduced using standard procedures in IRAF. The data were first bias-subtracted, using both the vertical and horizontal overscan regions, and then using bias frames. If necessary, the data were also dark-subtracted. The spectra were then flatfielded using flattened continuum lamp exposures, and wavelength-calibrated using bracketing arc lamp exposures for each image. The data were then rebinned to a logarithmic wavelength (linear velocity) scale corresponding to 25 km s^{-1} pixel^{-1}. The spectra were then corrected for vignetting along the slit using sky exposures. All exposures of a given object were then registered and offset along the spatial axis, corrected to a heliocentric rest frame, and combined. The resulting spectra were then sky-subtracted using source-free regions of the slit on each side of the objects. The sky subtraction was less than perfect in some cases because of difficulties in obtaining a uniform focus of the spectrograph along the entire length of the CCD. This was particularly troublesome for objects like IC 2531 and NGC 5746 which extend over almost the entire length of the slit (see, e.g., Fig. 5.3a). In order to isolate the emission lines, the continuum emission of the objects was then subtracted using a low-order fit to the data. The resulting spectra constitute the basis of our discussion in the next section.

We note that in regions with bright continuum emission, like the centers of some galaxies, the continuum subtraction can leave relatively high shot noise in the data, which should not be confused with line emission in the grayscale plots of Figures 5.1–5.3. This is the case, for example, in the spectra of ESO 240- G 011, NGC 1032, and NGC 4703 (Figs. 5.1 and 5.2). The effect is perhaps best seen when a bright star is subtracted, such as seen in the spectra of NGC 2788A or NGC 1032 (see, again, Figs. 5.1 and 5.2).

We have not extracted rotation curves from our data. This is because we require the entire two-dimensional spectrum, or PVD, to identify the signature of a bar in an edge-on galaxy (see Ch. 3 and 4). Evidence of interaction and of possible accretion are also more easily seen in the two-dimensional spectra. We present spectra of the [N II] λ6584 emission line rather than the Hα line because it is not affected by underlying stellar absorption.

5.4.3 Results

We present here our emission line spectra for all the sample galaxies which have extended emission. The PVDs of the galaxies in the main sample are shown in Figure 5.1 and those of the control sample are shown in Figure 5.2. In order to illustrate the range of galaxy types and bulge morphologies in the sample, and to allow connections to be made between bulge morphologies and kinematical features in the disks, each PVD is accompanied by a registered image of the corresponding galaxy (Digitized Sky Survey) on the same spatial scale. We will discuss here the trends observed across the data set.

The most important trend, and the main result of this chapter, is that most of the galaxies in the main sample show a clear bar signature in their PVD (as described in § 5.3). Of the 17 galaxies in the main sample of spirals with a B/PS bulge and extended emission lines, we conclude that 14 galaxies are barred[2]. In these objects, the PVD clearly shows a strong and steep inner component, associated with a nuclear spiral (an x_2-like flow), and a slowly-rising almost solid-body component, associated with the outer parts of the disk, and joining the flat section of the rotation curve at large distances. Those two components are separated by a gap caused by the absence of gaseous material with an x_1-like behaviour in the barred region. The best examples of this type of bar signature, discussed in Chapters 3 and 4, are seen in the PVD of earlier-type objects, like NGC 2788A, NGC 5746, and IC 5096. However, the signature is still clearly visible in the PVD of galaxies as late as ESO 240- G 011 (see Fig. 5.1).

In the main sample, only one galaxy, NGC 4469, may be axisymmetric, with no evidence of either a bar or interaction. Two galaxies, NGC 3390 and ESO 597- G 036, have disturbed asymmetric PVDs, which we ascribe to recent interactions (obvious in the case of ESO 597- G 036). These interactions may have led to the accretion of external material. The results for the whole main sample are summarised in Table 5.1.

Another significant result of this study is that no galaxy in the control sample shows evidence for a bar. Four of the six galaxies appear to be axisymmetric, without evidence for either a bar or interaction, and two galaxies (NGC 5084 and NGC 7123) have a disturbed PVD, indicating that they underwent an interaction

[2]The PVDs of NGC 128 and IC 2531 do not display a bar signature, but Emsellem & Arsenault (1997) and Bureau & Freeman (1997) showed, using other data, that each galaxy harbours a bar.

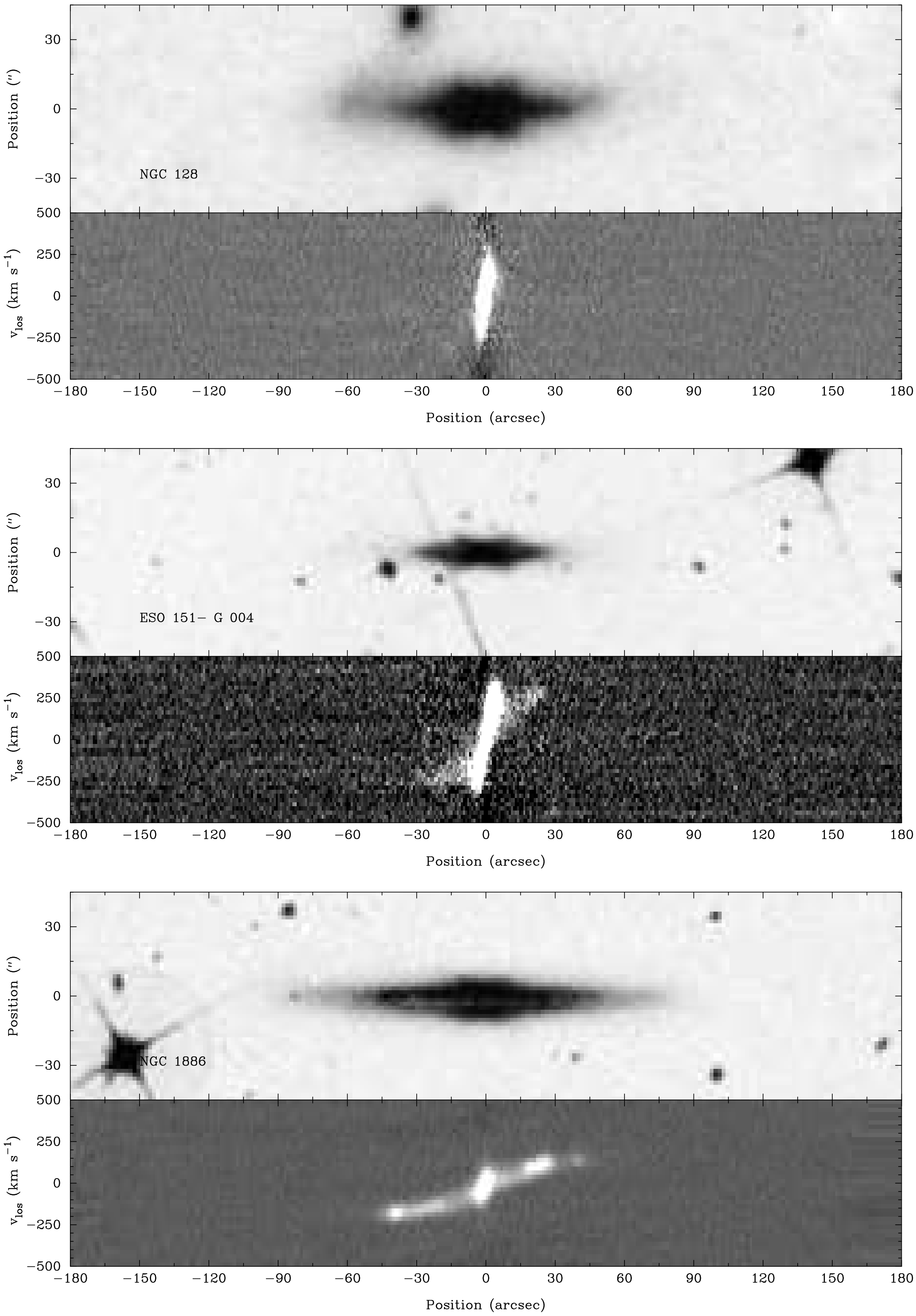

Figure 5.1: Structure and kinematics of the galaxies in the main sample of spirals with boxy/peanut-shaped bulges. Each plot corresponds to a galaxy. For each plot, the top panel shows a blue image of the galaxy (Digitized Sky Survey), which is identified in the bottom-left corner. The bottom panel shows the ionised gas ([N II] λ6584) position-velocity diagram (PVD) of the galaxy along its major axis, registered with the image above it. The galaxies are ordered as in Table 5.1.

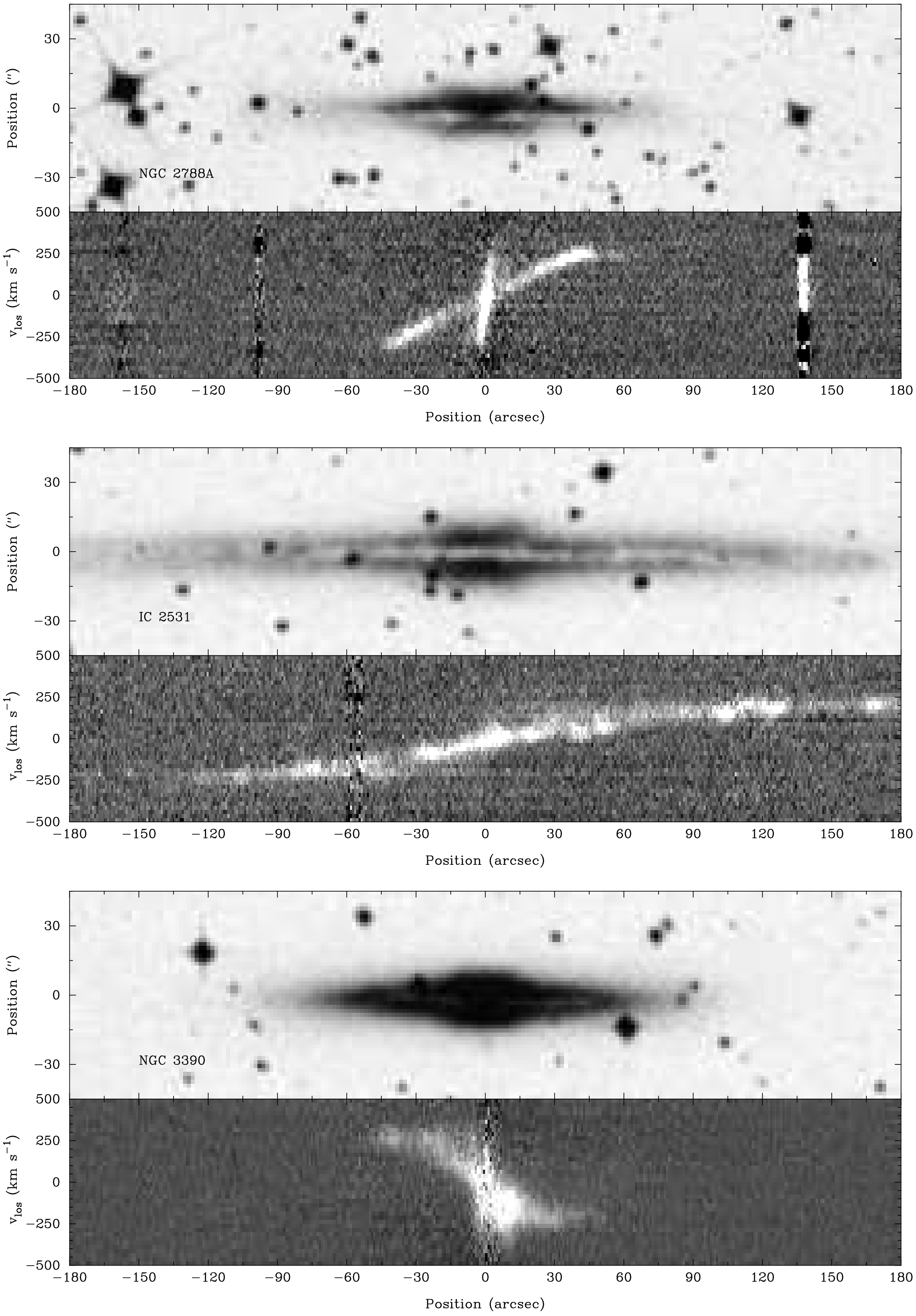

Figure 5.1: *Continued.*

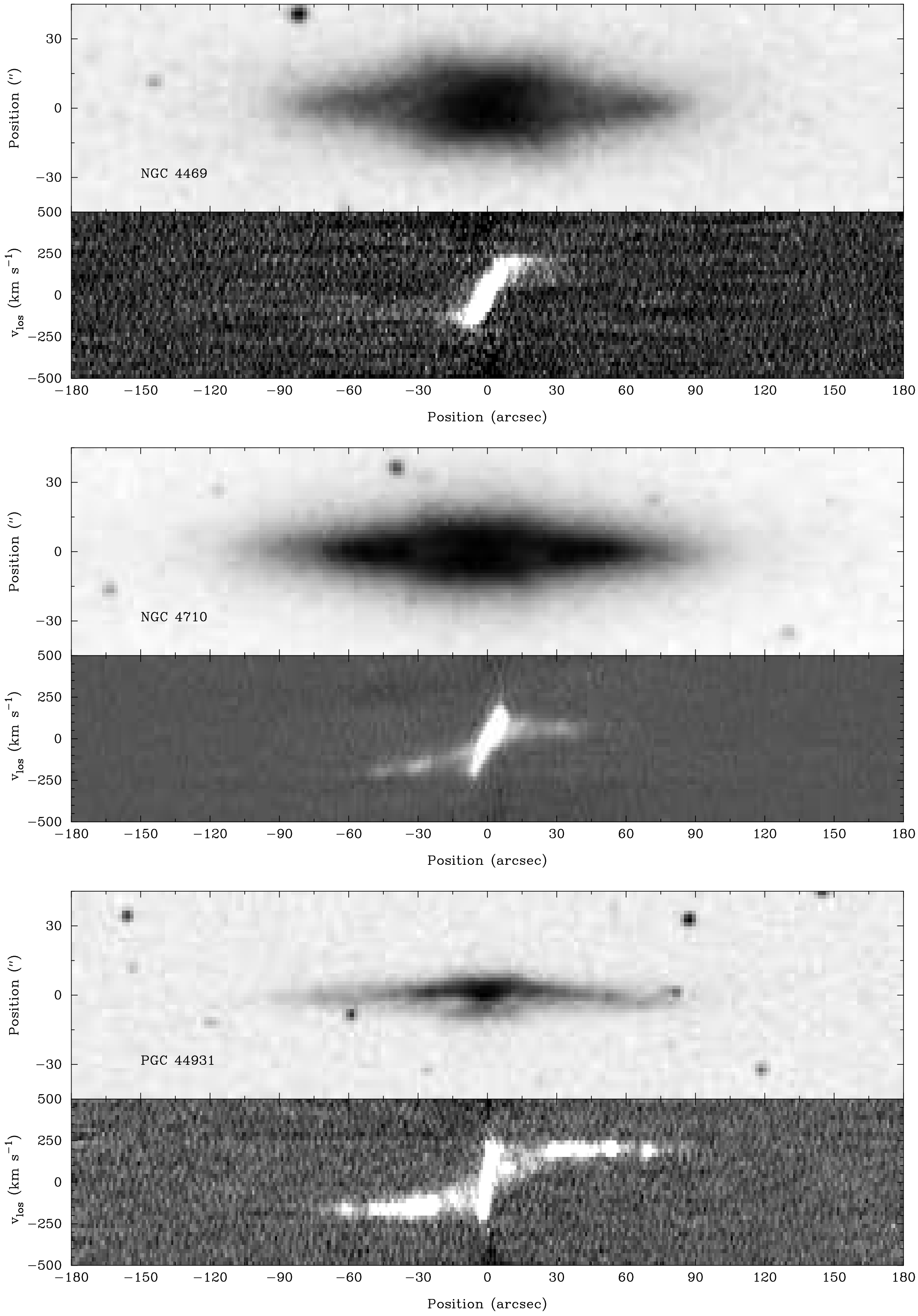

Figure 5.1: *Continued.*

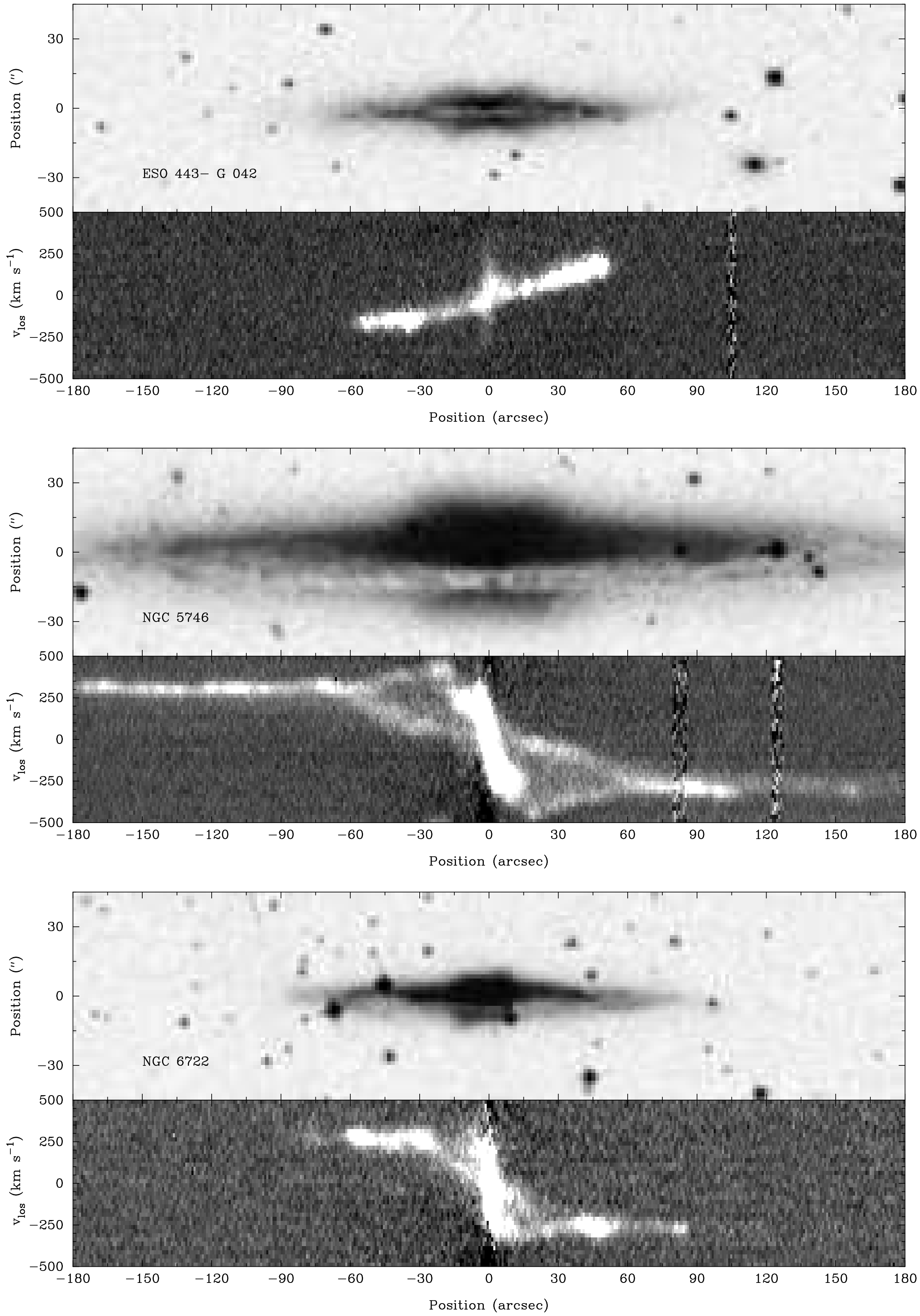

Figure 5.1: *Continued.*

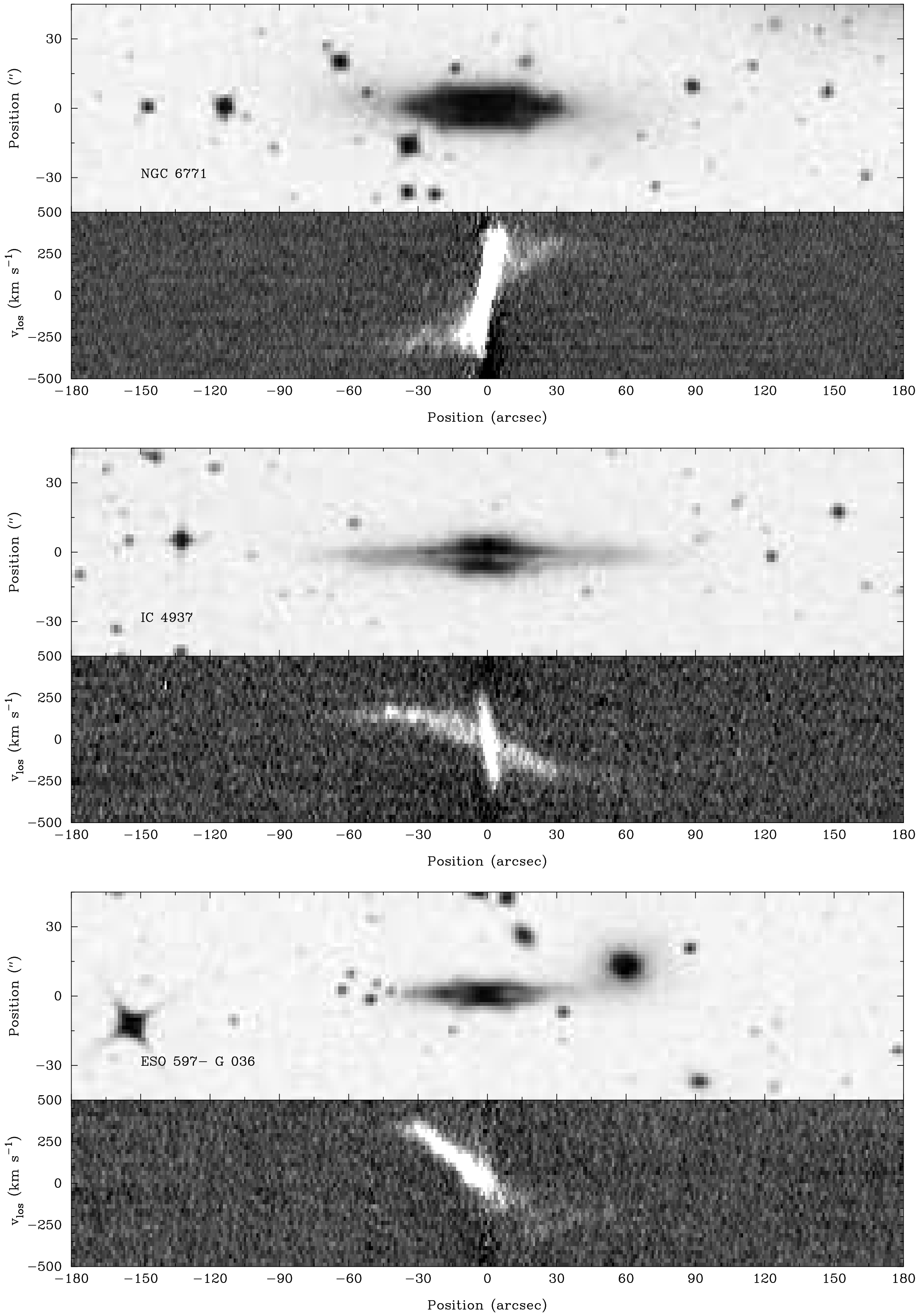

Figure 5.1: *Continued.*

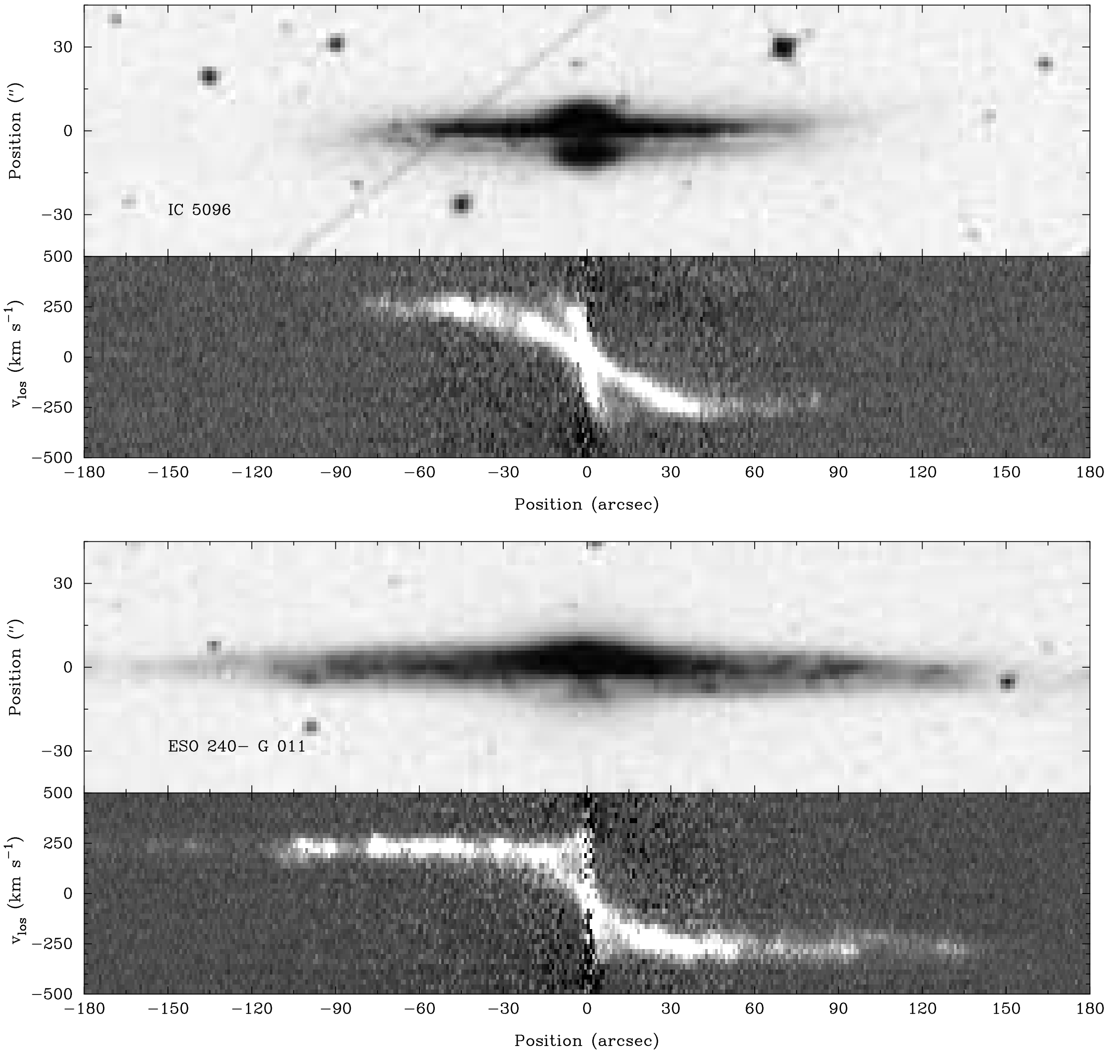

Figure 5.1: *Continued.*

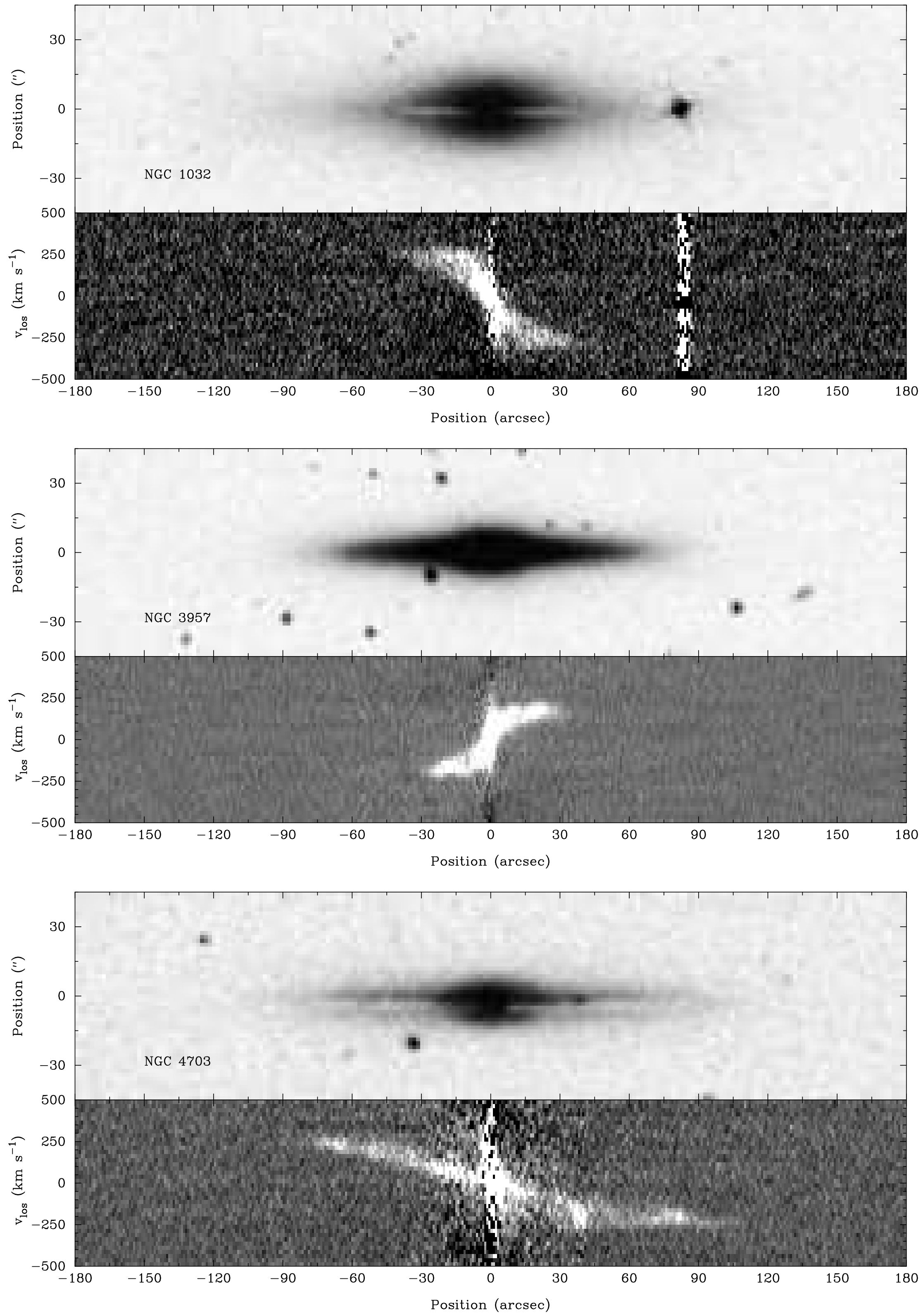

Figure 5.2: Same as Figure 5.1 but for the control sample of spirals with spheroidal bulges. The galaxies are ordered as in Table 5.2.

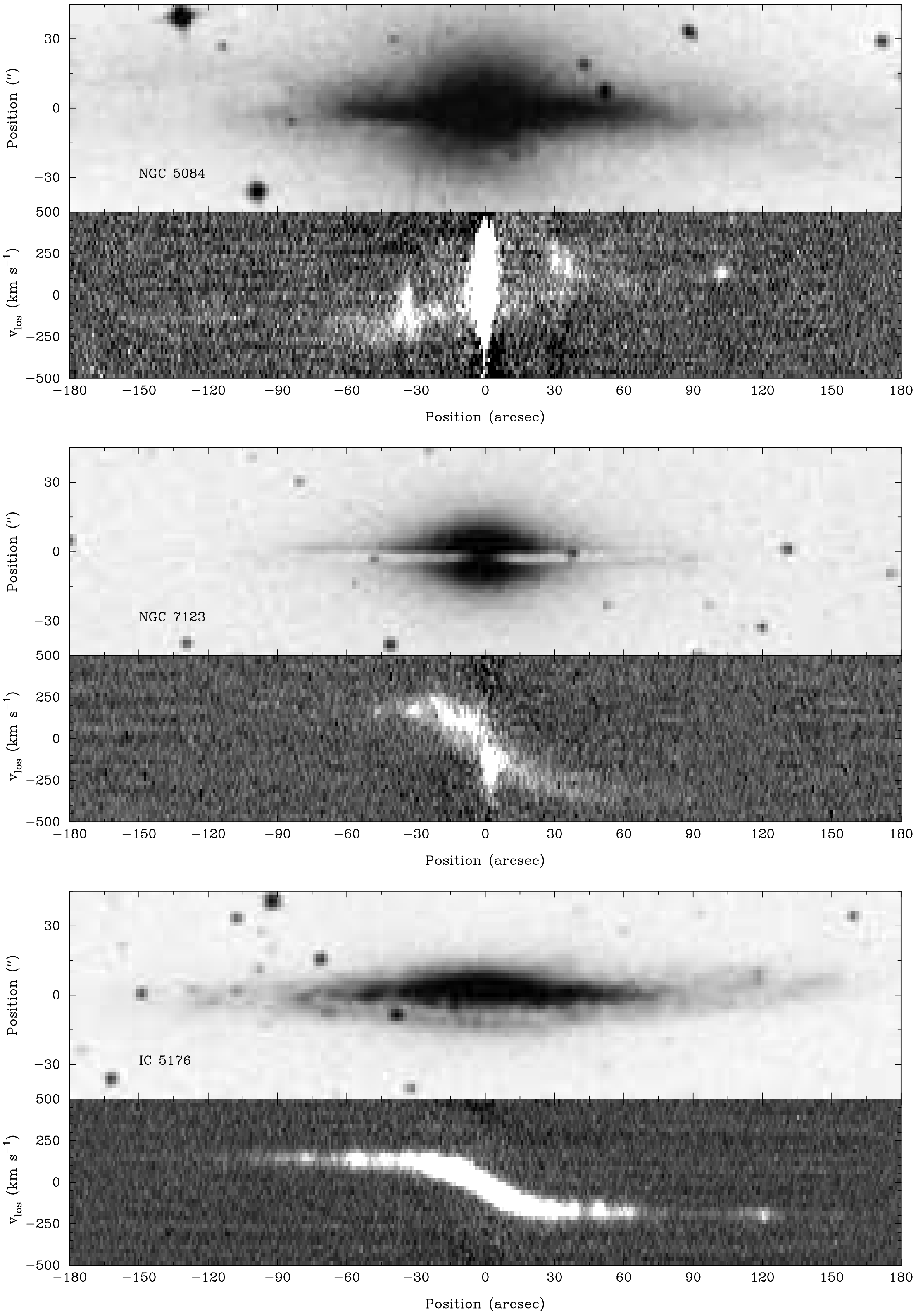

Figure 5.2: *Continued.*

recently and possibly accreted material. These results are tabulated in Table 5.2.

5.5 Discussion

The only previous study of this kind was that of Kuijken & Merrifield (1995), who proposed the method and considered two galaxies. This is thus the first systematic observational study of the relationship between bars and B/PS bulges in spiral galaxies. In summary, our main result is that 14 galaxies out of the 17 galaxies with a B/PS bulge are barred, and the remaining 3 galaxies show evidence of interaction or may be axisymmetric. None of the 6 galaxies in the control sample shows any evidence for a bar.

This means that most B/PS bulges are due to the presence of a thick bar viewed edge-on, and only a few examples may be due to the accretion of external material. In addition, the more spheroidal bulges (i.e. non-B/PS) seem to be axisymmetric. It appears then that most B/PS bulges are edge-on bars, and that most bars are B/PS when viewed edge-on. However, the small size of the control sample prevents us from making a stronger statement about this converse.

If bars were unrelated to the structure of bulges, we would have expected only about 5 galaxies in the main sample to be strongly barred, and about 2 galaxies in the control sample (about 30% of spirals are strongly barred; see Sellwood & Wilkinson 1993). Clearly, our results are incompatible with these expectations.

Our association of bars and B/PS bulges supports the bar-buckling mechanism for the formation of the latter. However, we do not test directly for buckling, but rather for the presence of a barred potential in the plane of the disks. Because bars form rapidly and buckle soon after, on a timescale of only a few dynamical times (see, e.g., Combes et al. 1990), it is unlikely that any galaxy in this nearby sample would have been caught in the act of buckling. Thus, other mechanisms which may lead to thick bars cannot be excluded. In addition, we have no way of determining how the bars themselves formed, or even whether they formed spontaneously in isolation or through interaction with nearby galaxies. Therefore, the possibility of hybrid scenarios for the formation of B/PS bulges, where a bar is formed through an interaction and subsequently thickens due to the buckling instability (see § 5.2.2), remains.

We have looked mainly at objects with large bulges; only two of the galaxies studied are late-type spirals (ESO 240- G 011 and IC 5176). This is a selection effect due to the difficulty of identifying a very small bulge as B/PS. It would therefore be interesting to search for bars in very late-type edge-on spiral galaxies, and verify whether thin bars do exist. The bar in ESO 240- G 011 is not very thick, but it is thicker (isophotally) than the disk. H I synthesis imaging is probably the best way to achieve this goal, as these objects are often dusty and H I-rich. We will report on H I synthesis observations of a few objects in our sample in a later paper.

In Chapters 3 and 4, we proposed diagnostics, again based on the structure of an observed PVD, to determine the viewing angle with respect to the bar in an edge-on barred disk (see also § 5.3). When the bar is seen close to side-on, the nuclear spiral signature is compact and steep, and the maximum radial velocity it reaches is similar to or larger than the flat portion of the rotation curve. When the bar is seen close to end-on, the nuclear spiral signature extends to relatively large distances and only reaches low velocities. These diagnostics are ideally suited to test the prediction of N-body models, that bars are peanut-shaped when seen side-on and boxy-shaped when seen end-on (see, e.g., Combes & Sanders 1981; Raha et al. 1991).

Of the 12 barred galaxies in the main sample where it is possible to apply these criteria (we exclude NGC 128 and IC 2531), two-thirds (8/12) seem to be consistent with the above prediction from N-body simulations. For example, in the galaxy with a peanut-shaped bulge IC 4937, it is clear that the steep inner component associated with the nuclear spiral extends to higher radial velocities than the outer parts of the disk (see Fig. 5.1). This situation is reversed in NGC 1886, which has a boxy-shaped bulge. However, caution is required when interpreting this result. Firstly, the present classification of the shape of the bulges is affected both by dust and the low dynamic range of the survey material used (Digitized Sky Survey). To remedy this problem, we have acquired K-band images of all the sample galaxies and we will report on these observations in a future paper. Secondly, no clear prediction has been made from N-body simulations about the viewing angle where the transition from a boxy to a peanut-shaped bulge occurs. In that regard, it would be useful to apply quantitative measurements of the boxiness and "peanutness" of the bulges to both observational data and simulation results (see, e.g., Bender & Möllenhoff 1987 and Athanassoula et al. 1990 for two possible methods). Thirdly, because the nuclear spiral is located near the center of the galaxies, the velocities it reaches depend somewhat on the central concentration of the objects (which affects the circular velocity in the central regions). This obviously varies amongst the galaxies in our sample. Therefore, while our observations weakly support the prediction of N-body models concerning the orientation of the bars in B/PS bulges, we believe that it is premature to make a detailed quantitative comparison of the data with the models.

For a more detailed comparison with theory, data of higher signal-to-noise and higher spatial resolution than the average PVD presented here would be very desirable. In that spirit, it would be worthwhile to model individually the best PVDs obtained in the present study (e.g. NGC 5746, IC 5096, and a few others).

This would very likely lead to tight constraints on the mass distribution of the galaxies and the properties of the bar, including the pattern speed (see Ch. 3 and 4).

Because many galaxies in our sample have a prominent dust lane, it is important to consider the possible effects of dust on our observations. The major effect of dust in an edge-on system is to limit the depth to which the line-of-sight penetrates the disk. However, we selected many galaxies to be slightly inclined, so it was possible in those objects to position the slit just above the dust lane, and have a line-of-sight that still goes through most of the disk, as required for a comparison with the models of Chapters 3 and 4. In the few cases with a strong dust lane and a perfectly edge-on disk, we tried again to put the slit just above the dust layer. Unfortunately, with the observational set-up available at the telescope, it was difficult to locate the slit with great precision. The objects where we suspected that dust could affect our observations are indicated in Tables 5.1–5.3.

A large dust optical depth in an edge-on disk produces an almost featureless PVD, and the rotation curve appears slowly-rising and solid-body, as one sees only an outer annulus of material in the disk (see, e.g., Bosma et al. 1992). The only objects showing obvious signs of absorption are IC 2531[3] and NGC 4703 (and possibly ESO 443- G 042). Because we see a lot of structure in most PVDs, including the PVDs of objects with a significant dust lane, we do not believe that our results are significantly affected by dust; we do detect a clear bar signature in most objects of the main sample.

This statement is strengthened by the fact that all the PVDs showing a bar signature are close to symmetric. We showed in Chapter 4 that the bar signature would be strongly asymmetric for a very dusty disk, and this is not observed. Similarly, it is improbable that irregular dust distributions would lead to such well-ordered and symmetric PVDs (very large dust patches would be required to create the gaps observed in many objects).

An unexpected but interesting prospect raised by our observations concerns emission line ratios. For many of the barred galaxies in the main sample, the emission line ratios in the central regions are different from those expected of typical H II regions. For 9 barred galaxies out of 14, mostly those with the strongest bar signatures, the [N II] $\lambda6584$ to Hα $\lambda6563$ ratio is greater than unity in the bulge region. Furthermore, in a few objects, the steep inner component of the PVD, associated with the nuclear spiral, is much stronger in [N II] than it is in Hα, while the slowly rising component, associated with the outer parts of the disk, has a [N II]/Hα ratio typical of H II regions. In fact, the inner component can be almost absent in Hα. We illustrate those two behaviours in Figure 5.3

[3]This is confirmed by the H I radio synthesis data of Bureau & Freeman (1997), which reveal a complex PVD with a bar signature.

with the PVDs of NGC 5746 and IC 5096.

It is possible that the Hα emission line is weakened by the underlying stellar absorption line. This suggestion is supported by the fact that the spectra of many galaxies show strong Balmer absorption lines. However, the Hα absorption would need to be very large to account for the extreme [N II]/Hα ratios observed in some objects (see, e.g., Fig. 5.3). The strong Balmer lines observed in many objects are interesting in themselves, and indicate that a significant intermediate age ($\sim$ 1 Gyr) stellar population is present in the central regions of the disk of many objects. It would be interesting to see if these past bursts of star formation are related to the presence of the bars.

The high emission line ratios are interesting for two reasons. Firstly, high [N II]/Hα ratios are believed to be produced by shocks (see, e.g., Binette, Dopita, & Tuohy 1985; Dopita & Sutherland 1996). This is consistent with the view that B/PS bulges are simply bars viewed edge-on. The steep inner components of the PVDs, which display high [N II]/Hα ratios, are associated with the nuclear spirals observed in many barred spiral galaxies (see Ch. 4). Athanassoula (1992) showed convincingly that these are the locus of shocks. Secondly, if one were to derive Hα and [N II] rotation curves from the data, by taking the upper envelope of the PVDs (as is usually done), the Hα and [N II] rotation curves would differ significantly for many objects. The Hα line would yield slowly rising rotation curves flattening out at relatively large radii, while the [N II] line would yield rapidly rising rotation curves flattening out at small radii. The mass models derived from such data would thus yield qualitatively different results, and our understanding of galactic dynamics and structure gained from this type of work could be seriously erroneous (at least for highly inclined spirals). Of course, now that we have established that these galaxies are barred, their rotation curves should not be used directly for mass modelling, as they are not a good representation of the circular velocity.

On the other hand, data such as those presented in Figure 5.3 open up the possibility of determining the ionisation conditions and abundance of the gas in different regions of the galaxies. Because the deprojected location of each component of the PVDs is known (see Ch. 4), we can study the effects of bars on the interstellar medium of the galaxies on various scales. A study of this type will be presented in the future.

5.6 Conclusions

In this chapter, we discussed the various mechanisms proposed for the formation of boxy and peanut-shaped bulges in edge-on spiral galaxies. We argued that accretion scenarios were unlikely to account for most boxy/peanut-shaped (B/PS) bulges, but that bar-buckling scenarios, discovered through N-body simulations,

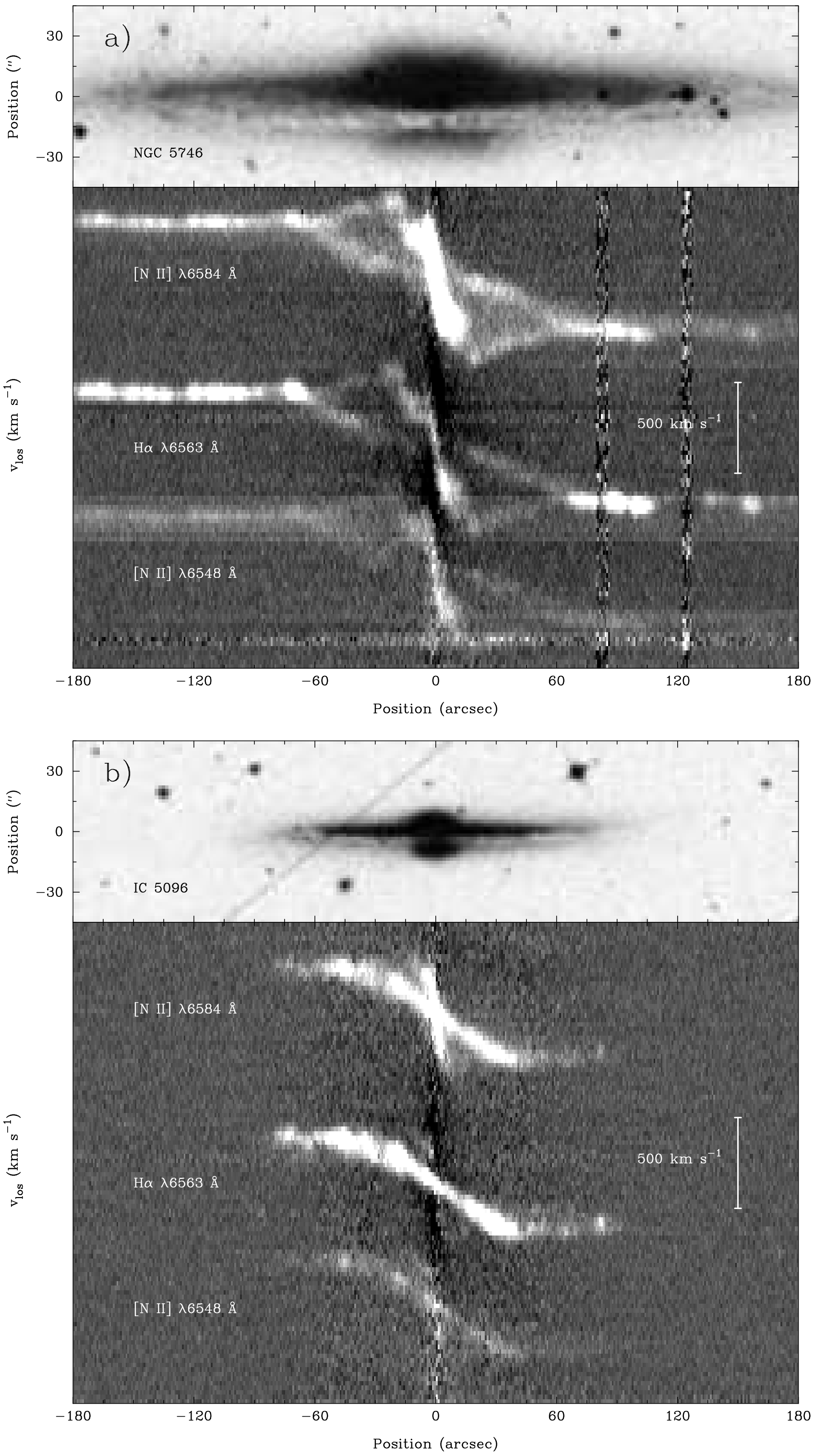

Figure 5.3: Structure and kinematics of (a) NGC 5746 and (b) IC 5096. For each plot, the top panel shows a blue image of the galaxy (Digitized Sky Survey). The bottom panel shows ionised gas position-velocity diagrams (PVDs) of the galaxy along its major axis, registered with the image above it. The PVDs correspond to the [N II] λ6584, Hα λ6563, and [N II] λ6548 emission lines (from top to bottom). Note the large [N II] λ6584 to Hα ratio in the central component of the PVDs.

had this potential. Using kinematical bar diagnostics recently developed for edge-on spirals, we searched for bars in a large sample of edge-on spiral galaxies with a B/PS bulge. Of the 17 galaxies where the diagnostics could be applied using emission lines, 14 galaxies showed the presence of a bar, 2 galaxies were significantly affected by interactions, and 1 galaxy may be axisymmetric. In a control sample of 6 galaxies with a spheroidal bulge, none appeared to be barred.

Our study supports the bar-buckling mechanism for the formation of B/PS bulges. Our results imply that most B/PS bulges are due to the presence of a thick bar viewed edge-on, while only a few may be due to the accretion of external material. Furthermore, spheroidal bulges do appear to be axisymmetric. This suggests that all bars are B/PS. Our observations also seem to support the prediction of N-body simulations, that bars appear boxy-shaped when seen end-on and peanut-shaped when seen side-on. However, this issue should be revisited in a more quantitative manner in the future. With our data, we have no way of determining whether the bars leading to B/PS bulges have formed in isolation or through interactions and mergers. The association of B/PS bulges and bars is entirely consistent with the properties of the bulge of the Milky Way, which is known to be both boxy and bar-like.

We considered the effects of dust on our observations but concluded that it does not affect our results significantly. We have also shown that emission line ratios correlate with kinematical structures in many barred galaxies. This make possible a direct study of the large scale effects of bars on the interstellar medium in disks.

Our study opens up the possibility of studying the vertical structure of bars. Observationally, this has not been done before and represents an interesting spin-off from the use of bar diagnostics in edge-on spiral galaxies. We have obtained K-band images for all our sample galaxies to study their vertical structure and avoid dust-related problems. We will report on their vertical light distribution in a future paper.

References

Araki, S. 1985, Ph.D. Thesis, Massachusetts Institute of Technology

Athanassoula, E. 1992, MNRAS, 259, 345

Athanassoula, E., Morin, S., Wozniak, H., Puy, D., Pierce, M. J., Lombard, J., & Bosma, A. 1990, MNRAS, 245, 130

Athanassoula, E., & Sellwood, J. A. 1986, MNRAS, 221, 213

Bender, R., & Möllenhoff, C. 1987, A&A, 177, 71

Bettoni, D., & Galletta, G. 1994, A&A, 281, 1

Binette, L., Dopita, M. A., & Tuohy, I. R. 1985, ApJ, 297, 476

Binney, J. J., Gerhard, O. E., Stark, A. A., Bally, J., & Uchida, K. I. 1991, MNRAS, 252, 210

Binney, J., & Petrou, M. 1985, MNRAS, 214 449

Bosma, A., Byun, Y., Freeman, K. C., & Athanassoula, E. 1992, ApJ, 400, L21

Bureau, M., & Freeman, K. C. 1997, PASA, 14, 146

Combes, F., Debbasch, F., Friedli, D., & Pfenniger, D. 1990, A&A, 233, 82

Combes, F., & Sanders, R. H. 1981, A&A, 96, 164

Debattista, V. P., & Sellwood, J. A. 1998, ApJ, 493, L5

de Carvalho, R. R., & da Costa, L. N. 1987, A&A, 171, 66

de Souza, R. E., & dos Anjos, S. 1987, A&AS, 70, 465

Dopita, M. A., & Sutherland, R. S. 1996, ApJS, 102, 161

Emsellem, E., & Arsenault, R. 1997, A&A, 318, L39

Fridman, A. M., & Polyachenko, V. L. 1984, Physics of Gravitating Systems (New York: Springer-Verlag)

Friedli, D., & Benz, W. 1993, A&A, 268, 65

Gerin, M., Combes, F., & Athanassoula, E. 1990, A&A, 230, 37

Hamabe, M., & Wakamatsu, K. 1989, ApJ, 339, 783

Hasan, H., & Norman, C. 1990, ApJ, 361, 69

Hernquist, L., & Quinn, P. J. 1989, ApJ, 342, 1

Jarvis, B. J. 1986, AJ, 91, 65

Kalnajs, A. J. 1971, ApJ, 166, 275

———. 1977, ApJ, 212, 637

Karachentsev, I. D., Karachentseva, V. E., & Parnovsky, S. L. 1993, Astron. Nachr., 314, 97

Karachentsev, I. D., Karachentseva, V. E., Parnovsky, S. L., & Kudrya, Y. N. 1993, Astron. & Astrophys. Trans., 4, 143

Kormendy, J., & Illingworth, G. 1982, ApJ, 256, 460

Kuijken, K. 1996, in Barred Galaxies, ed. R. Buta, D. A. Crocker, and B. G. Elmegreen (ASP: San Francisco), 505

Kuijken, K., & Merrifield, M. R. 1995, ApJ, 443, L13

May, A., van Albada, T. S., & Norman, C. A. 1985, MNRAS, 214 131

Merrifield, M. R. 1996, in Barred Galaxies, ed. R. Buta, D. A. Crocker, and B. G. Elmegreen (ASP: San Francisco), 179

Mihos, J. C., Walker, I. R., Hernquist, L., de Oliveira, M. C., & Bolte, M. 1995, ApJ, 447, L87

Miwa, T., & Noguchi, M. 1998, ApJ, 499, 149

Mulder, W. A., & Liem, B. T. 1986, A&A, 157, 148

Noguchi, M. 1987, MNRAS, 228, 635

Norman, C. A., Sellwood, J. A., & Hasan, H. 1996, ApJ, 462, 114

Paczyński, B., Stanek, K. Z., Udalski, A., Szymański, M., Kałużny, J., Kubiak, M., Mateo, M., & Krzemiński, W. 1994, ApJ, 435, L113

Peters, W. L. 1975, ApJ, 195, 617

Pfenniger, D. 1984, A&A, 134, 373

Pfenniger, D., & Friedli, D. 1991, A&A, 252, 75

Raha, N., Sellwood, J. A., James, R. A., & Kahn, F. D. 1991, Nature, 352, 411

Rowley, G. 1986, Ph.D. Thesis, The Australian National University

———. 1988, ApJ, 331, 124

Sellwood, J. A. 1980, A&A, 89, 296

——— 1981, A&A, 99, 362

Sellwood, J. A., & Wilkinson, A. 1993, Rep. Prog. Phys., 56, 173

Shaw, M. A. 1987, MNRAS, 229, 691

———. 1993, MNRAS, 261, 718

Toomre, A. 1966, in Geophysical Fluid Dynamics, 1966 Summer Study Program at Woods Hole Oceanographic Institution, ref. no. 66-46, 111

Weiland, J. L., et al. 1994, ApJ, 425, L81

Weinberg, M. D. 1985, MNRAS, 213, 451

Whitmore, B. C., & Bell, M. 1988, ApJ, 324, 741

Chapter 6

Conclusion

Each chapter of this thesis contains an abstract and a conclusion with a summary of its main results, and it would be too repetitive to provide yet another summary in this chapter. We will thus recall only the main achievements of each chapter and their importance in the next section. We then describe some ongoing projects aimed at increasing our understanding of spiral galaxies with a boxy/peanut-shaped (B/PS) bulge, but which are still incomplete. In the last section, we discuss possible applications of the methods used in this thesis to other fields of astronomy, in particular to the study of the structure and dynamics of other galaxy types.

6.1 Summary of Main Results

In Chapter 2, we successfully measured the pattern speed of the H I disk in the galaxy NGC 2915, using the method proposed by Tremaine & Weinberg (1984). This is only the second direct measurement of a bar pattern speed, and the first one in a gas-rich galaxy. NGC 2915 is a unique object, with a blue compact dwarf galaxy "core" and a very extended H I disk (Meurer, Mackie, & Carignan 1994; Meurer et al. 1996). This disk shows a strong bar and a well-developed spiral pattern. We demonstrated that the bar pattern speed is slow, too slow to be consistent with models of self-gravitating disks. NGC 2915 is dynamically dominated by dark matter (Meurer et al. 1996), and we argued that the structure and kinematics of the disk could be explained by the effects of an extended triaxial halo with a slowly rotating figure. If we are right, systems such as NGC 2915 could helps us constrain the geometry and dynamics of dark halos, and may at the same time provide important constraints on cosmological structure formation scenarios.

In the following chapters, we concentrated on testing the possible relationship between bars and B/PS bulges. Such a relationship should exist if bar-buckling is the dominant formation mechanism for these objects. In order to achieve this goal, we developed methods to identify bars in edge-on spiral galaxies. Following the work of Kuijken & Merrifield (1995), we adopted in Chapter 3 an approach based on periodic orbits, considering periodic orbit families as building blocks to model real galaxies. We showed that the global structure of the position-velocity diagrams (PVDs), derived using an edge-on projection, is a reliable bar diagnostic in edge-on disks. In particular, the non-homogeneous distribution of the orbits in a barred galaxy creates characteristic gaps in the PVDs, between the signatures of the various families of periodic orbits. Although periodic orbits are only an approximation to the structure and kinematics of a real galaxy, they provide insight into the properties of real systems, and are an invaluable tool for the development and understanding of more complex and realistic models.

In Chapter 4, we developed better bar diagnostics for edge-on spirals, using hydrodynamical simulations which specifically target the gaseous disk component (see Athanassoula 1992). We showed that, when a nuclear spiral is formed, gaps appear in the PVDs between the signature of the nuclear spiral and that of the outer parts of the disk. The gaps dominate the structure of the PVDs, and are a good bar diagnostic to be used with real observations, where the spatial and spectral resolutions are often limited. The shape of the signature of the nuclear spiral can also be used to determine the viewing angle with respect to the bar.

In Chapter 5, we used our diagnostics to study the relationship between bars and B/PS bulges. We searched for bars in a large sample of edge-on spiral galaxies with a B/PS bulge, and in a smaller sample of edge-on galaxies with a more spheroidal bulge. We showed that most B/PS bulges are due to a thick bar viewed edge-on, while only a few extreme cases may be due to the accretion of external material. This strongly supports the bar-buckling mechanism for the formation of B/PS bulges, and implies that accretion plays at most a minor role in their formation. None of the galaxies in the control sample were barred, which suggests in addition that most bars are B/PS.

The observations presented in Chapter 5 demonstrate the power of the diagnostics developed. These can now be used as a simple tool for a range of other studies. In particular, by providing an easy way to identify bars in edge-on spiral galaxies, they allow us to study the influence of bars on the vertical structure of disks. Observationally, this has never been possible before.

6.2 Work in Progress

The observations presented in Chapter 5 represent only a subset of the data collected during this thesis. For all the sample galaxies, we have also obtained long-slit absorption line spectroscopic data, near-infrared (NIR) K-band imaging data, and optical BVI-band images. We have also acquired H I radio synthesis data for a small number of objects. We will now discuss the status and goals of these observations, as well as the status of other related projects.

6.2.1 Penetrating the Dust Barrier: H I Line-Imaging

To study the vertical light distribution of bars/bulges, it is preferable to use galaxies which are as edge-on as possible. This reduces problems associated with deprojecting the light distribution of slightly inclined systems, and with removing contaminating disk light from the bulges. However, as we discussed in Chapter 5, dust can reduce our ability to identify bars in perfectly edge-on systems, especially if they have a strong dust lane. The solution is to apply the bar diagnostics in regions of the spectrum which are less affected by dust.

Because spiral disks are probably optically thin at K-band (see Byun 1992), the NIR H Brγ line would be well-suited for this type of work, but the line is weak in most galaxies and NIR spectrographs with adequate resolution are not common. Another solution is to use H I line-imaging observations with a radio synthesis telescope. It is then possible to obtain PVDs through dust lanes, with a higher spectral resolution than possible optically. In addition, because of the full 2D spatial coverage, such data provide a better observational handle on possible interaction and/or accretion of material. Using the Australia Telescope Compact Array (ATCA), we have surveyed 10 objects in our sample for H I, focussing on the largest and more dusty galaxies with $\delta \lesssim -24°$ (to obtain a full uv coverage with the ATCA). Because the bar diagnostics developed require relatively high spatial resolution, we had to use the longest but least sensitive arrays (6 km). We detected 4 galaxies: IC 2531, NGC 6771, ESO 240- G 011, and NGC 5084. For each of these galaxies, we have now acquired a complete data set, consisting of observations in three different configurations (2×6 km, 1×1.5 km).

The goal of these observations is similar to that of the emission line spectroscopy presented in Chapter 5. Our main aim is to verify the presence of a bar in the edge-on disks. For IC 2531, this has already proven successful. The optical observations showed a featureless PVD, but a bar signature is clearly visible in the H I data (see Bureau & Freeman 1997a for preliminary results). It will also be interesting to compare the PVDs obtained in H I with those obtained from the ionised gas (Ch. 5), as each traces a different phase of the interstellar medium. In addition, as mentioned above, the H I observations provide us with a better way to evaluate the importance of interaction/accretion in the systems. In that regard, NGC 6771 and NGC 5084 will be particularly useful, as there is already independent evidence for interaction in these systems. The observations can also be used to study issues outside of the main emphasis of this thesis. For example, they can be used to study the warping and flaring of the H I layer in the outer parts of the disks (see, e.g., Olling 1995, 1996). The analysis of these observations is, however, in a preliminary state. We will report on our results in a future paper.

6.2.2 Stellar Diagnostics: Absorption Line Spectroscopy

The bar diagnostics developed in Chapter 4 were targeted specifically at the gaseous component of spiral galaxies. Because many of the features in the PVDs are due to the collisional nature of gas (the presence of shocks), it is not possible to use these diagnostics directly to interpret stellar spectra. The periodic orbits approach used in Chapter 3 probably provides a better approximation to the stellar kinematics. However, even this approach is unsatisfactory at a quantitative level, because stars are not restricted to move on periodic orbits. Most stars are probably simply trapped around these orbits and, in some circumstances, there may be a significant numbers of stars on irregular (chaotic) orbits (see, e.g., Sellwood & Wilkinson 1993). We thus expect the PVDs produced in Chapter 3 to appear "washed out" in more realistic stellar models.

In collaboration with E. Athanassoula, we have begun a project to produce bar diagnostics in edge-on spiral galaxies based on the stellar kinematics, in a manner analogous to that of Chapter 4 with the gas kinematics. For that, we are using the results of a small number of 3D N-body simulations of rotationally supported disks. As in the simulations reported by other groups (e.g. Combes et al. 1990), these disks rapidly form bars which buckle and settle with a boxy/peanut shape. By projecting these models edge-on, we are able to produce PVDs analogous to those of Chapters 3 and 4. These will allow us to design proper bar diagnostics to be used in conjunction with stellar kinematical observations. In addition, these models will enable us to quantify how much the bar signature changes as the disk is inclined. We have conducted a preliminary analysis of some PVDs, but a more thorough investigation is required before we report on these results.

On the observational side, we have obtained absorption line spectroscopic data for all the sample galaxies, simultaneously with the emission line data described in Chapter 5. The blue arm of the spectrograph was centered on the Mg b absorption feature ($\lambda 5190$) and, when no emission line was detected, the red arm of the spectrograph was moved to the Ca II absorption line triplet ($\lambda 8600$). It will be interesting to compare the stellar kinematics in the sample galaxies with those predicted from the N-body models described above. In particular, for the sample galaxies with no or confined emission lines (see Table 5.3), where the diagnostics developed in Chapter 4 could not be used, we will now be able to verify whether or not the disks harbour a bar. This will extend the work described in Chapter 5 to the whole galaxy sample, and will hopefully strengthen our conclusions concerning the origin of B/PS bulges. The analysis of the absorption line spectra is still underway, and, again, we will report on these at a later date.

6.2.3 The Vertical Structure of Bars: K-Band Imaging

The N-body simulations discussed in the previous section have wider applications than the simple development of bar diagnostics for the stellar component of spiral galaxies. By quantifying the boxiness of the bulges (e.g. Athanassoula et al. 1990), we will be able to study how the bar/bulge shape varies with the inclination of the disk and the viewing angle to the bar. This will put better constraints on the likelihood of detecting B/PS bulges for various lines-of-sight, and will thus provide a better comparison for existing surveys (e.g. Shaw 1987), and for observations of individual systems.

We have also obtained K-band imaging data for all the sample galaxies, using CASPIR (Cryogenic Array SPectrometer/ImageR) on the 2.3 m telescope at Siding Spring Observatory. These will be used to construct mosaiced images of the galaxies, each galaxy requiring mosaicing of 2–5 CASPIR fields aligned with the major axis (the individual fields are about $2' \times 2'$). The use of K-band data is essential to reduce the effects of dust, especially for galaxies with a strong dust lane (see Kuchinski & Terndrup 1996).

Our observations have two main goals. Firstly, we aim to obtain an improved classification of the morphology of the bulges for the sample galaxies (boxy versus peanut-shaped), compared to that of Chapter 5. In conjunction with the observed PVDs, the K-band images will thus provide a strong test of the bar-buckling scenario for the formation of B/PS bulges, which predicts that the bulges appear boxy-shaped when the bar is seen close to end-on and peanut-shaped when the bar is seen close to side-on (see, e.g., Combes et al. 1990).

Secondly, we aim to study the vertical structure of bars. Observationally, this has never been done before, mostly because no reliable bar diagnostic in edge-on spiral galaxies was available. Our primary goal is to compare the observed vertical light distribution of bars with that predicted from 3D N-body simulations of rotationally supported disks. These predict vertical light profiles which are closer to an exponential law than to the usual $R^{1/4}$ law of spheroidal bulges (see Combes et al. 1990). In addition, because we know the orientation of the bars (approximately), we should be able to constrain their 3D light distribution. Thus, for the first time, we will be able to seriously test observationally 3D models of barred spiral galaxies. Furthermore, using our sample, we will be able to contrast the vertical light distribution of barred and unbarred systems. Finally, we will be able to study how the shape and scaleheight of bars vary with both radius and Hubble type (see, e.g., Burkert & Yoshii 1996). Although all the K-band imaging data have been acquired, none have been reduced or analysed, so we cannot report any results at this point.

6.2.4 Stellar Populations: Optical Imaging

The bar-buckling scenario for the formation of B/PS bulges invites a comparison of the stellar populations of the bar and disk once the bar has reached a steady state. In order to study this issue, we have obtained optical BVI broadband images for all our sample galaxies (see Just, Fuchs, & Wielen 1996), using the 1 m telescope at Siding Spring Observatory (direct imaging). Adding U-band data would be a significant enhancement, as it would help break the age-metallicity degeneracy. However, we recognise that the data for many objects will be seriously affected by dust, especially close to the plane. Again, none of these data have been analysed yet.

6.3 Future Work

The diagnostics developed in Chapters 3 and 4, and the results reported Chapters 2 and 5, encourage more work. Several aspects of our study of B/PS bulges should be deepened, while some interesting prospects are raised for the study of other types of galaxies. We discuss some potential projects in the next two sections.

6.3.1 Spiral Galaxies

In the spirit of Chapter 2, it would be extremely valuable to have more direct determinations of the pattern speed in barred spiral galaxies. The bar pattern speed is one of the most important parameters determining the structure and dynamics of barred spirals. Only with more direct measurements will we be able to test if our current models of barred disks are correct. Direct measurements of the bar pattern speed are required in both early-type and late-type spirals. However, because little secure knowledge on pattern speeds in late-type spirals has been gained from theory, the need is more urgent for these objects (see Elmegreen 1996). Now that we have demonstrated that H I observations can be used with the Tremaine-Weinberg (1984) method, at least for some objects, the situation for late-type spiral is more promising.

Some of the barred galaxies studied in Chapter 5 possess ionised gas PVDs with a great amount of structure (see, e.g., NGC 5746 in Fig. 5.1). Modelling these systems individually would be particularly rewarding. Not only would it enable us to constrain the mass distributions and bar pattern speeds very well (see Ch. 4), but we would also learn greatly about the effects of the bars on the interstellar medium, particularly in the central regions of the galaxies, near the ILRs. In the same spirit, it would be worthwhile to acquire 2D stellar kinematical data for a few objects (or, at least, obtain kinematical data away from the plane). These would allow a detailed comparison of the observed kinematics with that predicted from N-body simulations (see, e.g., Combes et al. 1990). In particular, it would allow a thorough investigation of cylindrical rotation in B/PS bulges, which has been predicted to stop outside of the brightest parts of the bar/bulge (see, again, Combes et al. 1990). With the advent of integral field spectrographs with relatively large fields (e.g. $30'' \times 30''$ for SAURON), such projects are becoming more realistic.

The idea of "bars within bars" has received a lot of attention in recent years. Many spiral galaxies with multiple triaxial structures have been observed (e.g. Wozniak et al. 1995) and it has been suggested that such structures could provide an efficient way to feed active galactic nuclei (see, e.g., Shlosman, Frank, & Begelman 1989). It would be worthwhile to develop multiple-bar diagnostics for edge-on spiral galaxies in a manner analogous to that of Chapters 3 and 4. The unique line-of-sight to edge-on spirals allows us to capture the kinematics of whole disks using simple long-slit spectroscopy, and would allow us to trace flows of material in the galaxies on various scales. N-body simulations (including gas) and periodic orbit studies of these object now exist (e.g. Friedli & Martinet 1993; Maciejewski & Sparke 1997), so the development of such diagnostics should be straightforward.

While we have shown in Chapter 5 that B/PS bulges in spiral galaxies are due to the presence of an edge-on bar, we could not determine how these bars formed. This is of course a crucial issue, as we cannot claim to understand bars fully if we can not explain how they formed. It is interesting to note that barred spirals are almost absent at the highest redshifts observable (see van den Bergh et al. 1996 for the Hubble Deep Field), while they are present in large numbers at intermediate redshifts (Couch, private communication), and dominate locally (e.g. Sellwood & Wilkinson 1993). It would be extremely interesting to determine when and in what environment bars can form. Both goals can be achieved by comparing the fraction of barred spirals in the field and in clusters as a function of redshift. With the advent of 8 m telescopes, such projects are now feasible, and they fit in very well with some of the major scientific objectives of this new generation of telescopes.

6.3.2 Dwarf and Elliptical Galaxies

The latest galaxies which are still clearly rotationally supported, the Magellanic irregulars, often have a bar which is offset from the center of the apparent disk (both photometrically and kinematically). Little is known about the dynamics of these systems, not even how the bar pattern revolves around the center of the disk (see, e.g., Colin & Athanassoula 1989; Odewahn 1994). Even less is known about their vertical structure. N-body simulations of rotationally supported disks, such as those of Combes et al. (1990), are representative mostly of early-type spirals. Similarly, our observations in Chapter 5 did not extend to spirals of type later than about Sc. It would thus be rewarding to search for bars in edge-on Magellanic irregulars. Any information gained this way would be an addition to our knowledge of these objects. As far as we know, no systematic study of their vertical structure has ever been attempted. However, it may be that the diagnostics developed in Chapter 3 and 4 are not appropriate for Magellanic irregulars, depending on the actual dynamics of the bars. In any case, a full study of the dynamics of these objects is warranted. Given the unusual location of the bar, such studies should prove very interesting and challenging.

The brightest elliptical galaxies are very likely to be triaxial systems (see, e.g., Binney 1980). Their figure is usually assumed to be non-rotating, but this may well be incorrect; there is little observational evidence to support this assumption. The results presented in Chapter 2 also suggest that the process of building up a dark halo may lead to a significant number of triaxial halos with a slow figure rotation. If this is true, then it seems likely that many elliptical galaxies would have a slowly rotating figure. It is possible that the bar diagnostics which we have developed for edge-on spirals could be applied to some ellipticals. Their figure rotation is likely to be slow, so the potentials should allow ILRs. As a small number of elliptical galaxies possess a significant gaseous disk, the effect of the resonances on the disks should be easily detectable, in a manner similar to the diagnostics presented in Chapters 3 and 4 (see also Bureau & Freeman 1997b). Another possible approach is provided by Tremaine & Weinberg's (1984) method. Although the method is designed to measure the pattern speed of 2D disks, none of the basic assumptions forbid an extension to 3D. It would thus be worthwhile to investigate if the method can be generalised to measure the pattern speed of triaxial ellipsoids. Elliptical galaxies with a minor axis dust lane may prove important for such studies, as in these objects the orientation of the line of nodes on the sky is known.

The simulation results presented in Chapter 2, which suggest that dark matter halos are not only triaxial but also have slowly rotating figures, were taken from a set of low resolution cosmological structure formation simulations constructed for a different purpose. We believe studies of figure rotation in halos should be extended to a larger range of simulations. In particular, it would be interesting to see if, in higher resolution simulations, halos with scales comparable to those of elliptical galaxies continue to display figure rotation.

References

Athanassoula, E. 1992, MNRAS, 259, 345

Athanassoula, E., Morin, S., Wozniak, H., Puy, D., Pierce, M. J., Lombard, J., & Bosma, A. 1990, MNRAS, 245, 130

Binney, J. J. 1980, Phil. Trans. R. Soc. London, 296, 329

Bureau, M., & Freeman, K. C. 1997a, PASA, 14, 146

———. 1997b, in The Nature of Elliptical Galaxies, ed. M. Arnaboldi, G. S. Da Costa, & P. Saha (San Francisco: ASP), 93

Burkert, A., & Yoshii, Y. 1996, MNRAS, 282, 1349

Byun, Y.-I. 1992, Ph. D. Thesis, The Australian National University

Colin, J., & Athanassoula, E. 1989, A&A, 214, 99

Combes, F., Debbasch, F., Friedli, D., & Pfenniger, D. 1990, A&A, 233, 82

Elmegreen, E. 1996, in Barred Galaxies, ed. R. Buta, D. A. Crocker, and B. G. Elmegreen (ASP: San Francisco), 505

Friedli, D., & Martinet, L. 1993, A&A, 277, 27

Just, A., Fuchs, B., & Wielen, R. 1996, A&A, 309, 715

Kuchinski, L. E., & Terndrup, D. M. 1996, AJ, 111, 1073

Kuijken, K., & Merrifield, M. R. 1995, ApJ, 443, L13

Maciejewski, W., & Sparke, L. S. 1997, ApJ, 484, L117

Meurer, G. R., Carignan, C., Beaulieu, S. F., & Freeman, K. C. 1996, AJ, 111, 1551

Meurer, G. R., Mackie, G., & Carignan, C. 1994, AJ, 107, 2021

Odewahn, S. C. 1994, AJ, 107, 1320

Olling, R. P. 1995, AJ, 110, 591

———. 1996, AJ, 112, 481

Sellwood, J. A., & Wilkinson, A. 1993, Rep. Prog. Phys., 56, 173

Shaw, M. A. 1987, MNRAS, 229, 691

Shlosman, I., Frank, J., & Begelman, M. C. 1989, Nature, 338, 45

Tremaine, S., & Weinberg, M. D. 1984, ApJ, 282, L5

van den Bergh, S., Abraham, R. G., Ellis, R. S., Tanvir, N. R., Santiago, B. X., & Glazebrook, K. G. 1996, AJ, 112, 359

Wozniak, H., Friedli, D., Martinet, L., Martin, P., & Bratschi, P. 1995, A&AS, 111, 115